Hochschule für Angewandte Wissenschaften Hamburg
*Hamburg University of Applied Sciences*

# Master Thesis

Horst Knoop

# Numerical Simulation of failure of adhesively bonded composite parts using the cohesive zone method

*Fakultät Technik und Informatik*
*Department Fahrzeugtechnik und Flugzeugbau*

*Faculty of Engineering and Computer Science*
*Department of Automotive and Aeronautical Engineering*

**Horst Knoop**

# Numerical Simulation of failure of adhesively bonded composite parts using the cohesive zone method

Master thesis submitted in line with the master examination

in the program of aeronautical engineering studies/design and light construction
at the department automotive and aeronautical engineering
of the faculty technic and computer sciences
of the Hochschule für Angewandte Wissenschaften Hamburg

in cooperation with:
Airbus Defence and Space
Department TAECA24 structural optimization / simulation
Rechliner Str.
85077 Manching

First examiner: Prof. Dr.-Ing. Wilfried Dehmel
Second examiner: Prof. Dr.-Ing. Jens Baaran

Corporate supervisor: Dipl.-Ing. Tim Pühlhofer

Closing date: 22.02.2016

# Zusammenfassung

**Horst Knoop**

**Thema der Masterthesis**

Numerische Simulation des Versagens geklebter Faserverbundbauteile unter Benutzung der Cohesive Zone Methode

**Stichworte**

Faserverbundtechnologie, Klebefügung, Cohesive Zone Methode

**Kurzzusammenfassung**

Das Ziel der vorliegenden Arbeit ist es, das Versagen einer geklebten Verbindung aus Faserverbundbauteilen zu simulieren. Die Simulationen sind diesbezüglich unter Anwendung der Cohesive Zone Methode mit dem FEM-solver Nastran (SOL400) am Standort von Airbus Defence & Space in Manching durchgeführt worden. Im Rahmen einer Validierungspyramide werden unterschiedlich komplexe Strukturen nichtlinear analysiert und mit dem Verhalten getesteter Prüfkörper verglichen. Dabei wird die ingeneursmäßige Tauglichkeit der Methode unter anderem im Hinblick auf die benötigten Rechenzeiten und der Analysequalität untersucht.

# Abstract

**Horst Knoop**

**Title of the paper**

Numerical Simulation of failure of adhesively bonded composite parts using the cohesive zone method

**Keywords**

Fibre-reinforced composites, adhesive bonding, cohesive zone method

**Abstract**

The present work aims in the proper simulation of failure of adhesive composite joints. In this regard, the simulations are executed using the cohesive zone method implemented in the FEM-solver Nastran at the site of Airbus Defence & Space in Manching. In the context of a validation pyramid, structures of different complexity are nonlinearly analyzed and afterwards compared with the behavior of tested specimen. In the process, the suitability of the method for the engineering sector is studied by evaluating amongst others the required computing costs and the quality of analysis.

AIRBUS DEFENCE & SPACE

Hochschule für Angewandte Wissenschaften Hamburg
*Hamburg University of Applied Sciences*

# Task for the master thesis of Horst Knoop

Title

## Numerical Simulation of failure of adhesively bonded composite parts using the cohesive zone method

Task:

- Literature research to the calculation of adhesively bonding failure by cohesive zone elements (CZE)
- Investigation on the Influences of material parameters: Which material parameters are necessary for cohesive zone elements? How are these parameters employed in the FE-model? Which tests can be performed to determine and adapt the material parameters?
- Nonlinear FE-Analysis of coupons, substructures and component parts (EF-airbrake) by cohesive zone elements
- Description and evaluation of the FE-models (types of elements, meshing, model parameter) and of the nonlinear calculation processes
- Visualisation and discussion of the simulation results
- Comparison of the simulation results with the results of testing
- Basic statements of failure behaviour of adhesively bonded composite parts
- Supplementary notes to additional influences as temperature and fatigue loading

The work of Mr. Knoop shall make a contribution to develop a reliable method of calculation and stress analysis of large adhesively bonded composite parts.

# Acknowledgement

In this way I want to thank all the people who supported and motivated me during the production of this thesis.

First my particular thanks goes to Tim Pühlhofer who supervised my master thesis at the location in Manching at Airbus Defence & Space. I want to express my special gratitude for the helpful suggestions and the constructive criticism along the creation of this work.

Furthermore my sincere thanks goes to the teammates, Urs Bob, Mircea Calomfirescu, Jürgen Grygier and Guido Hammes who contributed to the guidance of this thesis by holding numerous interesting debates with me.

Special thanks go to Axel Lins who technically supported the executed computer based work at the site of Airbus Defence & Space in Manching. I appreciate his prompt and target-oriented way to help out when any software specific problems did arise. Additionally i want to express my gratitude to C. Gelten from the MSC software support in this way who took care for my Nastran specific questions.

I want to thank my supervising professor at the HAW Hamburg, prof. W. Dehmel, for his advice and the evaluation of this work. Our meetings and his decent answers did support myself in the organization, the planning and the execution of this thesis. Furthermore my thanks go also to prof. J. Baaran for evaluating and examining this work.

Finally I thank my siblings, Bettina and Michael Knoop for their helpful advices on formal and linguistic level.

# Contents

# List of Figures

# List of Tables

# Nomenclature

## List of Abbreviations

| | |
|---|---|
| CFC | Carbon fiber composite |
| CFRP | Carbon fiber reinforced plastics |
| CLS | Cracked Lap Shear |
| CLT | Classical Laminate Theory |
| CS | Certification Specification |
| CZ | Cohesive Zone |
| CZE | Cohesive Zone Elements |
| CZM | Cohesive Zone Method |
| DLJ | Double-Lap Joint |
| DLR | Deutsche Zentrum für Luft- und Raumfahrt |
| EASA | European Aviation Savety Agency |
| ESA | European Space Agency |
| FEA | Finite Element Analysis |
| FEM | Finite Element Method |
| FFS | Fortschrittliche Flugzeugstrukturen |
| GSF | Graphical Scale Factor |
| LFM | Linear Fracture Mechanics |
| MPC | Multi point constraint |
| OEM | Original Equipment Manufacturer |
| SLJ | Single-Lap Joint |
| SLS | Single Lap Shear |

UD ..... Unidirectional

VCCT ..... Virtual Crack Closure Technique

WIWeB ..... Wehrwissenschaftliche Institut für Werk- und Beriebsstoffe

LTSM ..... Laboratory of Technology and Strength of materials

SBT ..... Simple beam theory

UPV ..... Load-displacement convergence criterion

## List of Symbols

$\alpha$ ..... Stiffness factor to model the behavior of a CZE

$\beta_1$ ..... Modal stress ratio

$\beta_2$ ..... Modal ratio of fracture toughness

$\beta_{MixedMode}$ ..... Mixed-mode ratio of a CZE

$\gamma_{shear}$ ..... Shear strain

$\kappa$ ..... Curvature of the bending line

$\mu$ ..... Friction coefficient

$\nu$ ..... Opening displacement of a CZE

$\nu_n$ ..... Opening displacement of a CZE in elemental normal direction

$\nu_s$ ..... Opening displacement of a CZE in elemental s-shear direction

$\nu_t$ ..... Opening displacement of a CZE in elemental t-shear direction

$\nu_{12}$ ..... Poisson's ratio for an UD-layer in 12-direction

$\nu_{13}$ ..... Poisson's ratio for an UD-layer in 13-direction

$\nu_{23}$ ..... Poisson's ratio for an UD-layer in 23-direction

$\nu_{c,n}$ ..... Critical opening displacement of a CZE in normal direction

$\nu_{c,shear}$ ..... Critical opening displacement of a CZE in both shear directions

$\nu_c$ ..... Critical opening displacement of a CZE

$\nu_{max,n}$ ..... Maximum opening displacement of a CZE in normal direction

$\nu_{max,shear}$ ..... Maximum opening displacement of a CZE in both shear directions

$\nu_{max}$ ..... Maximum opening displacement of a CZE

$\nu_{res}$ ..... Resultant opening displacement of a CZE

$\psi$ ..... Stiffness relation between adherends

$\rho$ ..... Characteristic adhesive factor

$\sigma_{max}$ ..... Critical traction of a CZE in normal direction

$\tau$ ..... Interface stress of a CZE

$\tau_{i,max}$ ..... Stress peak in adhesive layer

$\tau_{limit}$ ..... Stress representing limit load

$\tau_{max,n}$ ..... Critical traction of a CZE in normal direction

$\tau_{max,shear}$ ..... Critical traction of a CZE in both shear direction

$\tau_{max,s}$ ..... Critical traction of a CZE in s-shear direction

$\tau_{max,t}$ ..... Critical traction of a CZE in t-shear direction

$\tau_{max}$ ..... Critical traction of a CZE

$\tau_n$ ..... Traction of a CZE in normal direction; normal stress

$\tau_{res,shear}$ ..... Resultant traction of a CZE in shear direction

$\tau_{rigidadherend}$ .... Averaged shear stresses assuming rigid adherends

$\tau_{shear}$ ..... Traction of a CZE in shear direction; shear stresses

$\tau_s$ ..... Traction of a CZE in s-shear direction

$\tau_t$ ..... Traction of a CZE in t-shear direction

$\tau_{ultimate}$ ..... Stress representing ultimate load

$\tau_{Volkersen,max}$ ... Maximum shear stress along Volkersen's analysis

$\tau_{yield}$ ..... Yield strength

$\varepsilon_x$ ..... Strain in x-direction

$\varepsilon_{FEM}$ ..... Strains in the FEM-model

$\varepsilon_{straingauge}$ ..... Strains at the position of a strain gauge

$b$ ..... Width of the adhesive joint

$d$ ..... Damage value of a CZE

$d_{straingauge}$ ..... Undeformed length of a strain gauge

$E$ ..... Modulus of elasticity

$E^t$ ..... Present modulus of elasticity

$E_{11}$ ..... Modulus of elasticity for an UD-layer in the direction of the fiber

$E_{22}$ ..... Modulus of elasticity for an UD-layer perpendicular to the fiber direction

$E_{33}$ ..... Modulus of elasticity for an UD-layer perpendicular to the fiber direction

$ERR_{conv,explicit}$ . Error of convergence using the explicit solution algorithm

$ERR_{conv,implicit}$ . Error of convergence using the implicit solution algorithm

$ERR_{conv,UPV}$ ... Allowed error of convergence using the UPV-criterion

$F_{cl}$ ..... Clamping force

$F_{crit}$ ..... Critical force of a specimen

$F_{sim,crit}$ ..... Critical force of a specimen in the simulation

$F_{test,crit}$ ..... Critical force of a sample at the testing

$G$ ..... Shear modulus

$G_C$ ..... Critical energy release rate

$G_{12}$ ..... Shear modulus for an UD-layer in 12-direction

$G_{13}$ ..... Shear modulus for an UD-layer in 13-direction

$G_{23}$ ..... Shear modulus for an UD-layer in 23-direction

$G_{IC}$ ..... Critical energy release rate in normal direction

$G_{IIC}$ ..... Critical energy release rate in shear direction

$I_y$ ..... Geometrical moment of inertia in y-direction

$K$ ..... Stiffness

$K_{el,n}$ ..... Elastic stiffness of a CZE in normal directions

$K_{el,shear}$ ..... Elastic stiffness of a CZE in both shear directions

$K_{el}$ ..... Initial stiffness of undamaged CZE

$K_{pl}^{t}$ ..... Present stiffness of CZE respecting elemental softening

$l_E$ ..... Edge length of an element

$l_{CZE,Model,min}$ ... Minimal required edge length of a CZE for exclusive tensile-loading

$l_{CZE,ModelI,min}$ .. Minimal required edge length of a CZE for exclusive shear-loading

$l_{CZE}$ ..... Length of a Cohesive Zone Element

$l_{CZ}$ ..... Length of the Cohesive Zone

$l_{E,Composite}$ ..... Edge length of a composite element

$l_{joint,crit}$ ..... Critical overlap length of the adhesive joint

$l_{joint}$ ..... Overlap length of the adhesive joint

$M$ ..... Factor according to the approach of the determination of the mesh size

$M_y$ ..... Bending moment in y-direction

$n_{incr}$ ..... Amount of increments

$n_{iterations/incr}$ ... Number of iterations per increment

$P$ ..... Loading force

$QIC$ ..... Quadratic Interaction Criterion

$t$ ..... incremental time of nonlinear analysis

$t_{T-Pull}$ ..... Wall time of the T-Pull simulation

$t_{T-Shear}$ ..... Wall time of the T-Shear simulation

$t_{T-Tension}$ ..... Wall time of the T-Tension simulation

$th_{adhesive}$ ..... Thickness of adhesive layer

$th_{CZE}$ ..... Initial thickness of a CZE

$u$ ..... Applied displacement

$u_{bottom}$ ..... Averaged displacements for the adhesive bottom surface

$u_{straingauge}$ ..... Displacements at the position of a strain gauge

$u_{top}$ ..... Averaged displacement for the adhesive top surface

$w$ ..... Displacement in z direction

# 1. Introduction

This work deals with the numerical simulation of adhesively bonded composites using the Cohesive Zone Method (CZM).
For that purpose the work delivers at first an introductory overview of the current situation before the contents and the objective of the work are presented.

## 1.1. Current Situation

Traditionally aircraft have been mainly manufactured out of metallic materials. Aluminum and its various alloys have been a proper material to design aeronautical structures as a good possibility of lightweight construction for decades.
On account of the rising requirements to the economic viability of aircraft, engineers are willing to reduce the basic weight further. In respect thereof suitable materials for aeronautical engineering have to combine a low density with good mechanical properties.

Carbon fiber composite (CFC) satisfies these two characteristics outstandingly. Chiefly it has excellent strength properties and possesses in the same time a lower density than aluminum alloys. Further benefits of CFC are the resistance to corrosion and the positive fatigue performance during continuous loading.
Considering CFC as an orthotropic material, structural parts can be modeled the way that the mechanical preference direction of the material points along the same direction as the main loading path. This possibility leads at a proper dimensioning to a maximum utilization of the installed materials.

Nowadays the named advantages of CFC result in an increasing use in the aeronautical field. Nevertheless, the use of composites generates some new and almost unexplored problems. Using carbon fiber reinforced plastics (CFRP) in aircraft structures, promises of weight reduction of 20% to 30%, which have been given from the very first, are not kept according to [7]. The reasons for that are various.
The inexperience in the optimal use of composites forces to thicken critical parts of the aircraft structure to guarantee the necessary safety factors.
Apart of it, the anisotropy of composites requires generally high engineering and constructional efforts and thus it leads to high expenses for the original equipment manufacturer (OEM).

In the evaluation of the composite utilization the joining of parts gets a particular significance. In general composite parts are manufactured most often using an integral construction method, like for example the Co-curing method, where several adherends are adhesively joined and cured together in an autoclave [32].
Anyhow there are plenty ambitions to apply the differential construction technique, because of the following reasons.
First the use of the differential construction method improves the efficiency of maintenance, because smaller parts can be exchanged. Secondly the manufacturing process can be regulated more variable with the refined segmenting and can be outsourced more easily. These two major reasons provide an important need of developing good joint concepts for several interfaces.
The conventional method of joining in the aeronautical field is riveting. While metallic materials, like aluminum cope quiet well with a perforated design of the joints, due to their plasticity properties, composite materials like CFC are not appropriate for the riveting method. The holes which would be needed for a riveted or a bolted joint, destroy the high loaded fibers of the composite material. To obtain the necessary stability and strength nonetheless, the composite parts at riveted or bolted interfaces have to be designed much thicker than the rest of the composite structure, which would controvert the aspired lightweight dimensioned joint.
Adhesive bonding represents a suitable alternative of joining composites in a lightweight construction method [13]. That is the reason why its popularity rises enormously in recent days. For example, in the A380, adhesive bonding methods are applied already in nearly every part of the aircraft.

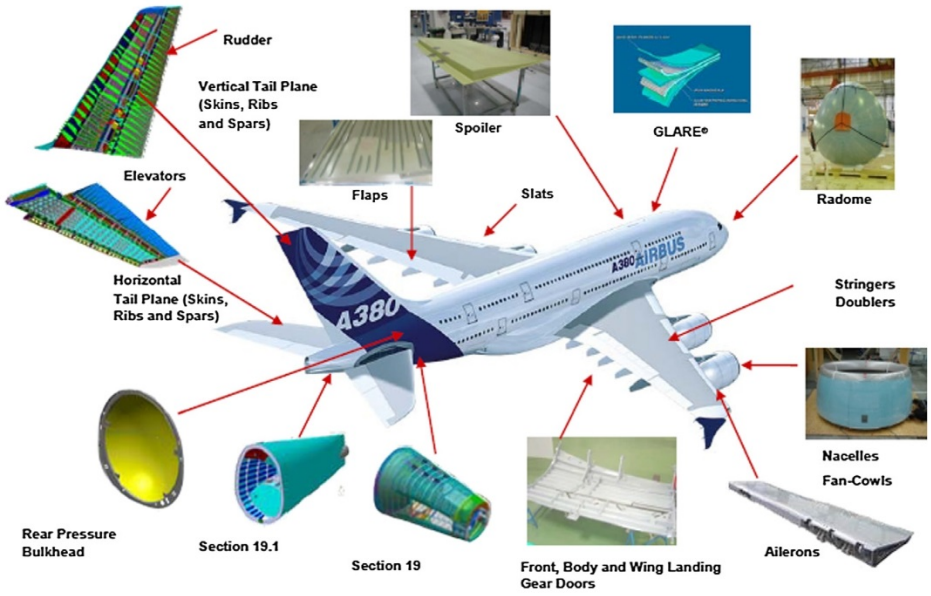


Figure 1.1: Application of adhesive bonding technologies at the Airbus A380 (s. [6])

In contrast to the previously stated joint methods, adhesive bonding provides an approximately continual load transmission. Thus, in present days there is high investigation in searching suitable adhesive material and adhesive methods for the engineering sector. At the same time, the knowledge about adhesives is assembled, so that studies are conducted to predict adhesive behavior more accurately. This is also the aim of this thesis.

## 1.2. Contents and Objective of this thesis

This thesis engages in the modeling and the simulation of adhesively bonded composite parts, to contribute to the extensive present investigation on adhesive bonding.

The main task of the present work focuses on the verification, if diverse adhesively bonded composite parts can be accurately modeled on different levels of complexity. At the same time, the work shall provide information about the required computing costs in order to determine the signification and the reasonability of simulating large components using the cohesive zone method.
In the process, the components to be studied are parts of a validation pyramid shown in figure 1.2. It uses an iterative validation process to finally validate a large complex adhesively bonded structural component at the example of an airbrake.

The pyramid has been established within the project „HAP1000: Structural Adhesive Bonding Technologies and Demonstrator“ in the superordinated project „Advanced Aeronautic Structures“ at Airbus Defence & Space in Manching. The greater project includes studies in modern and promising structural technologies of the aeronautical field for upcoming design requirements.

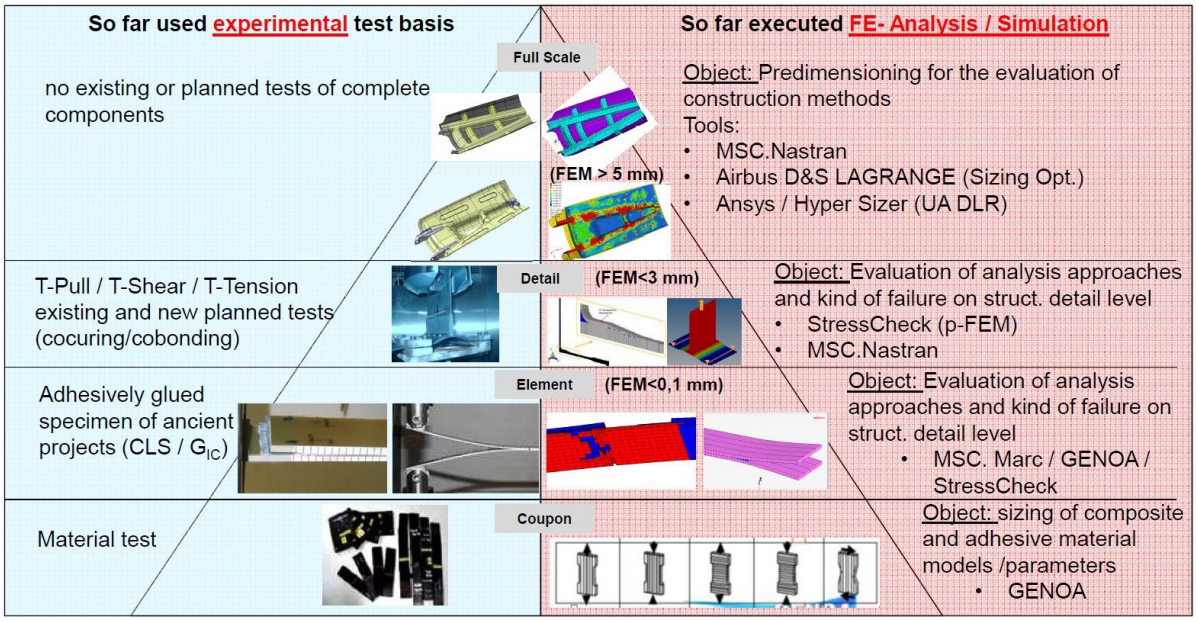


Figure 1.2: Method of validating complex adhesively bonded CFC-structures

The main vertical division of the pyramid represents the difference of a basis of real experimental tests on the blue left hand side and a basis of analysis, delivering the virtual reproduction via a model using the finite element method (FEM) on the red right hand side.

This comparison of virtual simulation and the real component behavior during testing is absolutely necessary for the certification of structural parts. In the CS-25.307 the EASA specifies for large airplanes that „structural analysis may be used only if the structure conforms to that for which experience has shown this method to be reliable“ according to [29]. Furthermore it indicates that „in other cases substantiating tests must be made to load levels that are sufficient to verify structural behavior up to loads specified in CS 25.305“.
Corresponding to this statement, tests for validating components are unavoidable to obtain the necessary experience of their structural behavior. But on the other side it is reasonable to develop a reliable validated structural model, so that later on experimental testing expenses can be reduced by having a structural model, which is able to accurately simulate also the behavior of slightly modificated components[28].

This work promises correspondingly to verify the created virtual analyzed models by checking their results as often as possible against results of experimentally tested equivalent specimens.

From the bottom to the top of the imaged validation pyramid, the complexity of the structural parts rises level wise simultaneously for both sides. It is up to the employed executing team to determine which and how many necessary sub-steps and sub-levels to complete to sufficiently validate the final component at the top of the validation pyramid. In this process the pyramid arranges four different levels from coupon level to full scale level. Once a level is completed, the following higher level can be studied.

The coupon level at the basis of the validation pyramid deals with pure material awareness. This means that all necessary material data needed for the final component is gathered independently of any structural geometry. On the one hand side, this stage includes material tests which give characteristic information about a material, on the other hand these characteristic material information must further on be prepared for the

application in the computer based models.
Once all necessary material information are available, the element level of the pyramid can be focused. In this level geometrically small and simple models are created on which the gained material information are implemented. Basic model parameters are set and defined for the following steps of the pyramid, while all relevant model parameter are evaluated critically. If the parallel executed experimental tests verify these models, the detail level can be focused.
In this higher level of the pyramid more complex structures are analyzed and this level thus forms an intermediate step to the full scale level at the tip of the pyramid. Fundamental for this step is, among other things, the evaluation of the analysis size, because in the related proportion first estimations of the size of the final model can be done.
At the tip of the pyramid an entire complex structural component is validated by the presented method. In the studies of adhesive joint analysis within the project HAP1000 an adhesively secondary bonded airbrake represents the final structural component.

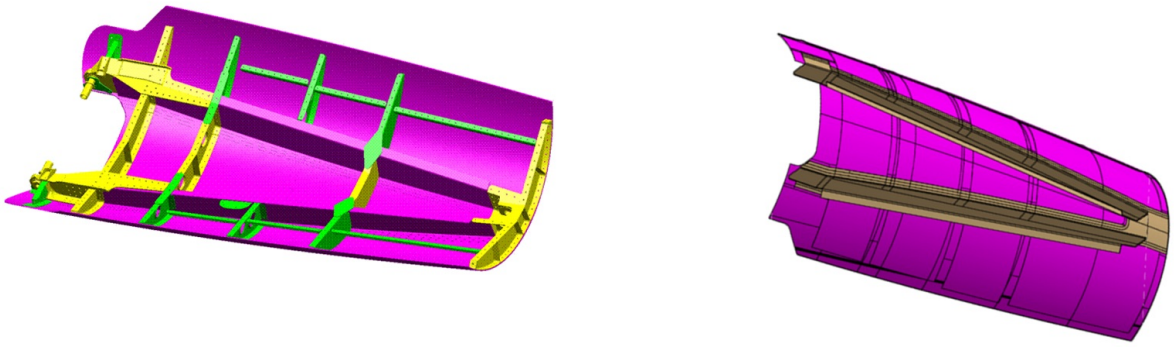

Figure 1.3: Present differential riveted hybrid airbrake model (CFC & metal) (s. [32]) (left) / Proposal of a fully adhesively bonded CFC-airbrake-model in differential construction method (s. [32]) (right)

Figure 1.3 maps the graphical model of the existing and integrated airbrake on the left hand side while on the right hand side a simple proposal for a fully adhesively bonded CFC-airbrake-model using the differential construction method is presented.

The proposal of the fully adhesively bonded CFC-airbrake-model is also named the „a-model“ where the structural concept of the serial produced airbrake remains unchanged and where only materials already certified for the aircraft industry are used [32].

The material information are given via several tests of specified cooperating partners and previous investigations on the adhesive joint project, within this thesis. Thus, after a theoretical introduction in the subject is given, this work starts with the implementation of the material data into numerical FEM-models. Subsequently the primary focus of this work stays on the simulation of models on the element and the detail level of the validation pyramid.
In the end of the thesis the results shall be summarized and critically discussed.

In this work only the solver MSC Nastran V2014 R1 is used. This version of MSC Nastran offers the possibility of cohesive zone modeling (CZM) as well as advanced contact modeling methods, which both form essential conditions for the creation of the adhesively bonded component-models in this work.
Additionally MSC Nastran is presently according to their own statement [3] the worldwide most used FE-solver for structure analysis in the areas statics, dynamics and acoustic.
The pre- and post-processing of the virtual models is performed with Hyperworks 13.0 and to some extend with Patran 2014.

# 2. Theoretical background information

First of all, the related theory to the subject is explained. All theory and literature review of this thesis which is necessary to understand the adhesive behavior and its modeling is fitted in this section.

As this work is exclusively about the mechanical loading of adhesively bonded joints, the first subchapter 2.1 describes these. Especially simplified analytical approaches of adhesive dimensioning is stated in the subsection 2.1.3.
The analytical equations of theory have due to their stress stress nonlinearity and for a suitable use in complex structures to be transformed into a numerical model. The numerical model is established and analyzed by the method of finite elements and thus the following subchapter 2.2 presents the Finite Element Analysis (FEA). The FEA is the most frequently used engineering tool to analyze complex solid structure components. Since the FEA is realized by the solver MSC Nastran V2014 R1, this subchapter exclusively shows the herein available methods of adhesive modeling.

Additionally to the local discretization implemented by the FEA, a temporal discretization in a structure simulation is necessary, if it comes to nonlinear structural effects, as they appear in failing adhesively bonded components. For this purpose an overview about linear and nonlinear mechanical structure analysis is attached to this thesis in the appendix A.2.

## 2.1. Adhesive joints

Adhesive joints are playing an evermore important role in the field of lightweight construction. Most of all, the use of composites benefits the structural adhesive bonding technology bringing up an increasing investigation in adhesive joining in present days. While on the one hand, the weight of mechanic fastener and additional necessary material doubler at a joint position can be saved, on the other hand few potential spots for damage initiation exist using an adhesively bonded joint. The breadth-wise homogeneous load transfer is the reason for this.
As a permanent bonding method, we differentiate adhesive joints according to their geometrical appearance.

### 2.1.1. Design of adhesive joints

Since a light weight design benefits generally the use of thin planar sheets, the most common geometrical configurations of adhesively joining thin sheets are imaged in figure 2.1.

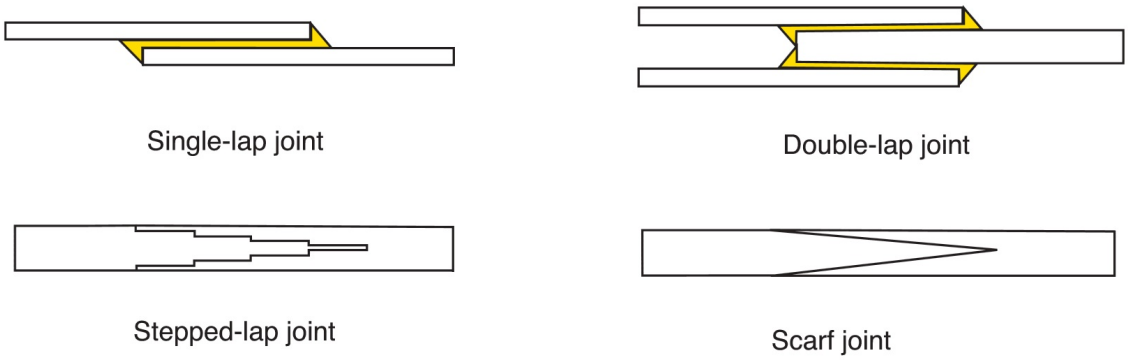


Figure 2.1: Configurations of adhesive joints (s. [11])

The presented basic configurations of adhesive joints do all have an important position in the adhesive joining technology, because each configuration shows up its own particular qualities.
While the single- and the double-lap joint comparably show a low effort in fitting and pre-treatment, the scarf and the stepped-lap joint persuade with much better strength properties, as the Hart-Smith-diagram (s. [8]) demonstrates in the appendix A.2.
In the diagram the adhesive joint strength is plotted over the adherends thickness. Furthermore, the diagram gives an idea of which part of adhesive and adherend is the critical part of the joint.
The failure types of adhesive joints are hence discussed in the following section.

### 2.1.2. Failure types of adhesive joints

The typical kind of failure for each joint configuration is named in the Hart-Smith-diagram. Proper dimensioned scarf joints tend to bring up such a high strength that the failure occurs mostly in the adherends next to the joint area. According to [43] this is explained by the stress distribution in the adhesive. At a large scarf angle the normal adhesive stresses $\tau_n$ are transferred into shear stresses $\tau_{shear}$ proposing the ideal loading condition of an adhesive joint. In general the peeling caused by normal stresses, counts

namely as the critical loading of an adhesive joint according to [40] and [43].
Thus, adhesive joints should be preferably designed for shear loading and design solutions should be respected to avoid any peeling behavior.

The possible failure modes of an adhesive joint at the example of a single-lap joint are simplified depicted in figure 2.2.

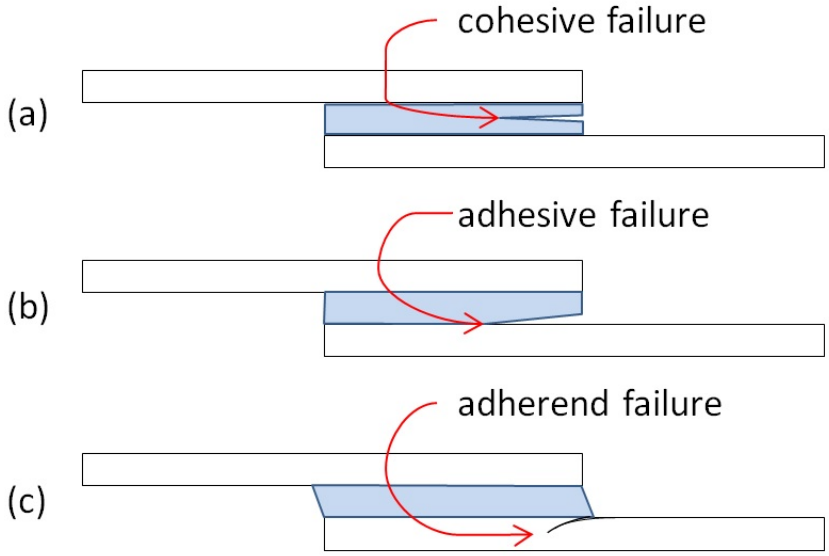


Figure 2.2: Differentiation of failure modes of an adhesive joint

A possible way for adherend failure, as it is usual for scarf joints, is illustrated at position (c).
If the joint itself is the critical part, the failure may basically occur in form of cohesive (a) or adhesive (b) failure. Cohesion describes the chemical bonding forces of atoms within one material. It is significant for a cohesive failure that the crack propagates through the adhesive layer. Thus, the material parameter of the adhesive forms the problem.
Adhesion in contrast defines the contact forces between molecules of two different surfaces. The adherend separates directly at the interface to the adhesive layer when an adhesive failure occurs. By the use of proper surface pre-treatment of the adherends the adhesion properties of the joint can be improved.

### 2.1.3. Analytical approach of cohesive stress determination in lap joints

The analytical approach of describing an adhesive joint is presented herein to show that its precise determination can raise already at very basic geometrical structures to a vast challenge. In this way, this chapter promotes already the nowadays suitable use of the numerical approach via Finite Element Method (FEM) even for the analysis of a geometrical simple adhesive joint.

There are various analytical approaches to analyze the stress and strain distribution in an adhesive layer. The most basic approaches are mentioned in the following subsections 2.1.3.1 to 2.1.3.3. The type of the adhesive joint geometries, the multiple possible loading conditions and the variety of different materials for adhesive and adherends influence the adhesive behavior crucially.
The majority of analytical adhesive models in the literature are two dimensional [17]. The appendix A.1 lists a variety of analysis approaches for adhesive models of two-dimensional single- and double-lap joints. Corresponding to [17] the challenge of some listed models increase so far that no analytical closed-form solution exists yet, though all models are two-dimensional simplifications. In those cases, a numerical solution has to be pursued.

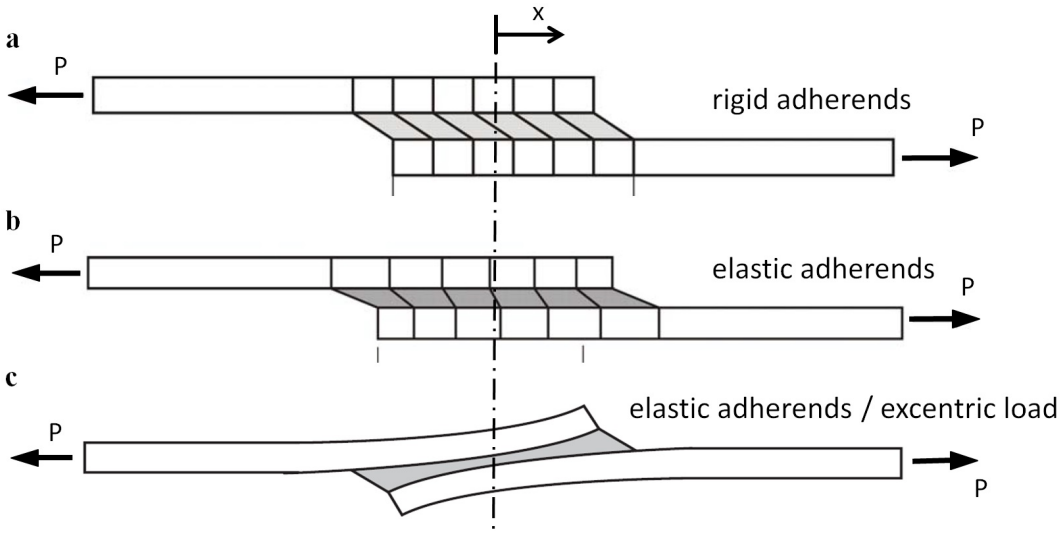


Figure 2.3: Simplified deformation models of a single-lap joint: rigid adherends (a) according to [17], elastic adherends (b) according to [17] and model respecting the eccentric load, with elastic adherends (c) according to [11]

#### 2.1.3.1. Rigid adherend stress analysis

If a lap joint is loaded on tensile forces $P$ only, as it is shown in figure 2.3, the simplest linear elastic approach of two-dimensional stress analysis models according to [17] is to pretend that both adherends are rigid and that the adhesive deforms only in shear (model a).

This would result in a constant averaged shear stress $\tau_{rigidadherend}$ along the overlap length $l_{joint}$ and the width $b$ of the adhesive layer along the equation (1).

$$\tau_{rigidadherend} = \frac{P}{b \cdot l_{joint}} \tag{1}$$

Indeed, this analysis is a simplification, which is just appropriate, if the adherends can be considered as rigid.

In other cases a different analytical approach should be chosen to determine the stress distribution in the adhesive layer. Though, the equation (1) can still be used in all cases to determine the mean shear stress in an adhesive layer.

#### 2.1.3.2. Volkersen's analysis

A further analytical approach of adhesive dimensioning under the same loading conditions shall be presented next. The approach is an elasto-static analysis of an adhesive lap joint along Volkersen according to [13]. In contrast to the just stated approach, Volkersen respects the elasticity of the adherends in length direction ($x$-direction) in his analysis (figure 2.3 b).

In order to develop the shear stress distribution the equations of the balance of forces, the kinematic relations and the law of elasticity form together a homogeneous differential equation of second order, which has the following solution:

$$\frac{\tau_{Volkersen}(x)}{\tau_{rigidadherend}} = \frac{\rho}{2} \cdot \left[ \frac{cosh(\frac{\rho \cdot x}{l_{joint}})}{sinh(\frac{\rho}{2})} - \frac{(1-\psi) \cdot sinh(\frac{\rho \cdot x}{l_{joint}})}{(1+\psi) \cdot cosh(\frac{\rho}{2})} \right] \tag{2}$$

$\rho$ defines a characteristic adhesive factor and $\psi$ defines the stiffness relation of both adherends. The effect of Volkersen's analysis is, that the shear stresses in the adhesive are dependent on the length variable $x$ of the adhesive layer and they increase strongly towards the adhesive edges. These stress peaks at the edges $x = l_{joint}/2$ shall be named $\tau_{i,max}$.

A corresponding shear distribution over the adhesive overlap length is mapped in figure

2.4.

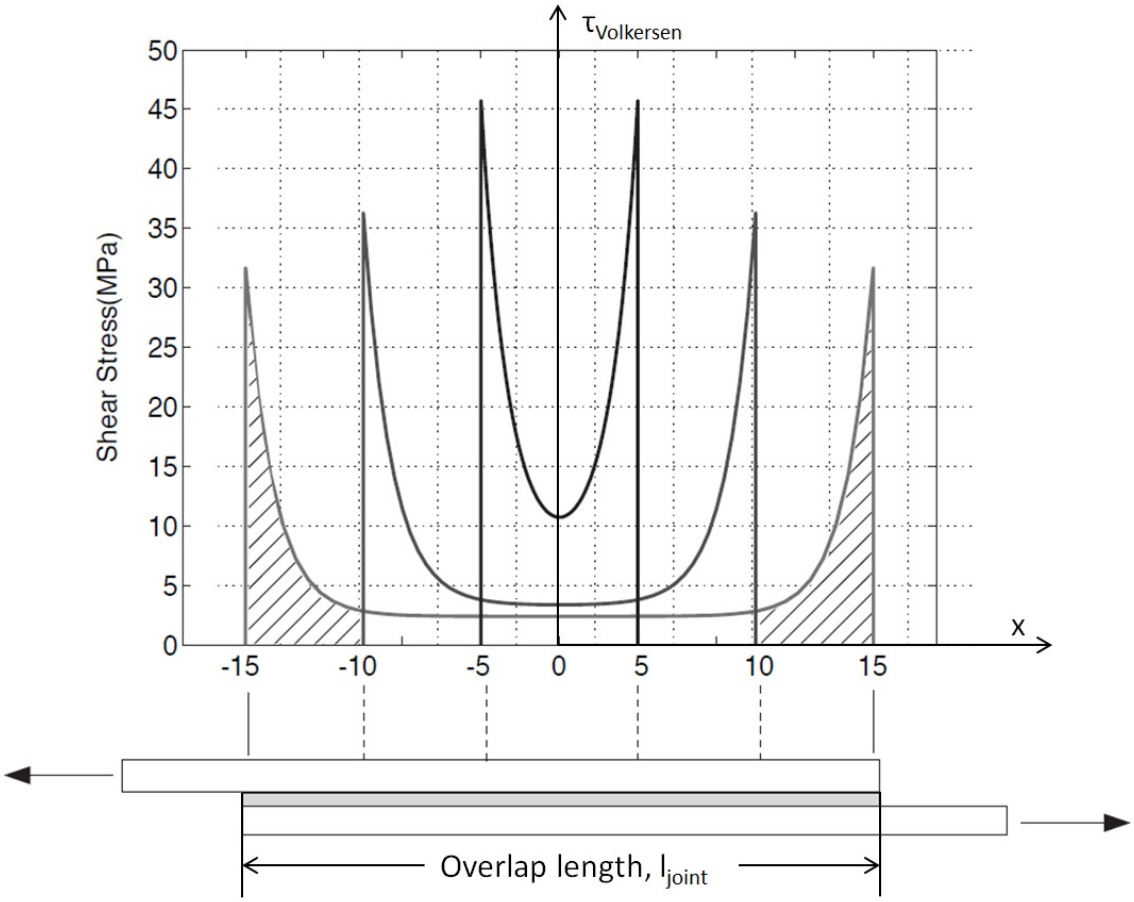


Figure 2.4: Shear stress distribution in a bonded single-lap joint resulting out of Volkersens analytical approach pursuant to [11]

With the two simplifications that both adherends have the same material and geometric properties and that the joint length exceeds a critical value $l_{joint,crit}$, the following equation offers to calculate the maximum shear stresses $\tau_{Volkersen,max}$ at the adhesive edges:

$$\tau_{Volkersen,max} = \frac{P}{b} \cdot \sqrt{\frac{G_{adhesive}}{2 \cdot E_{adherend} \cdot t_{adherend} \cdot t_{adhesive}}} \tag{3}$$

This is possible because if a certain overlap length is exceeded, the stress maxima at the adhesive edges don't decrease anymore and stay at a constant level with a further increasing overlap length. Thus equation (3) becomes independent of the overlap length

$l_{joint}$ and is valid if $l_{joint} > l_{joint,crit}$, with:

$$l_{joint,crit} = \frac{5}{\sqrt{\frac{G_{adhesive} \cdot 2}{E_{adherend} \cdot t_{adherend} \cdot t_{adhesive}}}} \tag{4}$$

The main restriction for Volkersen's analysis model is that the eccentric load path of a SLJ (image c in figure 2.3) is not considered, meaning a disregard of the occurring peel-stresses in the adhesive layer. Thus, Volkersen's theory is mainly appropriate for DLJ models according to [13].
An eccentricity of the load path leads at the example of the SLJ to a deflections of the adherends. In the wake of this bending effect at the adhesive joint, peel stresses are caused corresponding to [43].
According to [9] and as the Hart-Smith-diagram demonstrates, the peel stresses form a main problem in SLJ failures and should thus be considered, by choosing a different analytical approach for the proper description of SLJs.

#### 2.1.3.3. Further two-dimensional analysis

J.W. van Ingen and A. Vlot wrote a report about further two-dimensional stress analysis theories of adhesively bonded single-lap joints (s. [12]) in which the eccentricity of the load path is respected (figure 2.3 c). Theories thereby considering the peel stress distributions in the adhesive layer are for instance the Goland/Reissner approach and the Hart-Smith approach. The differential equation for shear and peel stress of these theories are solved in [12] and shall just be referred to in this way.

Finally, the peel stress distribution in an adhesive lap joint possesses stress maxima at the adhesive edges due to the elasticity and the eccentricity of the adherends according to [13].
In contrast, advanced theories of adhesive stress determination on lap joints determine that the shear stresses at the adhesive edges are equal to zero pursuant to figure A.3 in the appendix. Anyway, also the advanced consideration of the shear stress distribution depicts the shear stress maxima of the adhesive layer close to the adhesive edge. Thus it reveals that the shear stress distribution has high stress gradients close to the adhesive edge, analog to the peel stress distribution.

In the end it has to be summarized that there has not been found an ultimate approach

yet to completely determine the adhesive stress consideration for any adhesive lap joint. Thus, the basic analytical approaches presented (mean stress determination (equation (1)), Volkersen analysis) are often employed in practice.

A possible analysis of scarf and stepped-lap joints is proposed by the ESA in [9].

## 2.2. Finite Element Analysis (FEA)

In cases where the analytical approaches of structure analysis are not existent or sufficient anymore, the Finite Element Analysis (FEA) is often suitable. Advantages of the FEA are its universal utilisability on diverse complex structures and its ability to show graphically excellent results and to help the user to understand complex problems.

### 2.2.1. Background of the FEA

In practice we try to reproduce reality as accurate as possible. Virtual models often help in this regard using modern computing power to approximately reproduce real situations. In favor several steps of model creation have to be completed one after another (s. [18]). In all the mentioned steps of model creation in image 2.5 the model becomes more inexact by accepting inevitable model faults. These faults should be kept as small as possible and have to be taken into account by judging final results of modeling.

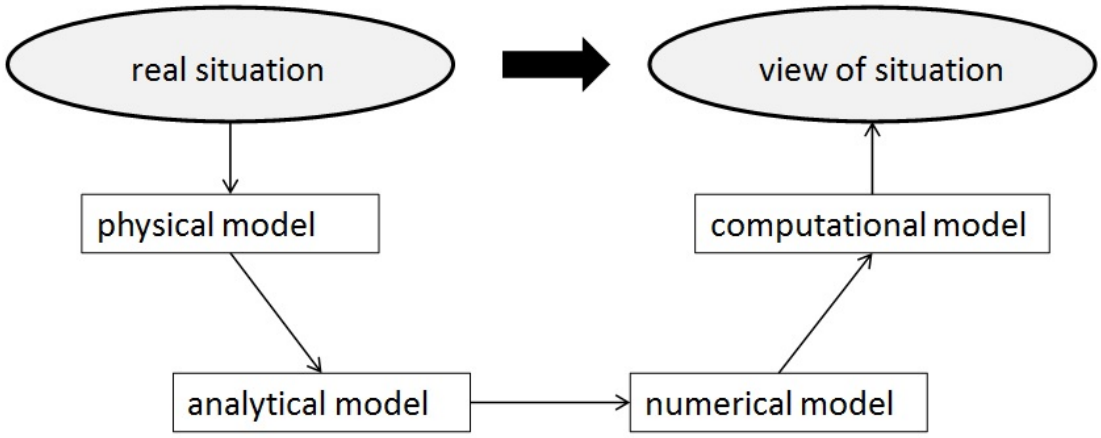


Figure 2.5: Process of model creation: reproducing the reality via a virtual model

The first step is the creation of the physical model where the user has to define all physical relevant influences which are taking effect on the regarded structure (definition of mechanical or thermal problem or both, etc). The user himself has to decide which physical factors are relevant for his model and which physical factors may be negligible small from case to case. It often makes sense to reduce the real occurrence in the first step already in order to facilitate the model and thus, to save engineering costs.

In a following second step, the user formulates analytical equations out of the physical factors which are influencing the model. The previous chapter (2.1.3) shows basic approaches for this purpose. Thus, the reality is reduced to an analytical model. Dependent on the kind of problem, the type of analytical equation may differ. Nonlinear problems, as we have got with the elastic-plastic deformation of an adhesive, are often described by dint of differential equations.

The next step of modeling is to discretize the analytical equations and to form a numerical model. For solid bodies the discretization is commonly processed by the finite element method (FEM), for fluids (liquid and gases) by the computational fluid dynamics method (CFD).
The FEM represents a physical problem by splitting an arbitrary structural solid body into several sections, the finite elements. This splitting can be executed in two different ways leading to two different kind of element meshes. On the one hand, a structured Cartesian mesh can be build up (figure 2.6), dividing the solid body into multiple rectangle or cuboid elements. On the other hand, the solid body can be meshed unstructured by using triangular elements, tetrahedron elements or combinations of different element forms.

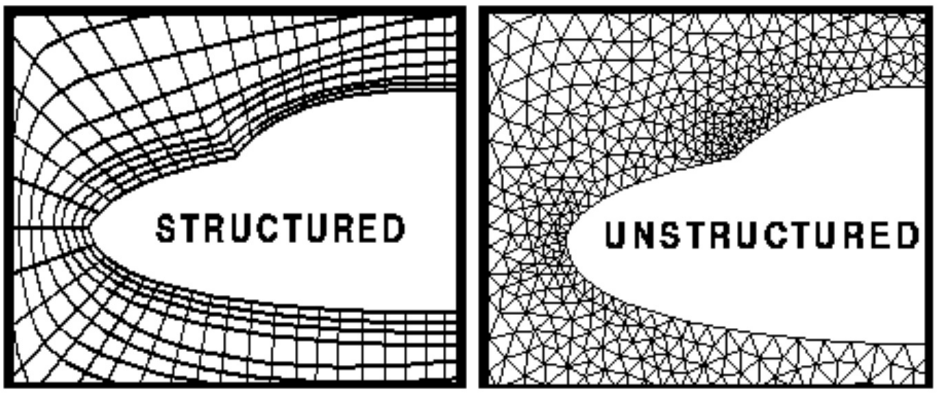


Figure 2.6: Different types of mesh structures for FEM and CFD; structured mesh (left), unstructured mesh (right) according to [45]

In addition to the elements nodal points, the gridpoints, are created automatically within a FEA, whereat each of these two objects has its proper meaning for the analysis.
The constitutive discretized equations are solved within an FEA corresponding to [18] at the nodal points situated at the corners or edges of the finite elements. In a three-dimensional model there are six equations for each nodal point (one for each translational

and one for each rotational degree of freedom). Summarizing up, the amount of nodes and with it the amount of degrees of freedom define the number of equations having to be solved for a FE-model.
The finite element, its kind, its property and its material is defining the kind of equation solved between the nodal points. In the following sections the most important element types for composite and adhesive modeling are presented. The explanation of the elements is based on the FE-library of MSC Nastran 2014 (s. [2]).

The local discretization is dependent on the element type. It represents local linear approximations of the constitutive equation for linear elements, which are used exclusively in this thesis. Thus, the element size should be adapted appropriately to the original analytical constitutive equations. In those local areas where the gradients of the constitutive equation change much, a fine element mesh is needed according to [18]
In reference to the constitutive equation of the adhesive stresses (s. figure 2) this would signify that the FEM-mesh over the adhesive layer has to be refined particularly at the edges where local stress singularities are expected.

### 2.2.2. Composite Modeling

Composites are conventionally modeled mostly out of shell elements. The shell elements correlate well with the commonly used planar analytical approach for composite analysis, the classical Laminate Theory (CLT).
If thick laminates are modeled or a three dimensional load path is existent, MSC Nastran recommends to use solid composite elements (s. [4]). Those solid elements are more appropriate to reflect the three-dimensional state of stress occurring in the laminate.
For the purpose of this thesis the composites are thus modeled by linear solid elements (CHEXA) with eight gridpoints at the element corners. For the composite modeling in Nastran a PCOMPLS-property card and the MATORT-material card are used.
Because solid elements generally tend to have an excessive bending stiffness, a certain amount of solid elements in elemental thickness direction is needed to predict the bending behavior of the composite correctly. This would unfortunately lead to a large increase of elements and gridpoints in the FEM-model and thereby to a crucial increase of computing costs.
For this reason MSC Nastran offers the possibility of solid shell composite modeling (s. [4]) where assumed strain functions correct the overly stiff bending behavior of the solid

elements. Hence, thick composites can be modeled with this technique by using only few composite elements in laminate thickness direction.
The solid shell composite elements represent the used element form to model composite layers within this thesis.

### 2.2.3. Adhesive Modeling

MSC Nastran offers several methods to model delamination of adhesive joints. One of the most promising methods is the Cohesive Zone Method (CZM) presented in this subsection.
Further approaches for adhesive modeling with the ability for delamination modeling are provided by the Virtual Crack Closure Technique (VCCT) and the Breaking Glue contact algorithm. The benefits and disadvantages of every method are listed within this section in order to understand why the CZM has finally been chosen as the most suitable approach.

#### 2.2.3.1. Virtual Crack Closure Technique (VCCT)

The VCCT originates from an energy based approach of Linear Fracture Mechanics (LFM). It can be traced back to Griffith' concept who stated that „for crack propagation, the rate of elastic energy release should at least equal the rate of energy needed for creation of a new crack surface“ according to [1]. This means that the necessary work to create a crack is compared with the existing strain energy in a structure.
In the VCCT the local nodal energy release rate is calculated by multiplying the forces which keep the crack tip together with the crack opening in a specific distance behind the crack tip.
This results in one major drawback of the VCCT. Corresponding to the stated concept, the crack propagation is calculated with the need of an existing crack opening so that there is no possibility to model the creation of new cracks according to [27]. Another drawback of this method is that problems arise if multiple delaminations interact in the same time (s. [19]).

Otherwise, positive experiences with the VCCT could be gained corresponding to the literature in the accurate prediction of adhesive failure. For instance Song et al. compare in [44] numerical methods to predict adhesive failure at mixed-mode bending specimens. The result of their comparison is that the numerical VCCT-method reflects the analytical approach of the adhesive failure very well.

#### 2.2.3.2. Breaking Glue

A further possibility to model delamination within MSC Nastran is the Breaking Glue contact method. While the VCCT did use an energy based approach, the Breaking Glue algorithm bases on a simple stress criterion.

$$(\frac{\tau_{shear}}{\tau_{max,shear}})^{exp_{shear}} + (\frac{\tau_n}{\tau_{max,n}})^{exp_n} \geq 1 \tag{5}$$

By using this approach, contact constraints are created between two adherends. According to [1] and [2], the contact constraints base on the Node-to-Segment contact algorithm in which the nodes of one adherend are constrained to the nodes of the other bonded adherend. The contact constraints are modeled in form of multi-point constraints (MPCs), which restrict the displacements of the touching adherends by defining additional equation in the constitutive equation of the models.
The relative simplicity of this approach leads to a fast computing time of the nonlinear analysis. Another advantage of the Breaking Glue method in MSC Nastran is that the user can define the exponents in the stress criterion so that the specific influence of normal and shear stresses can be varied.
A disadvantage is that the Breaking Glue algorithm does not permit to model the softening of the adhesive, which occurs in the highly loaded areas of adhesives according to [9]. A corresponding analytical approach, which takes the material nonlinearity of the adhesive into account is for instance the Hart-Smith's analysis according to [17]. An appropriate numerical model, which takes the material nonlinearity into account is supplied in MSC Nastran by the subsequently presented Cohesive Zone Method.

#### 2.2.3.3. Cohesive Zone Method (CZM)

Corresponding to [27], the concept of the cohesive zone method bases on Damage Mechanics. Its origins go back to Dugdale, Barenblatt and Hillerborg. Hillerborg introduced a tensile strength concept into his model allowing existing cracks to grow and even new cracks to arise. This is the most important improvement towards the VCCT-method. In addition the CZM combines a similar stress criterion as used in the Breaking Glue algorithm with an energy based approach allowing to model an adhesive damage behavior.

**Cohesive Zone length and cohesive element size**

The Cohesive Zone Method describes the use of interface elements, also called cohesive

zone elements (CZE) modeled between two surfaces at places where a delamination may arise. Delaminations may occur for instance between two adhesively bonded parts or inside a composite laminate. The delamination process of the CZM bases on a softening placticity zone, also called cohesive zone (CZ) as shown in figure 2.7.

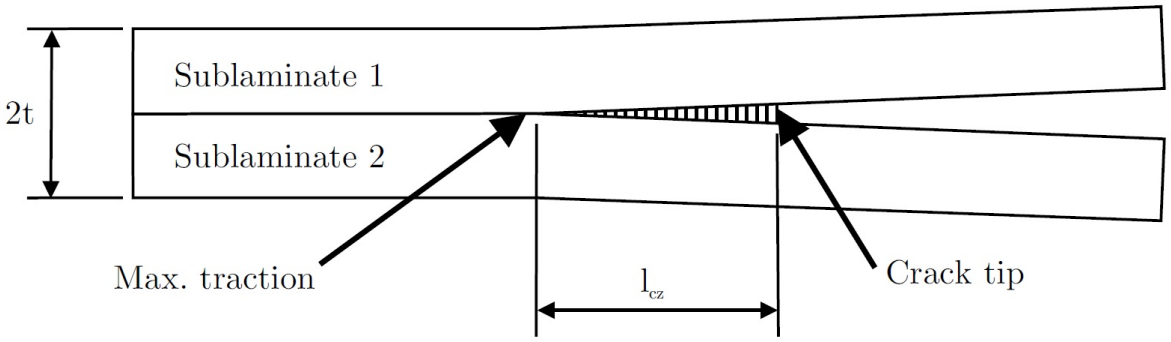


Figure 2.7: The cohesive zone is situated between the crack tip and the point of maximum traction in the interface layer (s. [25])

In this cohesive zone the interface elements deform plastically, while the rest of the interface elements outside of the cohesive zone deform elastically. The cohesive zone interface elements in MSC Nastran can be modeled three-dimensionally as well as planar with zero-thickness. Since only three-dimensional cohesive zone interface elements (CIFHEX-elements) are used for the modeling in this work, an equivalent element is shown in figure 2.8.

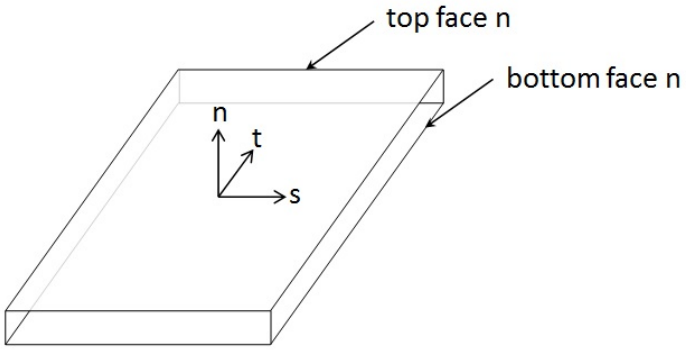


Figure 2.8: Three-dimensional cohesive zone element, with normal (n) and shear (s,t) directions

$$\nu_n = u_{n,top} - u_{n,bottom} \quad (6)$$

$$\nu_s = u_{s,top} - u_{s,bottom} \quad (7)$$

$$\nu_t = u_{t,top} - u_{t,bottom} \quad (8)$$

$$\nu_{res} = \sqrt{\langle \nu_n^2 \rangle + \nu_s^2 + \nu_t^2} \quad (9)$$

The zero-thickness element has the same behavior as the three-dimensional interface element, with the different that the initial thickness in normal direction n is zero. This makes it handy to insert the CZE in large existing FEM models which did not consider adhesive delaminations before.

As mentioned in the advanced analytical approaches in subsection 2.1.3.3, the elasticity and the eccentricity of the adherends lead to shear and peel stress maxima close to the edges of an adhesive layer in the cohesive zone. Hence, both stress distributions exhibit high stress gradients in this area. These high stress gradients require a minimum cohesive zone element length to predict the structural behavior accurately.
Previous studies according to A. Turon et al. (s. [25]) form an approach to determine the greatest possible cohesive zone element length $l_{CZE}$ by the length of the cohesive zone $l_{CZ}$ to still obtain accurate results.

$$l_{CZ} = M \cdot E \cdot \frac{G_{IC}}{\sigma_{max}^2} \tag{10}$$

In this context, $E$ is the transverse modulus of elasticity of the adhesive, $G_C$ the critical energy release rate, $\tau_{max}$ the maximum interfacial strength and $M$ is a factor varying between 0,21 and 1, depending on the chosen approach of cohesive zone length estimation corresponding to [25]. For the most common approaches $M$ is close or equal to $M$=1.
According to [24], the given approach can be chosen for determining the cohesive zone length for either pure normal or shear loading.
For the case of pure shear loading, the critical normal energy release rate $G_{IC}$ and the maximum normal interface strength $\sigma_{max}$ are just exchanged by the critical shear energy release rate $G_{IIC}$ and the maximum shear interface strength $\tau_{max,shear}$.
[25] recommends to place at least 3 CZE in the cohesive zone to predict the delamination behavior accurately, so that:

$$l_{CZE} = \frac{l_{CZ}}{3} = M \cdot E \cdot \frac{G_C}{\tau_{max}^2 \cdot 3} \tag{11}$$

Pursuant to [25], the resultant cohesive mesh size should for the modeling of typical graphite-epoxy composite adherends be smaller than 0,5mm. This would result to practical intractable problems for large structures.
In order to decrease computing costs and thus the amount of elements in an analysis, [25] presents a complementary approach to coarse the CZE-mesh further. It bases on

equation (11) and proposes to increase the CZE length $l_{CZE}$ by reducing artificially its critical maximum traction $\tau_{max}$.

However, if pure shear loading (Mode II, Mode III) is present, [25] and [44] detect an insensitivity of the CZE-mesh towards the strength of the simulated adhesive joint. Hence, the increase of the CZE-size primarily has an effect on the delamination, if the CZEs are loaded on peel conditions (Mode I).

**Material law for CZE**

In general, a cohesive zone interface element relates its interface stresses $\tau$ to the elemental opening displacements $\nu$ in form of traction-displacement laws. The opening displacement of a CZE can be determined by subtracting the displacement of two opposed element surfaces along equation (6) to (8).

There exist several kinds of the traction-displacement laws, as for instance a bilinear, an exponential or a linear-exponential. The most widely used traction-displacement law is the bilinear one which is the used adhesive material law in this work and thus presented in figure 2.9.

The relevant material values for a CZE are named in the depicted bilinear-traction-displacement law.

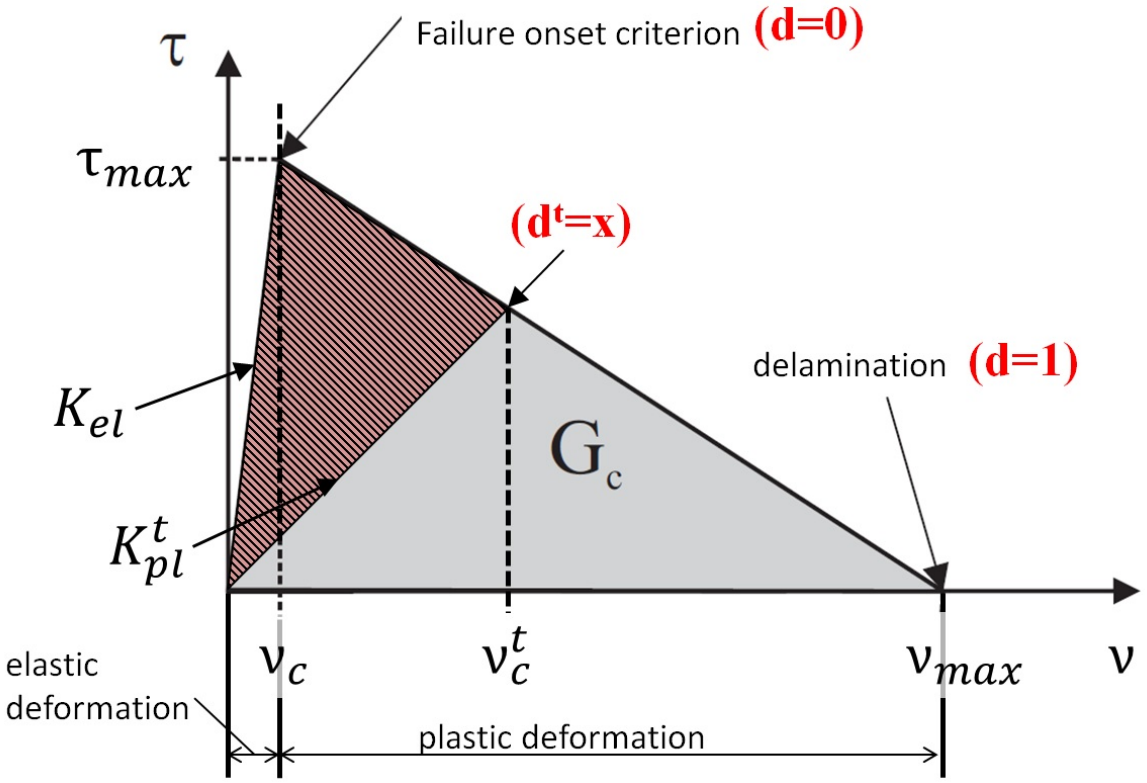


Figure 2.9: The bilinear traction-displacement law

The bilinear-traction law of a CZE is divided into two linear parts.
The first part represents the linear-elastic material behavior of the adhesive, while the second one describes the plastic material behavior. Therefore the elastic material behavior occurs up to a maximum traction $\tau_{max}$ in the CZE. At this point the CZE has a critical opening displacement $\nu_c$. A further element opening than $\nu_c$ initiates the plastic material behavior.

Next to the stresses and the element opening displacements, the element stiffness $K$ is described in the material law. If a point on the bi-linear traction law represents the present stress state of a CZE, the straight line connection to the point of origin shows its present stiffness $K_{pl}^t$.

$$K_{pl}^t = \frac{E^t}{th_{CZE}} \cdot \alpha = (1 - d^t) \cdot K_{el} \tag{12}$$

The element stiffness remains constant at $K_{el}$ as long as the present state does not exceed the failure onset criterion at a maximum resultant traction $\tau_{max}$.

Once the failure onset criterion is exceeded, the plastic deformation starts and the element stiffness reduces. The initial thickness of the CZE $th_{CZE}$ determines the CZE-stiffness with the relevant modulus of elasticity $E^t$. A. Turon et al. propose this equation introducing the stiffness factor $\alpha = 50$. This stiffness factor serves to provide a reasonable element stiffness without running into numerical problems (e. g. spurious oscillations) according to their investigation (s. [25]).

The zero-thickness cohesive zone interface element would theoretically condition an infinite initial element stiffness along equation (12) leading to the same numerical problems. Thus, a different stiffness estimation should be used for these two-dimensional interface elements corresponding to [19].

Furthermore the critical energy release rate $G_C$, also called fracture toughness, is described by the surface underneath the traction-displacement-curve, and can thus be described using the bi-linear material law as:

$$G_C = \frac{\nu_{max} \cdot \tau_{max}}{2} \tag{13}$$

Once the stresses in the adhesive layer reach the critical stress level $\tau_{max}$, the CZEs start to dissipate energy and the adhesive deforms plastically. The dissipated energy at the load increment $t$ of the applied nonlinear analysis is demonstrated by the hatched area in figure 2.9. The remaining critical energy release rate reduces to the unhatched area.

The details for the executed numerical nonlinear analysis are explained in the appendix in section A.2.2.

The above mentioned relevant material parameter for defining the material law of a CZE are summarized in the table below:

Table 1: Relevant material parameter for a Cohesive Zone Interface Element (CZE)

| **Name** | **Parameter** | **Unit** |
|---|---|---|
| modulus of elasticity (normal direction) | $E$ | MPa |
| shear modulus | $G$ | MPa |
| maximal stress in normal direction | $\sigma_{max}$ | MPa |
| maximal stress in shear direction | $\tau_{max,s}$, $\tau_{max,t}$ | MPa |
| critical energy release rate in normal direction | $G_{IC}$ | N/mm |
| critical energy release rate in shear direction | $G_{IIC}$ | N/mm |
| thickness of adhesive layer | $th_{CZE}$ | mm |

They are entered in MSC Nastran in form of the MCOHE-material card which is connected to the CIFHEX-CZEs by using the PCOHE-property card. Within the PCOHE-property card of the elements, the Newton-Coates/Lobatto integration scheme has been chosen for the numerical determination of the constitutive equation referred to the recommendation of MSC Nastran (s. [2]).

**Mixed-Mode loading of CZE**

In general, adhesive layers may be loaded by three different modes all of presented in the following image.

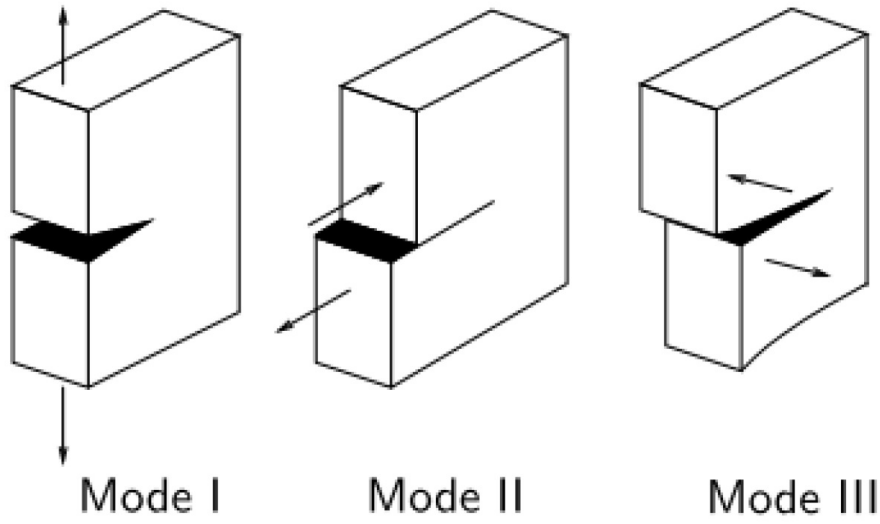


Figure 2.10: Load conditions and associated failure modes for an adhesive layer: tensile (Mode I); shear (Mode II, Mode III) corresponding to [42]

As mentioned, adhesive joints are preferably designed to transfer shear loading according to Mode II or Mode III. Adhesive joints are, however, always exposed to a combined modal loading where the above depicted load paths interact.
This leads to the fact that a single critical stress $\tau_{max}$ in one load direction is not sufficient anymore to determine the failure onset.
Thus, according to [26] a mixed-mode criterion must be established when shear and tensile stresses interact in the adhesive. A failure-onset-criterion which satisfies the consideration of mixed-mode loading conditions is in compliance with [27] the quadratic interaction criterion ($QIC$). It is also known as „Ye's criterion“ and it is very similar to

the stress criterion of the Breaking Glue algorithm (s. equation (5)):

$$QIC = (\frac{\langle\sigma\rangle}{\sigma_{max}})^2 + (\frac{\tau_s}{\tau_{max,s}})^2 + (\frac{\tau_t}{\tau_{max,t}})^2 = 1 \tag{14}$$

If the failure onset criterion is reached, the damage propagation of the CZEs starts. The damage of a CZE is expressed in Nastran via the scalar damage value $d$. Until the point of failure onset is reached, this scalar damage value logically is equal to $d$=0. Exceeding this failure onset criterion in a CZE, its damage value $d$ increases and can be expressed by the element opening displacements along equation (15) according to [27]:

$$d = \frac{\nu_{max} \cdot (\nu^t_{res} - \nu_c)}{\nu^t_{res} \cdot (\nu_{max} - \nu_c)} \tag{15}$$

If the maximum opening displacement $\nu_{max}$ is reached by a CZE, its scalar damage value rises to its maximum $d$=1. At that point the cohesive element stiffness $K^t_{pl}$ is decreased to zero (along with equation (12)) and the delamination of the tied adherends is completed.

The material values of adhesives which are needed to fill the constitutive laws of the CZEs vary according to the different modal adhesive behavior in shear and normal direction. Out of these, traction-displacement laws can be created in a first step for pure mode loading.
Since in practice most adhesive layers are loaded in a mixed-mode condition, a resultant traction-displacement law is essential. The resultant opening displacement of a CZE in mixed mode loading $\nu_{res}$ (pursuant to equation (9)) is a combination of an element opening in normal (n) and both shear directions (s,t). (In the elemental normal direction only a positive opening displacement is reasonable for delamination modeling so that the Macaulay brackets $\langle\rangle$ are used.) The resultant bilinear traction law is constructed dependent on the specific mixed-mode ratio $\beta_{MixedMode}$ (according to [27]) over the resultant opening displacement $\nu_{res}$:

$$\beta_{MixedMode} = \frac{\sqrt{(\nu_s)^2 + (\nu_t)^2}}{\sqrt{(\nu_s)^2 + (\nu_t)^2} + \langle\nu_n\rangle} \tag{16}$$

The resultant bilinear traction law for mixed-mode is displayed in figure 2.11.

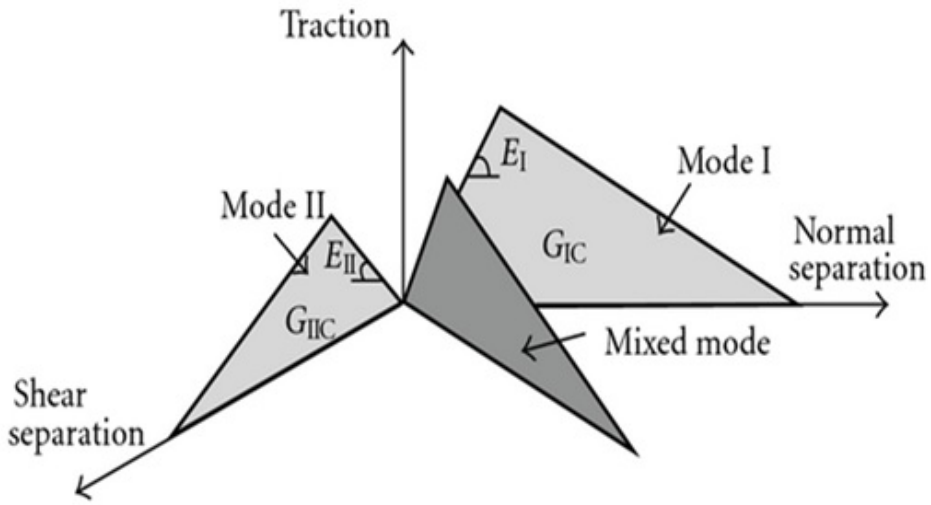


Figure 2.11: Resultant bi-linear traction law for a specific mixed-mode ratio

Since the mixed-mode ratio may change during delamination growth (according to [27] and [44]) it is not reasonable to present one specific traction-law for a certain mixed-mode ratio at a given point of the simulation. Instead, it is common to just representatively show the pure mode traction laws in normal and in shear direction, as they can be created out of the material tests.

As the CZEs just differ between shear and normal loading (but there are three modal loading conditions (figure 2.10)), both possible shear modes are merged to one resultant shear in the adhesive. The shear stresses of Mode II $\tau_s$ and Mode III $\tau_t$ are hence combined to a resultant occuring shear stress $\tau_{res,shear}$:

$$\tau_{res,shear} = \sqrt{\tau_s^2 + \tau_t^2} \tag{17}$$

The subsequent chapter investigates the correct creation and validation of the bilinear cohesive material laws.

# 3. Determination and validation of cohesive zone material parameter

This chapter is dedicated to show how adhesive material parameter are entered to the bilinear cohesive material law of the CZEs in a FEM-model.
Once the definition of the CZE-parameter is set, the behavior of the CZEs shall be verified in the second section of this chapter through a pure mode test in form of the Single Lap Shear (SLS) test.

## 3.1. Definition of cohesive zone material parameter

The choice of the adhesive material input data for the CZEs is done with the aid of adhesive material tests. For pure Mode I (tensile-loading) as well as for pure Mode II and Mode III (shear-loading), suitable tests have to be chosen to obtain the necessary material input of table 1.

According to [35], a Tinius Olsen H5K-S UTM tensile machine and an MTS universal testing machine can be used for the determination of the fracture toughness $G_C$ in tensile and shear mode. The fracture toughness for the relevant adhesives in this thesis have been taken out of the specified document (s. [35]).
Typical tests for the determination of the modulus of elasticity $E$ and the maximum normal stress $\tau_{max,n}$ are bone sample tests or flat-wise tensile strength tests, whereas lap-shear-tests are most often used to determine the shear modulus $G$ and the maximum shear stress $\tau_{max,s}$.

These tests, however, bring up the material specific stress-strain laws which do not print out the precise required input-parameter for the CZE material law. Thus, the determination of the bilinear CZE parameter shall be discussed below at the example of a typical shear stress-strain law for an arbitrary adhesive material as shown in figure 3.1.
The European Space Agency (ESA) defines the commonly used ultimate and limit loads in the aeronautical sector for adhesive materials at the material specific stress-strain law corresponding to [9]. In doing so, the nonlinear stress-strain output of a test is usually approximated by two linear curves (dashed lines). The ESA proposes several methods to create the approximation of the original testing curve by the named two-part division.

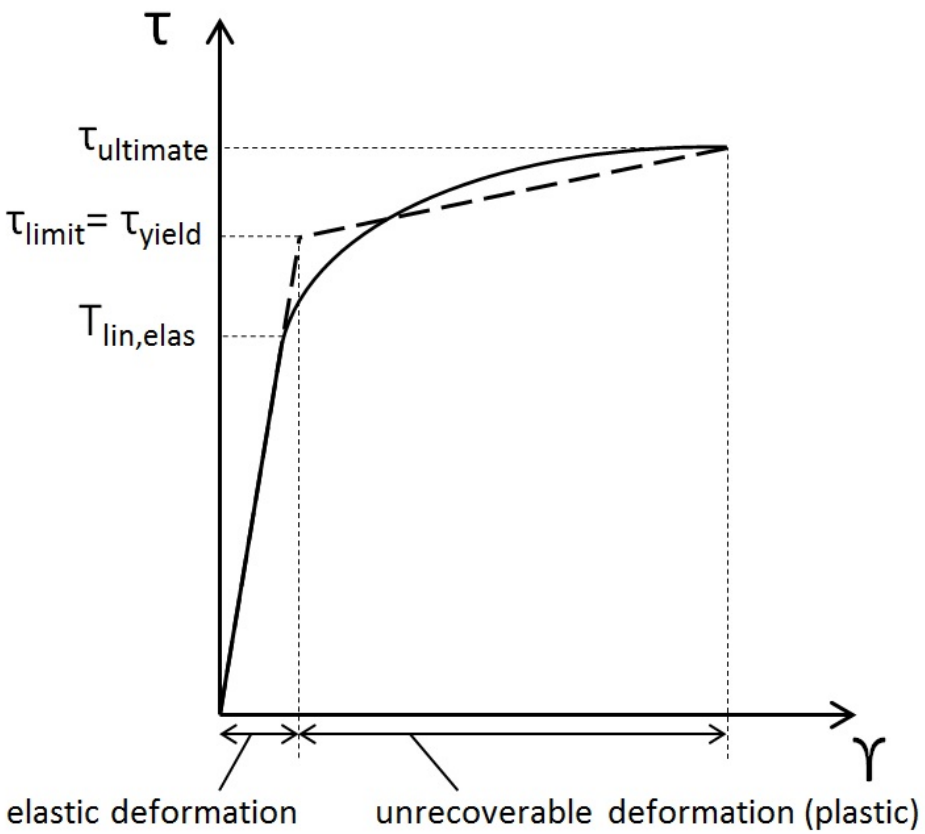


Figure 3.1: Typical shear stress-strain behavior (continuous line), and linear approximation of the shear-stress-strain law (dashed line)

The recommended method pursuant to [10] is to take first the elastic gradient of the stress-strain-curve for the first linear part to reproduce the material modulus correctly. Secondly, the knee between both linear parts has to be determined. In this favor, the recommendation for it is based on the strain recovery of the adhesive. Hence, the knee represents the yield strength of the adhesive $\tau_{yield}$ at the onset of unrecoverable deformation.
According to [9], the limit load $\tau_{limit}$ of the adhesive should be defined at this precise point.
Ultimate load is reached at the highest possible stress on the curve, i. e. at the failure stress $\tau_{ultimate}$.

With reference to the used bilinear cohesive material law, the point of interest in the approximated stress-strain-law is at the yielding strength $\tau_{yield}$, because at this point

the unrecoverable plastic deformation starts. Thus, we define the same point P($\nu_c$,$\tau_{max}$) in the CZE-material law (s. figure 2.9) for the onset of plastic deformation. The modulus of elasticity E of the CZE-material is precisely defined by the gradient of the first part of the linear-approximation.

Besides, the cohesive zone method respects a simple relation between the CZE-input parameter corresponding to [36] for Mode I-:

$$G_{IC} = \frac{th_{adhesive} \cdot (\sigma_{max})^2}{2 \cdot E} \tag{18}$$

and for Mode II-loading:

$$G_{IIC} = \frac{th_{adhesive} \cdot (\tau_{max,s})^2}{2 \cdot G} \tag{19}$$

Equation (18) and (19) consequently form a ratio of modulus $E/G$ dependent on the modal ratio of fracture toughness $\beta_2 = G_{IIC}/G_IC$ and on the modal stress ratio $\beta_1 = \tau_{max,s}/\tau_{max,n}$ in the following way:

$$\frac{E}{G} = \frac{G_{IIC}}{G_{IC}} \cdot \frac{(t_{max,n})^2}{(t_{max,s})^2} = \frac{\beta_2}{(\beta_1)^2} \tag{20}$$

On the one hand, MSC Nastran offers the input of only five CZE-material parameters at the usage of the bilinear cohesive material law , so that the sixth one has to follow the equation (20).
On the other hand, this relation offers a useful approach to verify the quality of the chosen CZE-input parameters. The different executed material tests of an adhesive should thus result in a consistent solution of equation (20). If the executed material tests do not conform in this regard, a selection of the CZE-parameters has to be found which corresponds best to the real adhesive behavior.
Furthermore, it should be studied whether the numerical definition of the adhesive as it is implemented in the CZM by equation (20), can also be determined for any real adhesive.

## 3.2. Comparison of material tests and material simulation

The validation of the chosen material inputs for the CZM-models shall be done by comparing their stress-strain-curves with those of the material tests. Representative for a typical pure-mode-model, the stress-strain-curve of the Single Lap Shear (SLS) specimen is analyzed. Some of the tests of the SLS have been executed at the university of Landshut in cooperation with the Airbus Group (s. [34]).

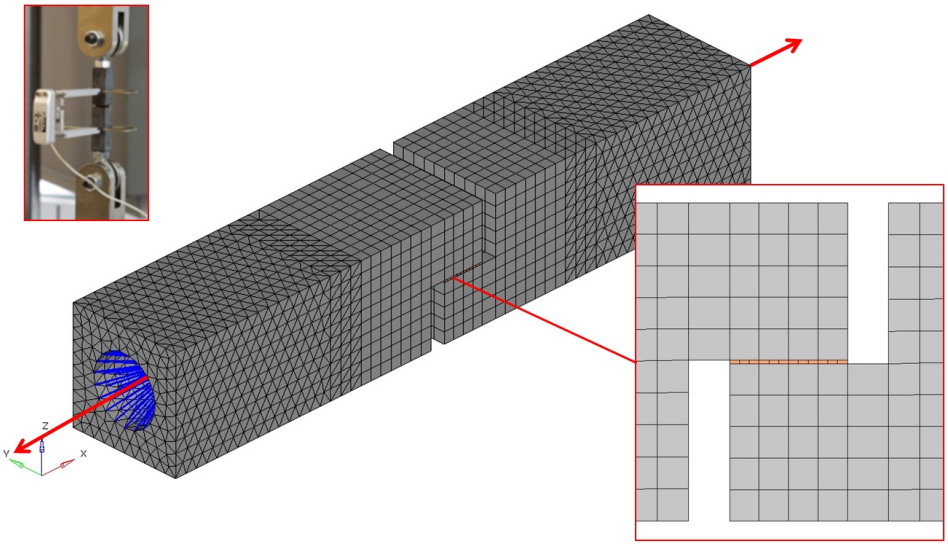

Figure 3.2: The FEA model of a Single Lap Shear specimen according to [33] (the loading of the model is done by the application of displacements in longitudinal direction); the cut out on the right shows a side view (xz) on the adhesive layer; in the top left corner the test specimen of the SLS is imaged

The upper depicted configuration of the SLS-model (s. 3.2) is an adhesive single-mode-model due to the following reasons. First, the adherends have a large thickness so that their bending stiffness is high. Secondly, the steel of the adherends has a much higher modulus of elasticity than the adhesive. These two facts lead to the condition that the model hardly shows any of the bending effects mentioned in figure 2.3 (c). Additionally, the relatively high tensile stiffness of the adherends leads approximately to the model simplification of rigid adherents (a) in figure 2.3.
Consequently, the shear stress distribution can be approximated by the analytical rigid adherend model presented in subsection 2.1.3.1. In this approximation the shear stress distribution $\tau_{shear}$ does not show any stress singularities at all, because the stress is estimated as constant over the whole adhesive length $l_{joint}$.

That there are no distinct stress maxima in the adhesive layer is numerically proven in a FEM-model of the SLS with a refined adhesive mesh in the appendix B.1.
Thus, the adhesive shear stress can be approximated for the whole adhesive layer according to equation (1).
The shear strain $\gamma_{shear}$ is equally averaged over the complete adhesive layer. The averaged displacements $u$ in longitudinal direction are for this purpose determined for the adhesive top surface ($u_{top}$) and for the adhesive bottom surface ($u_{bottom}$). In consideration of the thickness of the adhesive layer $th_{adhesive}$, the averaged shear strain $\gamma_{shear,xz}$ of the adhesive can be calculated as follows:

$$\gamma_{shear} = arctan(\frac{|u_{bottom} - u_{top}|}{th_{adhesive}}) \tag{21}$$

Within this section, two adhesive materials are presented, for which the suitability shall be proven; the mixed EA9395-EA9396 paste adhesive, henceforth called „Mojo-Mix“, and the EA9695 film adhesive. For both adhesives, material data is attached in the appendix in table 7 and table 8 whereat the origins of the used material values are specified.
These two adhesives have been chosen, because both will later be used in the testing and simulation of larger components.
Their resultant bilinear-traction laws for tensile and shear mode are shown in the following figures:

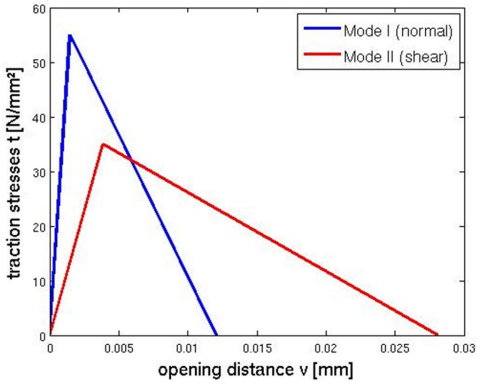


Figure 3.3: Single mode bilinear traction-laws of „Mojo-Mix“ adhesive on CLS-specimen

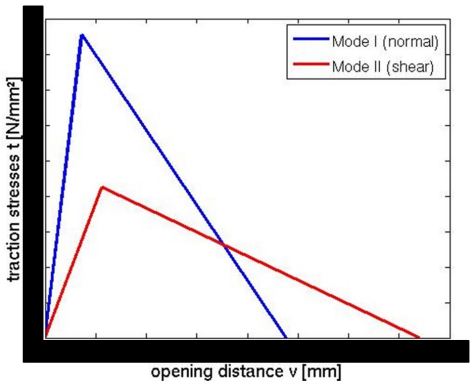


Figure 3.4: Single mode bilinear traction-laws of Hysol EA9695 adhesive on T-Stringer specimen

These bilinear-traction laws form the numerical material input for the CZEs in form of Nastran MCOHE-cards in the models according to [2]. In this regard the used MCOHE-cards for the representation of both adhesives are depicted in table 10 and 11 in the

appendix. Also the applied PCOHE-property-card is specified (s. 9).

The test and the simulation results of the SLS are subsequently presented for both adhesives. In doing so the resultant stress-strain-curves are superposed to each other to determine the suitability of the CZE-material input.

In figure 3.5 and 3.6 the green colored stress-strain-curves represent the simulated re-

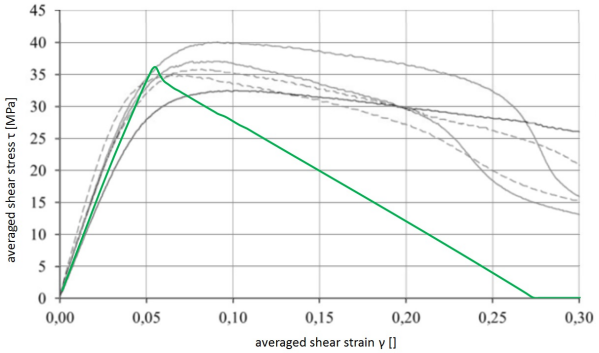


Figure 3.5: Shear-stress-strain-curve of Mojomix (grey curves are test results of SLS according to [34]; green curve represents the FEM results)

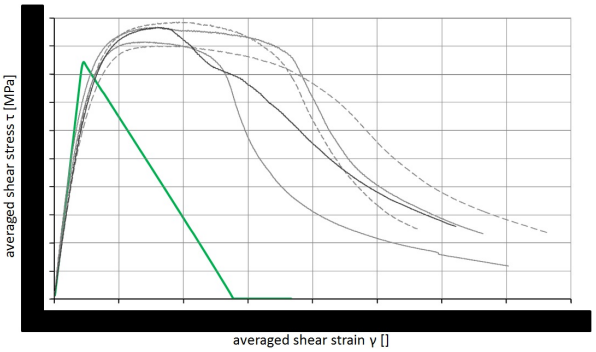


Figure 3.6: Shear-stress-strain-curve of Hysol EA 9695 (grey curves are test results of SLS; green curve represents the FEM results)

sult, while the gray curves represent the results obtained by the tests.

For both adhesives, the simulations provide good results for the elastic part of the adhesive behavior. The elastic behavior represents a very important part in the aircraft validation process of a structure, because in the daily operation a structure should not exceed the end of its elastic deformation (limit load). The elastic shear modulus which is proportional to the gradient of the curves in the linear elastic area fits well to the test curves and the CZEs start to gain damage at their implemented yield strength.

Looking at equation (12) it has to be stated that the recommended stiffness factor $\alpha$ = 50 does not satisfy the elastic behavior of the adhesive model. Instead, the 50-fold stiffness of the model would reduce the elastic strain deformation of the adhesive and thus, the simulated CZE-stress-strain-curve would not fit to the test-curves anymore. If the deformation of the SLS is scaled up by the graphical scale factor GSF=1000, the different behavior can be visually identified:

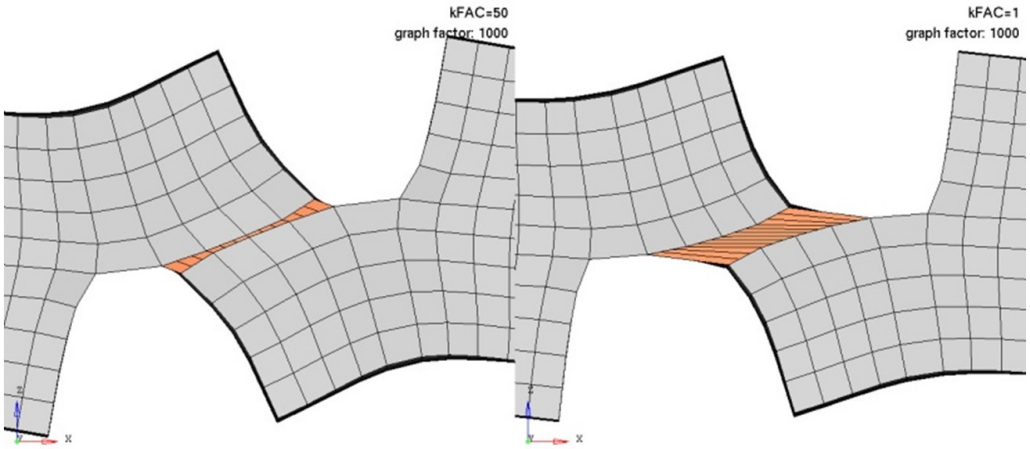


Figure 3.7: Sideview of deformed SLS-model (graphical scale factor GSF=1000): influence of stiffness factor $\alpha$ (left: $\alpha$=50, right: $\alpha$=1)

Thus, the cohesive models in this work have an implemented stiffness factor $\alpha$=1, in opposition to the recommendation of [25].

The plastic behavior in contrast to the elastic behavior can not adequately be reproduced. For both adhesives, the tests plastically deform more than their corresponding FEM-model. This may have two reasons. First, the fracture toughness $G_C$ of both adhesives having been determined in [35] may not match the tested SLS-specimen. According to [42], an enlargement of the fracture toughness parameter would bring the CZM-results closer to the test results. It would lead in this regard to an enlargement of the plastic deformation behavior depicted in figure 2.9.
Secondly, the simulation using a bilinear CZ-material law is not intended to perfectly reproduce the test stress-strain-curves which do not show the bilinear characteristics.
Instead, it is rather important to precisely predict the accurate failure load of an adhesive joint. Since the stress-plots of the SLS are created by equation (1) for the test curves as well as for the simulation curve, the failure load of the tests and of the simulation correlate with each other.

# 4. Investigation on the Cracked Lap Shear specimen (CLS)

The Cracked Lap Shear specimen (CLS) shall be analyzed next. It satisfies the element level representing the second level of the validation pyramid in figure 1.2. At first glance, the CLS-model may geometrically not look more complex than the previously presented SLS-specimen.

Indeed, the CLS-specimen is constructed out of thin composite plates which allows a bending effect due to the load conditions of the specimen. Thus, its adhesive layer should sustain a mixed-mode loading condition.
The CLS-specimen has been chosen in this thesis for the element level of the validation pyramid, because there have been already some previous investigation in the Airbus Group company on this model. Hence, several test results and analysis results do already exist.

After a brief presentation of the specimen including its geometry and the used materials, the focus of the CLS analysis is put back to the comparison of the simulated FEM-results towards the test results.

## 4.1. Geometry

In general, the CLS-geometry is based on four different components depicted in figure 4.1. There is one bottom plate, the strap covering the full length of the sample having a thickness of 3,0mm. On top of it on the right hand side another 3,0mm thick plate, the lap, is being fixed. The lap is shorter than the strap. While both plates end flushly at the right end, the left end of the lap is limited on the top surface of the strap. The fixing between both plates is done by an adhesive layer, the bondline, of 0,3mm thickness $th_{adhesive}$. These three components are representing the adhesive joint in which the failure is going to be induced. To control the start of the failure, the bondline is formed in a zigzag shape on its left edge (pursuant to figure 4.1) called the trigger.

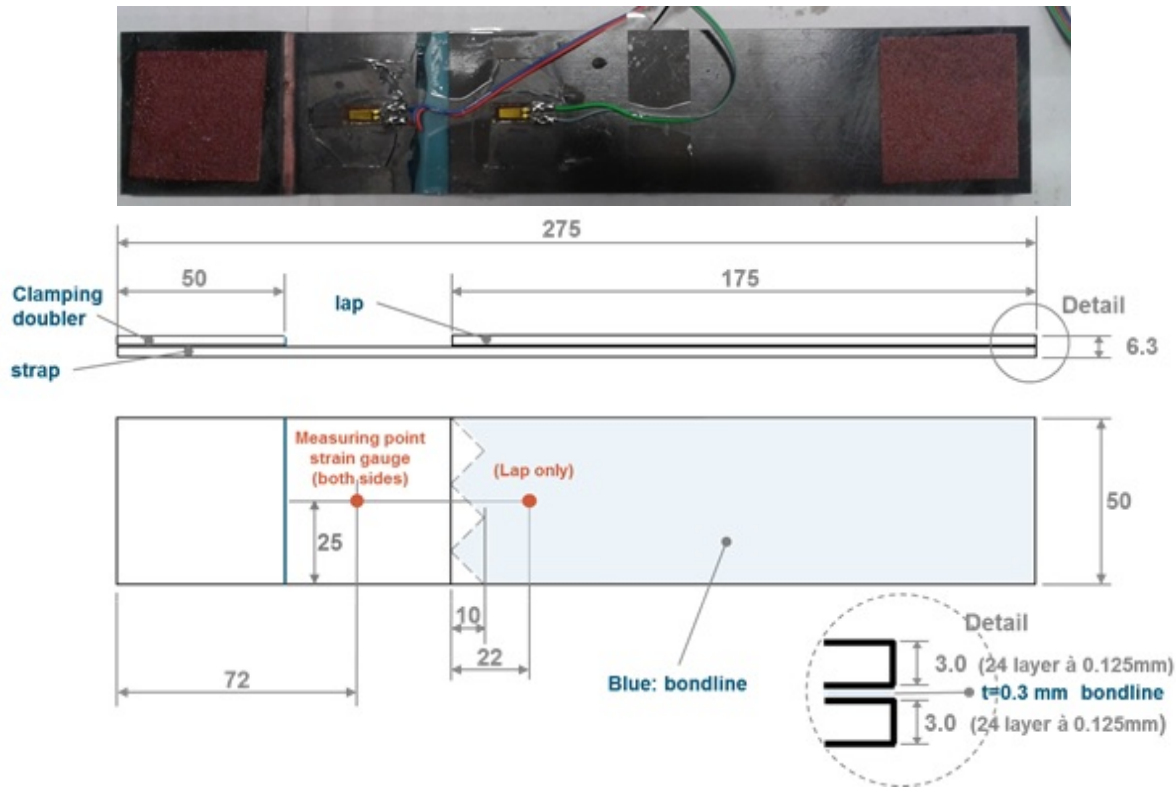


Figure 4.1: CLS-specimen of tests (top) / geometrical dimensions of the CLS-specimen (bottom)

For a better fixation in the mounting, there is a quadratic plate called clamping doubler bonded on top of the left strap side. The clamping doubler thickens the sample on the left side of the CLS so that both ends have a similar form and opening distance in the mounting.
The load implementation in the model is done by an applied displacement along the longitudinal axis of the component. While the right bracket of the mounting remains at a fixed position, the left bracket moves to the left side.

The whole sample has a uniform width of 50mm. Strain gauges are positioned on the surfaces of the lap and the strap as specified in figure 4.1.

## 4.2. Material Properties

All the plates in the CLS-sample are made out of similar CFC-laminates. One laminate is fabricated out of 24 unidirectional prepreg-layers, while every layer has a thickness of

0,125mm according to [23]. The unidirectional layers are build up on top of each other with a rotational angle of 45°. This leads to the following stacking sequence:

$$[(0/45/90/135)]_{3S}$$

The unidirectional (UD) layers of these composites are made out of the carbon fibres of the type "IM7" and an epoxy resin called "Hexcel 8552". A material data sheet for an unidirectional layer is attached in the appendix 12. The extracted material properties of each unidirectional layer are shown in table 2.

Table 2: Material parameter of Hexcel IM7/8552 UD-prepreg according to [23]

| **Parameter** | **magnitude** |
|---|---|
| $E_{11}$ | 160000MPa |
| $E_{22}, E_{33}$ | 9000MPa |
| $G_{12}, G_{31}$ | 4500MPa |
| $G_{23}$ | 3215MPa |
| $\nu_{12}, \nu_{13}$ | 0,32 |
| $\nu_{23}$ | 0,4 |

For the adhesive layer the paste adhesive „Mojo-Mix" is used as studied in the previous chapter 3 at the example of the SLS-specimen.

## 4.3. Test results

The considered tests of the CLS-specimens have been run at the university of Augsburg. Corresponding to [20] it has been observed that a small offset in normal direction appeared at the clamping doubler while loading. The model was loaded by the application of a displacement in longitudinal direction at the side of the clamping doubler. The travel speed of the moved clamping bracket has been 2mm/min.

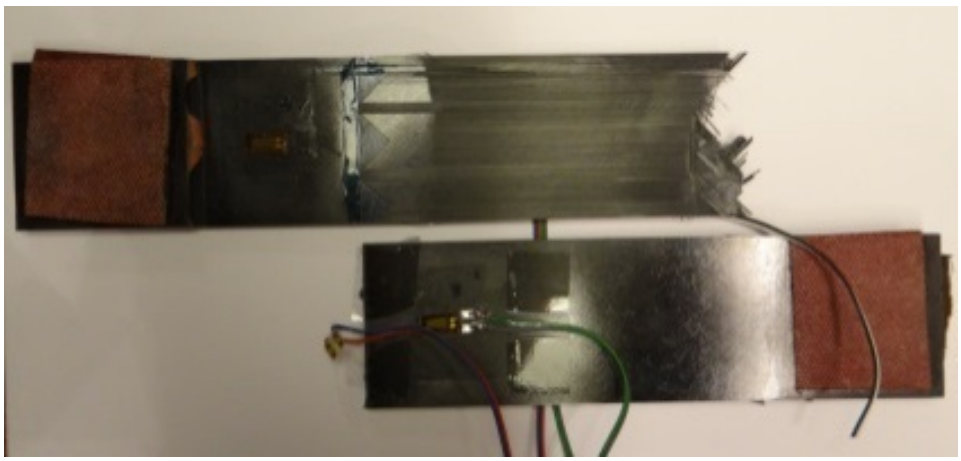

Figure 4.2: failed CLS-specimen after loading

The failure of the specimen appeared at a machine travel of about 7,5mm, representing a tensional force of $F_{test,crit}$ = 55kN. Figure 4.2 shows the cracked CLS-specimen. The reported test results are shown in figure 4.3. Additionally [20] specifies the quality of failure, saying that the failure arises in the bond line at the trigger and that it propagates for about 20mm. Afterwards the failure shifts to the first 0°-ply of the strap composite plate and finally propagates through this ply.

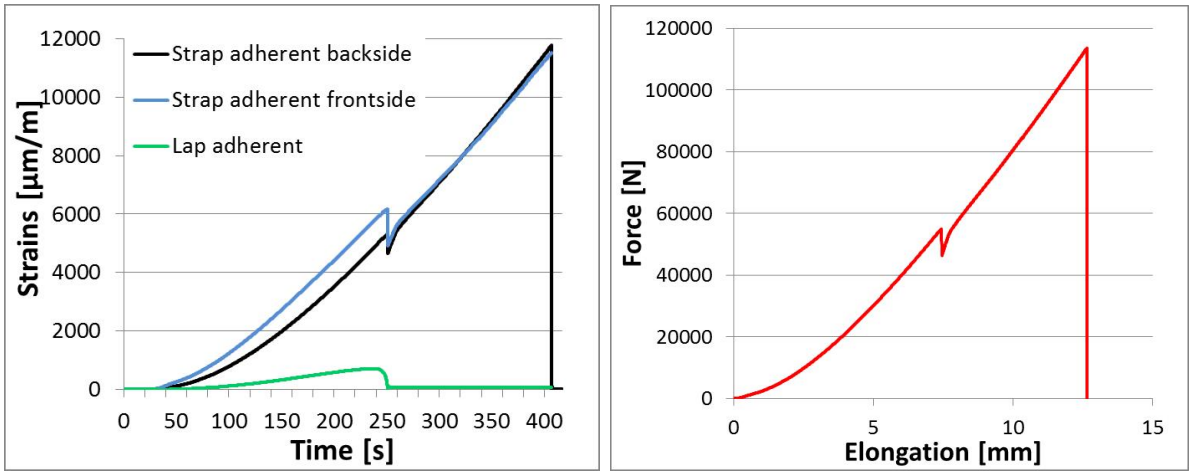


(a) Strain results of the fixed strain gauges

(b) Load-displacement-curve of CLS test

Figure 4.3: Test results of CLS under tensional loading condition

The load-displacement curve shows some non-linearities during the first phase of loading to about 3mm. These non-linearities result from the geometric non-linearity of the CLS and from slipping effects at the clamping brackets. Having reached 3mm of applied dis-

placements the CLS-specimen reacts linear until the failure of the CLS occurs.

With the aid of strain gauges, strain measurements could be recorded which are presented in figure 4.3(a). The strain at top face of the lap reports much smaller strains than the strain gauges at the strap faces, because the CLS has a much higher stiffness at that place due to its higher thickness. Additionally, the strain at the lap decreases abruptly to zero at the point of failure initiation. Since the load of the specimen is not transferred anymore through the delaminated part of the lap, the strain behavior of the lap can be explained.
The strains on both faces of the strap differ from each other. While the load is increased permanently, the CLS-specimen starts bending slightly thanks to its excentricity. The bending causes higher strains on the strap top face than on the strap bottom face. After the appearance of the failure, this effect is not witnessed anymore, which means that the position of the strain gauges is not subjected to the bending effect any further.
The abrupt change of the measured strains and the measured load indicate that the delamination of the CLS has quickly been proceeded.

## 4.4. Simulation

In this place the FEM-model of the CLS will be introduced. The cohesive zone model presents the major part of the CLS-investigation. A CLS-model using the Breaking Glue contact approach is created as well whereat its results are attached in the appendix C.2. Additionally, a mesh study with different meshes of the adherends and the adhesive has been conducted so that the influence of the element size on cohesive elements can be studied further. The cohesive modeling parameters in MSC Nastran have been varied to get an impression about their influences on the simulation.

### 4.4.1. Model specification

The basic model of the CLS-specimen has an average element edge size of $l_E$ = 2mm for the composite elements and for the CZEs. All the composite plates, strap, lap and clamping doubler are modeled by two elements in the thickness direction of the component. The adhesive layer is modeled with respect to its thickness $th_{adhesive}$ = 0,3mm equally to the SLS-model by three-dimensional CIFHEX-CZEs. As shown in figure 4.4, each node of the cohesive elements is connected directly with a CHEXA

element node of the adjacent congruent composite plate. The lap composite elements have been masked partly in order to get a better view of the CZEs positioned between strap and lap. All in all, the basic CLS-model consists out of 13723 elements and 18354 nodes. 2097 elements are CZE with the nonlinear MCOHE-material, the remaining ones are CHEXA composite elements with a linear-elastic material behavior.

The black triangles represent the clamping conditions in the model. The red arrows at the element nodes at the side of the clamping doubler represent an applied tensional force which is used alternatively to the applied tensional displacement constraint. In z-direction (normal-direction) the clamping brackets apply negative displacements of 0,0063mm, which represents 1 promille of the undeformed part thickness. This negative displacement simulates the pressure of the clamping brackets.

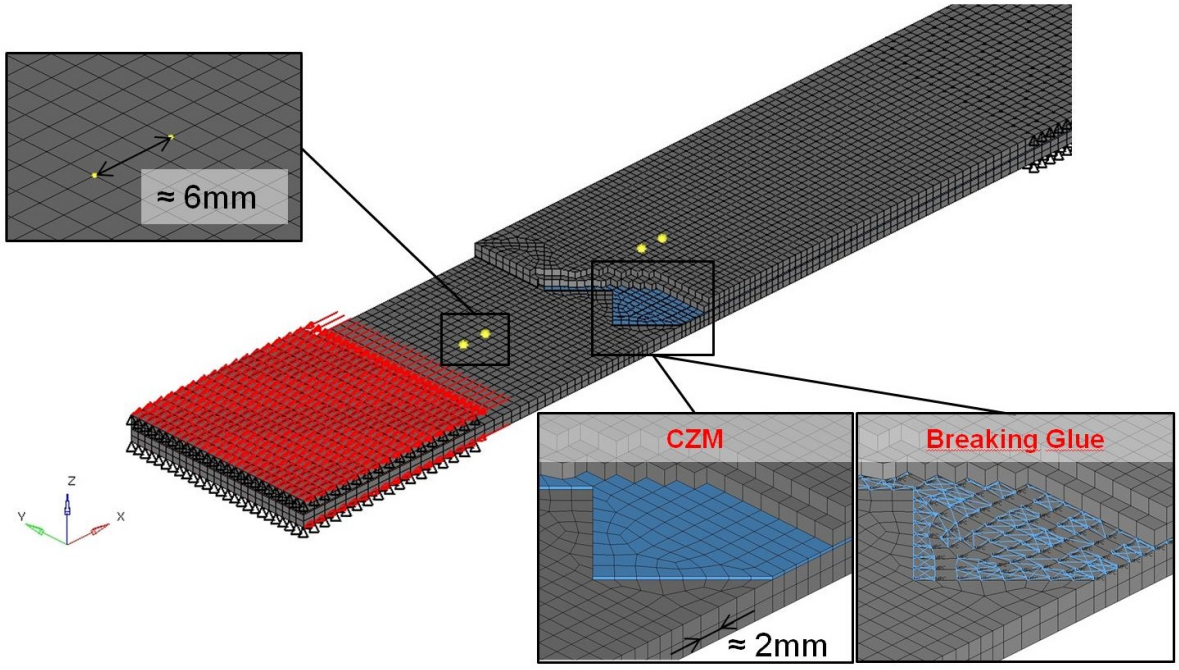


Figure 4.4: CLS model created via Hypermesh

The yellow marks show the positions between which a strain gauge is fixed on the test specimen. On the backside of the strap the third strain gauge is positioned. The strains $\varepsilon_{straingauge}$ of the CLS-model at the specified strain gauge positions are calculated by the printed displacements $u_{straingauge}$ of the strain gauge front and end points (equation 22).

$d_{straingauge}$ defines the undeformed strain gauge length.

$$\varepsilon_{straingauge} = \frac{u_{straingaugefront} - u_{straingaugeend}}{d_{straingauge}} \tag{22}$$

### 4.4.2. Failure

Analog with the test results, the simulation results are plotted and printed in figure 4.5. The deformation state at an applied displacement of 0,5mm is shown on the left side with a graphical scale factor GSF=10 which means that the shown deformation is ten times as high as the calculated real deformation. The fully damaged CZEs are masked. On the right side of the image, the strain and load result curves are printed over the applied displacements in longitudinal direction.

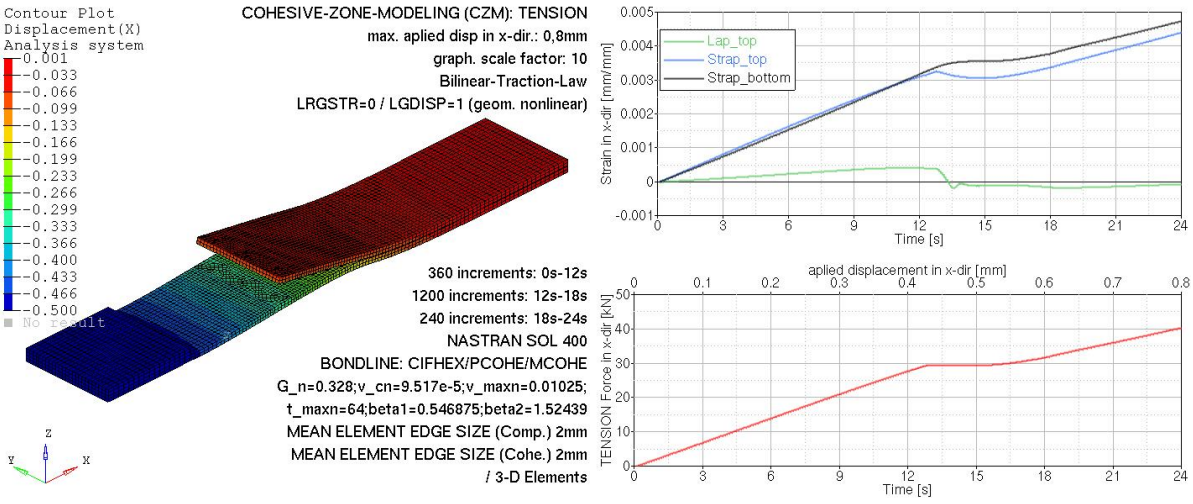


Figure 4.5: Simulation of the CLS-model using the CZM. The state of deformation is kept at an applied tensional displacement of 0,5mm

The observed bending deformation of the CLS can be explained by the theory of the bending line of the model. At the position of the trigger, the lap stiffens the strap on the upper surface. The neutral axis changes at this position from the center line of the strap to the surface between the strap and the lap, i. e. the centerline of the adhesive joint. Reducing the load ahead of the joint to a resultant force $P$ at the center line of the strap, the change of the neutral axis leads to an arising bending Moment $M_y$ at the position of the bondline start (s. figure 4.6).

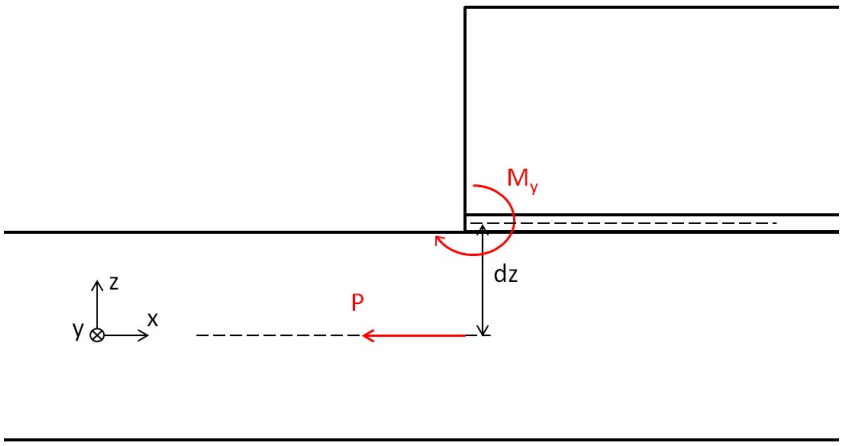


Figure 4.6: Explanation of the bending effect of the CLS through induced bending moment $M_y$ and change of neutral axis

The simulation of the nonlinear analysis can be displayed in form of a video in Hyperview, putting all nonlinear results for each load step behind each other. This makes it comfortable for the user to register modeling effects, by parameter changings. Instead of a sudden crack, the delamination progresses comparably slowly in the simulation of the FEM-model.

The damage initiation and the damage propagation is presented in tabular form in the appendix 14. The shear and normal tensions are printed over the increments of the simulation, for one specific CZE in the trigger tip.

To understand the significance of CZE-size changings, the following subchapter is imposed.

### 4.4.3. Variation of FEM-meshes on CLS-CZM-model

There are six differently meshed CLS-CZM-models created within this work, as it is shown in figure 4.7.

Not only the element size of the composite plates and the adhesive layer, but also the element type for the composite modeling are being varied to study their influence on the computing time. While model one to four create the composites out of solid elements, model five and six use a shell formulation for this purpose.

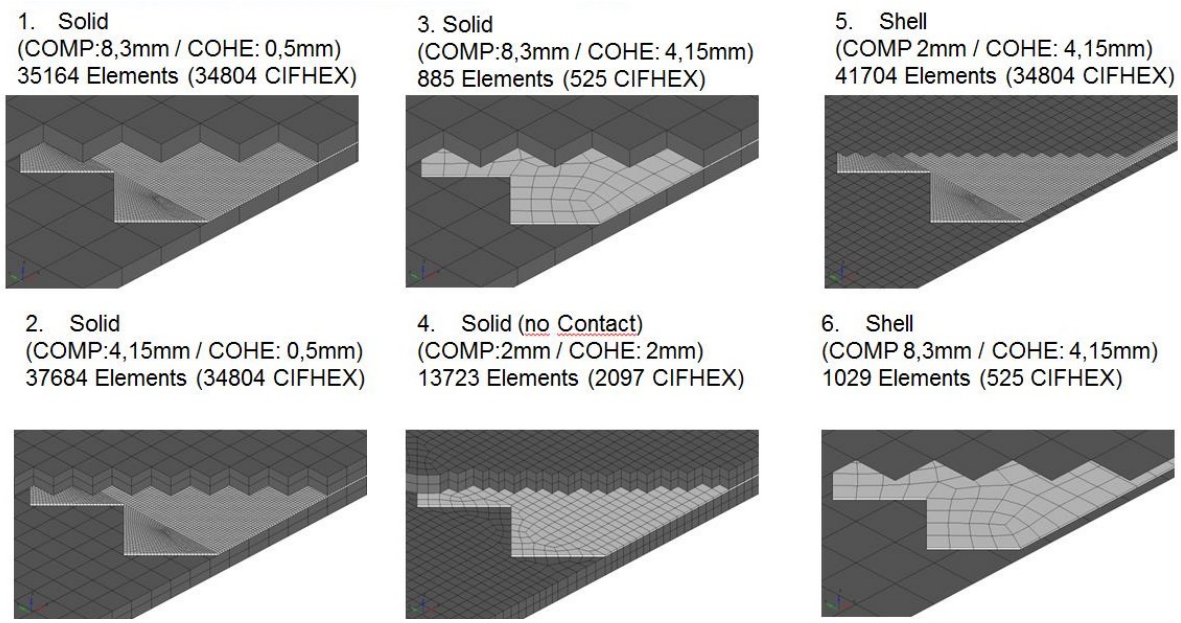


Figure 4.7: CZM-models with element size and element type variation

The study of the element size is realized in account of the requested minimal CZE-size agreeable to equation (11). Correspondingly the minimal required CZE-edge-length follows for pure mode loading to the specified values in table 3.

Table 3: Minimal required CZE-edge-length for pure tensile-loading (left) and for pure shear-loading (right) along equation 11

| $l_{CZE,Model,min}$ | $l_{CZE,ModelI,min}$ |
|---|---|
| 0,1mm | 0,55mm |

The average CZE-edge-length, the average composite element-edge-length and the amount of elements in each created CLS-model are specified on top of each image in figure 4.7. Model number four represents the basic model of the CLS as described on the previous. It is the only model consisting out of congruent meshes of the adhesive and the composite plates.
All the other models are created by the use of the contact algorithm of MSC Nastran in order to combine a coarser composite mesh with a more detailed CZE-mesh. The reason behind it is that the implementation of a coarse composite mesh and an as coarse as possible CZE-mesh reduces the amount of degrees of freedoms in the model. Thus, it

also reduces the computing time of the nonlinear analysis and thus, larger structures can be analyzed.
Since the CZE-mesh typically requires a very fine mesh in compliance with [25] and table 3, a rating of the model sensitivity related to the contact algorithm and the element sizes shall be given in this section.

In the used contact algorithm the nodes of the touching body are fixed to the surface of the touched body and it is insured to have no relative tangential or normal displacement underneath the nodes of the contact along with [1]. The chosen contact method is the conventional node-to-segment contact algorithm in MSC Nastran. According to this method, multi-point-constraints (MPCs) restrict the displacement of the contacting bodies towards each other.

The load-displacement-curves of the six presented models are compared to each other as listed in figure 4.8.
In general, all models provide quite similar failure behavior meaning that the mesh size

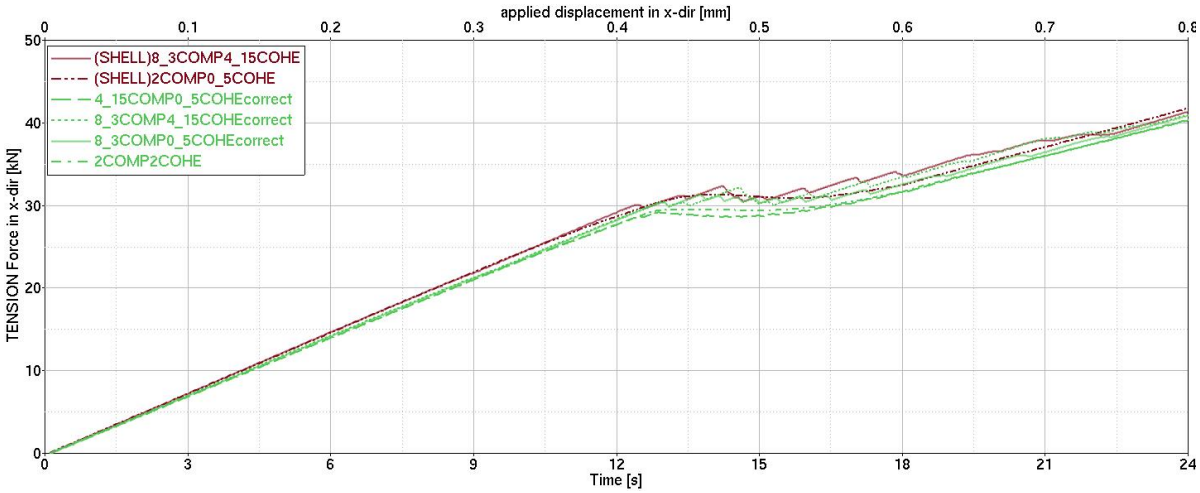


Figure 4.8: load-displacement-curves of different CZM-models

effect of the CLS-model under the given conditions is not significant.
The attached CIFHEX stress-output table 14 for the CZE 469208 in the appendix provides a possible explanation of these similar simulation results. It shows that this CZE fails mostly because of shear loading.
At the increment where the regarded CZE starts to fail ($d \geq 0{,}01$), the resultant shear

stress $\tau_{res,shear}$ determined after equation (17) is elevated to $\tau_{res,shear}$=32,8MPa. This value is close to the critical defined shear stress of the Mojo-Mix adhesive of $\tau_{max,shear}$=35MPa.

As a repetition, the theory states that a mostly on shear loaded adhesive layer is not very sensitive to the CZE-size variation, which might explain the negligible influence of the executed mesh-size variation.

The stiffness and the point of failure of the shell composite models diverges slightly from the solid composite models. The different stiffness results from the different kind of clamping conditions. In the solid models only the nodes at the top and bottom face of the lap and strap are constrained what properly reflects the reality of the tests. In contrast the constrained nodes of the shell composite models are arranged at the mid-plane of the lap and the strap. A graphical augmented visualization of this phenomenon is attached in the appendix C.8 by using a high graphical scale factor for the fully delaminated CLS-model.
The strain curves of all the six regarded CLS-CZM-models are also provided in the appendix C.7.

While the results of the six cohesive zone models appear to be similar to each other, there are significant differences in the computational efforts of these models. The duration of analysis for each model is listed in the table 4.

Table 4: Simulation time of CZM-models

| **model identification** | **average composite element edge size [mm]** | **average CZE edge size [mm]** | **stiffness update time [s]** | **iteration time [s]** | **wall time (1800 increments)** | **critical force [kN]** |
|---|---|---|---|---|---|---|
| 1. Solid | 8,33 | 0,5 | 3 | 4,5 | 13h33min | 30 |
| 2. Solid | 4,15 | 0,5 | 10 | 5,5 | 16h | 29 |
| 3. Solid | 8,33 | 4,15 | 0,3 | 1,5 | 1h15min | 30 |
| 4. Solid | 2 | 2 | 1 | 9 | 19h18min | 29 |
| 5. Shell | 2 | 0,5 | 3,5 | 3,5 | 15h26min | 30 |
| 6. Shell | 8,33 | 4,15 | 0,6 | 0,2 | 18min | 30 |

All six simulations fulfill the same amount of 1800 load increments during their implicit

nonlinear analysis. Anyhow the wall times of the nonlinear analysis do vary in a range from 18 minutes to 19 hours and 18minutes.
As assumed, the amount of elements is the most important factor in the duration of the analysis. Additionally, the shell composite models run faster than the solid composite models because of their fewer amount of gridpoints and thus on their fewer amount of degrees of freedom.

## 4.5. Rating of FEM results

The CLS-simulations deliver qualitatively correct results with respect to the strain gauges. If the strains of the strain gauges are compared to each other before the delamination is initiated, the FEM model shows a similar stiffness to the tested specimen at all the three regarded strain gauges on the CLS.

Furthermore, the use of the CZM and the Breaking Glue algorithm lead to results, which both simulate the delamination onset at a load level far beyond the tested CLS-specimen. The results using the Breaking Glue algorithm, which are attached in the appendix C.2, should theoretically just correlate to the point, of the first failure onset. Afterwards the softening of the adhesive is not respected so the results should slightly vary to the results of the CZM-models.
Anyhow, because the Breaking Glue algorithm should deliver good results unto the first failure onset, it might be taken in future projects to define limit loads of adhesive joints.

The critical force for the initiation of the delamination along the CZM-CLS-analysis in this thesis is $F_{crit}$ ≈30kN. This result has been reached as well in a previous investigation at Airbus Defence and Space by M. Bordogna (s. [21]). He evaluated the CLS-model using the solver Marc of the MSC Software Corporation.

D. C. Noorman (s. [42]) also used the solver Marc of MSC Software Corporation. Creating his CZM-CLS-model, with an average element-edge-length of 2,5mm his model utilized the exponential traction material law. His model led to a failure at a critical load of 28,65kN, which is close to the simulated result of this work.
Using the commercial FEM-tool Stress Check, M. Weiland (s. [22]) who previously investigated the CLS-model at Airbus Defence and Space, built up a CLS-model without using any cohesive elements. Instead, he utilized interaction criteria to predict failure.

His „Puck“-delamination criterion predicted an initiation of delamination at a load of 34kN.

In the end, there is no answer to the question why the critical load of 55kN of the test at the university in Augsburg could not be simulated so far. For further investigations it might be helpful to enlarge the number of tested specimen. This might help by finally extracting a mean value out of several test results, because tests of adhesive joints often tend to vary significantly at their point of failure.

Possible reasons and studies, why the simulation did not reproduce the test situation are summarized for a better overview in table 5.

Table 5: Reasons and studies for the explanation of the deviation of the simulations

| **Reason** | **Comment** |
|---|---|
| mesh size effects | have been studied in a mesh-size study of the CZE- and the composite-mesh in subsection 4.4.3 |
| achievement of convergence | has been studied in subsection C.3 |
| test inaccuracy | only one test-sample has been loaded; further tests could help to define a mean value |
| deviation of the exact assembly in the tested specimen | the bracket at the clamping doubler did have a vertical initial displacement in the test ( has already been studied of M. Bordogna (s. [21])); further deviations could have been present at the tested sample (for instance inaccuracies at the sharp trigger edges of the adhesive or thickness of adhesive) |
| problems with the determination of the critical energy release rates $G_{CI}$, $G_{CII}$ | according to the executed parameter study in subsection C.1 the failure load can be simulated by changing the CZE-MCOHE-input |
| test conditions did not match to the simulations | the adhesive properties of the „Mojo-Mix“ are influenced by the present temperatures and the speed of displacement application according to [34] |

# 5. Investigation on critical details

Within this section, the critical details are being studied. These components are located one level higher than the CLS specimen in the validation pyramid (s. 1.2). This level geometrically supposes an intermediate step between the element level investigation of the CLS and the dimensioning of the final full scale component. Overall, the critical details form composite T-stringers which are secondarily bonded on top of composite skin panels.

There are three types of critical details to be investigated: the T-Pull-, the T-Tension- and the T-Shear-model. These three tests form the main loading conditions of stiffened skin panels in the aeronautical sector. The specified tests have been restarted at Airbus in line with the development of the A400M cargo door.

The previous investigation by M. Weiland (s. [22]) on the critical details could already accurately model the stiffness of the components. In the same time his studies identify delamination to be one of the major failure types occuring in the critical detail models. In this respect, this work exclusively focuses on the simulation of the predicted delamination failure by the CZM.

## 5.1. T-Pull

First, the T-Pull-model is presented, starting with the explanation of its assembly and its integrated materials. Afterward, the test results are revealed and the simulation of the T-Pull-model follows. In the end, the results of the simulation are evaluated by a comparison with the test results.

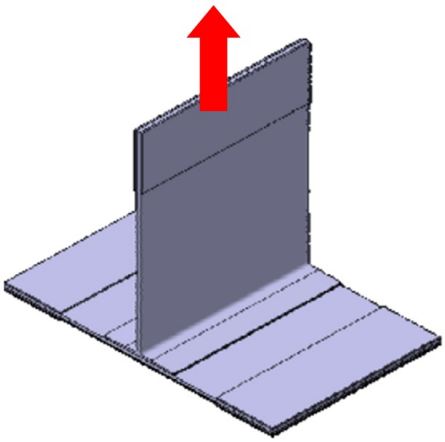

The T-stringer is fabricated out of two composite L-profiles which are at their long arms mirror invertedly placed to each other and adhesively connected. A composite capping strip is adhesively bonded to the bottom face of the short arms of the L-profiles. Due to the radial curvature of the L-profiles, an airy hole would arise in the center of the named three parts which is filled by a gusset. The gusset itself consists out of a composite layup of +/-45°-UD-layers of CFC. The hereby generated T-stringer is finally adhesively bonded on top of a skin panel also called the base plate. The dimensions and the stacking of the composites is attached in the appendix D.1.

Both sides of the base plate are horizontally clamped by fixed steel brackets. The top of the vertical T-stringer is clamped between a vertically movable bracket. To apply a load on the model, this vertical bracket moves upwards and induces thus a tensional force on the T-stringer.

The used composite material in all the skin panels of the T-stringer and for the gusset is again the “IM7 8552”. All the brackets fixing the component are made out of structural steel.

For the adhesive material, the Loctite Hysol EA9695 is used having been presented in the chapter 3. It is a low-flow bonding film of the company Henkel especially used in

aeronautical applications for the curing and the co-curing of composite laminates.
The three critical detail models to be studied use all the same composite and adhesive materials as the T-Pull-specimen. Thus it suffices to name their materials at this place.

### 5.1.1. Test results

The tests of the critical details are executed at the "Wehrwissenschaftliche Institut für Werk- und Betriebsstoffe" (WIWeB) in Erding in cooperation with Airbus Defence & Space. Figure 5.1 demonstrates the occurring conditions of the T-Pull-test in an unloaded state.

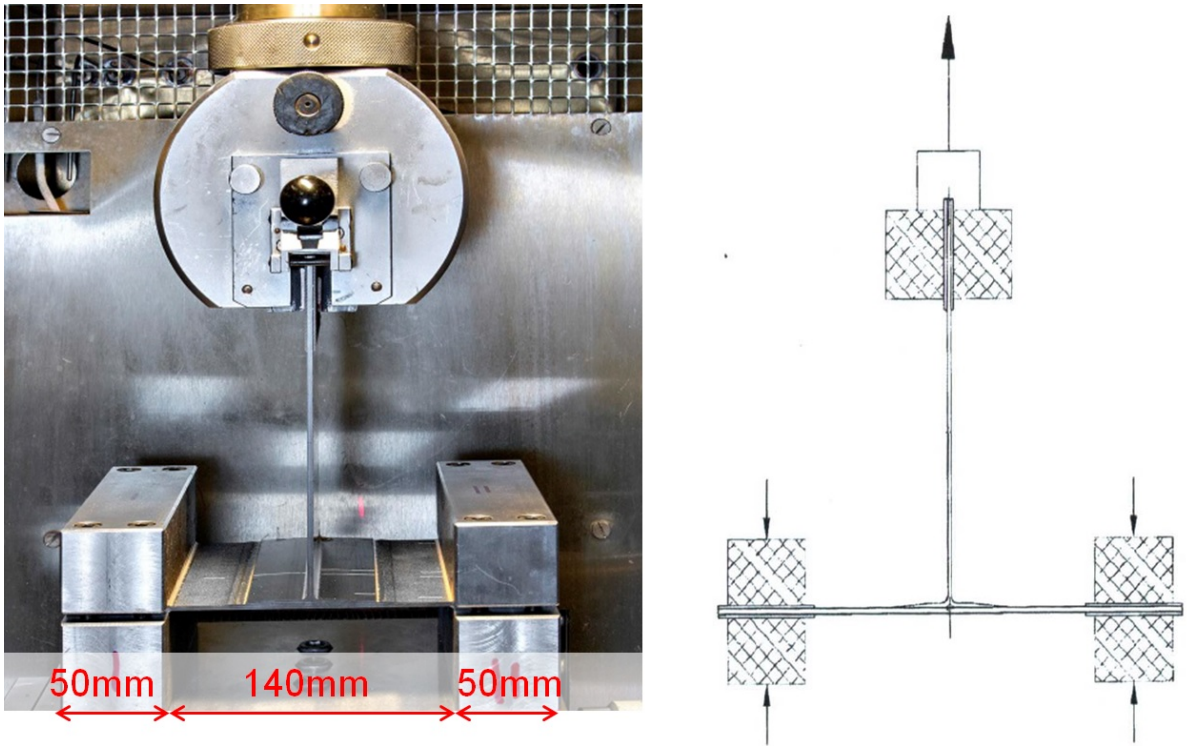


Figure 5.1: T-Pull-specimen tested at WIWeB (left), schematic representation of the loading conditions (right)

While the load is applied to the component, videos of the T-Pull-specimen are taken.
The evolution of the failures can not properly be shown in photographic sequences of the video, because the failures occurred very abruptly. This is why the kind of test failures are illustrated by photographic images of the specimen directly after the failure appeared (s. figure 5.2). Having completed 16 preliminary attempts of the T-Pull-test, the examination of the photographic images shows three major failure types.

1. Debonding between capping strip and base panel

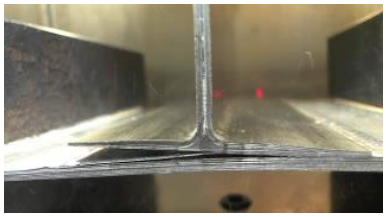

2. Gusset failure

3. Delamination between capping strip and rib foot

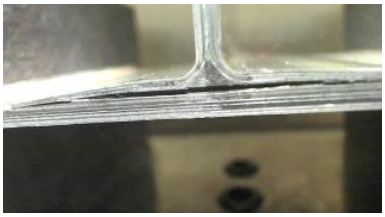

Figure 5.2: Three occurring failure types of preliminary testing of the T-Pull-specimen

Out of 14 analyzable pictures, the first failure type (s. figure 5.2 (left)) occurred eight times forming a percentage of 57%. For this type the initiation of the failure starts on one rib foot edge, while the adhesive on the opposite rib foot edge does not fail. The crack propagates up to the other side until the whole T-Stringer is delaminated.
The image in the middle depicts a failure arising around the gusset where the vertical and the horizontal arms of the T-stringer join together in the radial transition area. The gusset delaminates at the bottom face of the gusset and additionally on one side face. Four tests and thus 29% failed similar to this imaged failure type.
The remaining two tests (14%) failed in a third manner. As it can be seen at the right image in figure 5.2, the rib foot fails simultaneously over the whole adhesive layer on the upper side of the capping strip.
All the 16 tested T-Pull specimen failed in a range where the equivalent applied tensional force was in between 7,2kN and 8,1kN. The average critical failure load of the tests results to 7,7kN. The created load-displacement curves of the tests are presented within the rating of the T-Pull-simulation in subchapter 5.1.3.

### 5.1.2. Simulation

This section presents the FEM-model of the T-Pull specimen and all considered simulation aspects. First, the model is specified and elementary model adjustments are explained. Afterwards, the results of the simulation are presented. These are sub-classified into a general load-displacement analysis, a following damage and a final stress analysis.

#### 5.1.2.1. Model specification

Figure 5.3 illustrates the FEM-T-Pull model, naming its most important components.

The model creation is based on the engineering drawing of the T-Pull-specimen (s. appendix D.1).

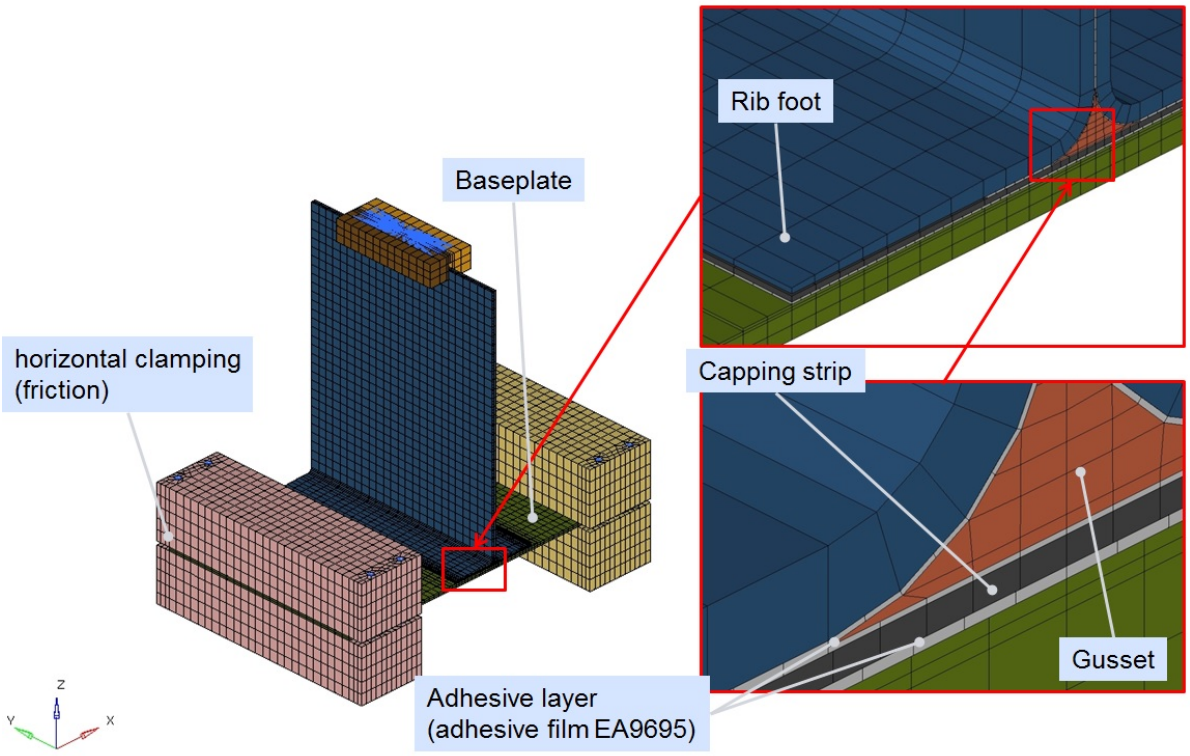


Figure 5.3: T-Pull model created via Hypermesh

The basic coordinate system of the model is also plotted and shall subsequently be used to reference areas of the model. The x-axis defines the width-, the y-axis the length- and the z-axis defines the height-direction of the component.
The composition of the adhesive layers shall be clarified by depicting detailed view displays of the model. The elements of the adhesive layers are colored in light gray and have again the CIFHEX-CZE-type as they have been implemented in the CLS- and the SLS-specimen.
There is one adhesive layer modeled between the capping strip and the base plate, one modeled between the capping strip and the rib foot and another one modeled between both L-profiles of the T-stringer. In the hole at the area of the radius of the L-profiles, the red colored elements of the gusset have been implemented between the adhesive layers of CZE. At the areas where the gusset ends, respectively two adhesive layers join together. Instead of continuing these two layers of CZEs on top of each other, they are replaced by one thicker layer of CZEs. The progressive use of two layers of CZEs would lead to

problems in relation with the critical opening distances of the elements, if no property assignment of the elements was fulfilled. With no assignment of the CZE-properties, a doubled layer of CZEs would allow a twice as high critical opening displacement $\nu_c$ as the use of one CZE-layer.
Instead, the thicker CZE-layer which result at the position at the edge of the gusset should just have a different elastic element stiffness due to its thickness according to equation (12). Unfortunately, the modeling of the thus required two different MCOHE-cards is not yet possible to model by MSC Nastran V2014 R1 in combination with the contact algorithm. In this reason the present work just uses one MCOHE-card for all CZEs in the model, knowing that according to literature (s. [25]) the stiffness of the CZEs has no significant influence on the quantity of failure load in a model.
Additionally the use of a double CZE-layer is not recommended, because if two CZEs laying on top of each other would both completely damage ($d$=1,0), the CZE-nodes at the interface of these two CZEs would not be constrained anymore in the model, leading finally to the break-off of the analysis.

The present CZEs have a mean element edge length $l_{CZE}$ of 1-2mm and the composites have an element edge length $l_{E,Composite}$ of 2-6mm. The element sizes remain equal for all the three studied critical details.

Table 6: minimal required CZE-edge-length for pure tensile-loading (left) and for pure shear-loading (right) along equation 11

| $l_{CZE,ModelI,min}$ | $l_{CZE,ModelII,min}$ |
|---|---|
| 0,6mm | 0,47mm |

Pursuant to [25], the chosen element-size of the CZEs is again too big. The element size for the composite elements and for the CZEs is in this way orientated at the combination of the coarsest CLS-mesh, because the coarse mesh of the CLS delivered similar appropriate results to the finest CLS-mesh.
A finer mesh of the FEM-T-Pull-model would in contrast enlarge the size of the model too much so that too high computing costs would be needed.

Thus, the created mesh leads to a total number of 61727 elements and 74387 nodes of which 24675 elements are CZEs. The connection between the smaller CZEs and the coarser composite elements is again created by the contact algorithm of MSC Nastran

in the same way as at the mesh refinements of the CLS-model.

Particular effort has been expended to the T-Pull-model to simulate the frictional effects at the horizontal clamping (pink and yellow colored). The affected surfaces are not connected to the green colored base plate by congruent meshes. Instead, contact modeling is applied on the touching surfaces. The frictional effects are in form of Coulomb's friction. Common friction parameters for CFC and steel are used. The compression of the horizontal brackets is simulated by compressive loaded ROD-elements demonstrated in figure 5.4. An initial force affects the ROD-elements and hence arranges for the pressure on the surfaces of the base plate.

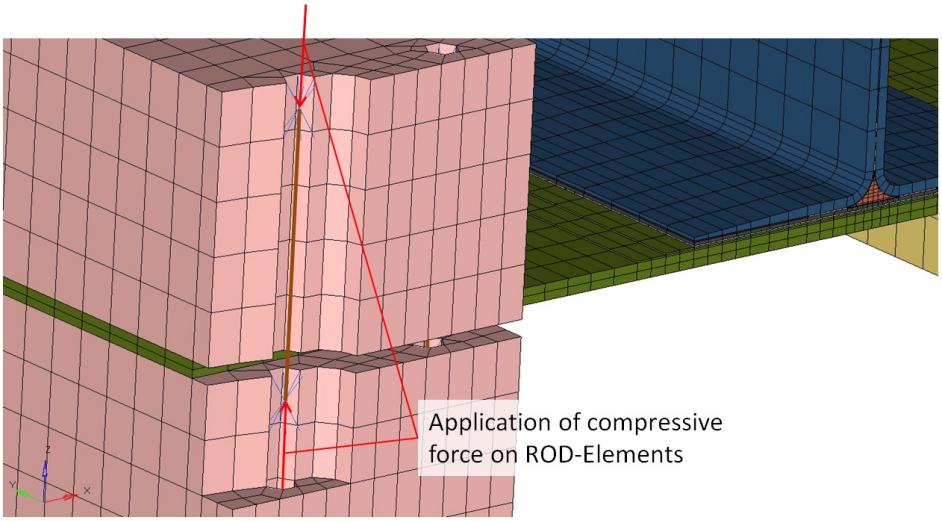


Figure 5.4: Compression of the horizontal clamping with ROD-elements (brown); elements of the horizontal bracket have been masked to point out the ROD-elements

The brown colored ROD-elements symbolize the screws of the real component loaded by compressive forces to press the brackets towards each other. In this favor, the blue colored rigid body elements connect the nodes of the ROD-elements to the surrounding mesh of the brackets. Each of both horizontal brackets is held together by four of these ROD-elements.

Different friction parameters are simulated to correctly consider the effects of the horizontal clamping and to get an impression of how sensitive the model becomes towards the horizontal clamping conditions.

All nonlinear settings of the simulation remain untouched to the previously chosen settings of the CLS-model.

#### 5.1.2.2. Load-displacement behavior and adhesive bondline failure

In this section, the general behavior of the FEM-simulation is introduced. While the T-Stringer moves upwards for each load increment leaded by the vertical bracket, both sides of the base plate are kept down at their initial position by the horizontal clamping. It leads to an upwards bending of the base plate at the center of the component until the component can not bear the deformation any further. At that moment, the adhesive layer starts to fail and leads to the simulated failure mode depicted in figure 5.5. It

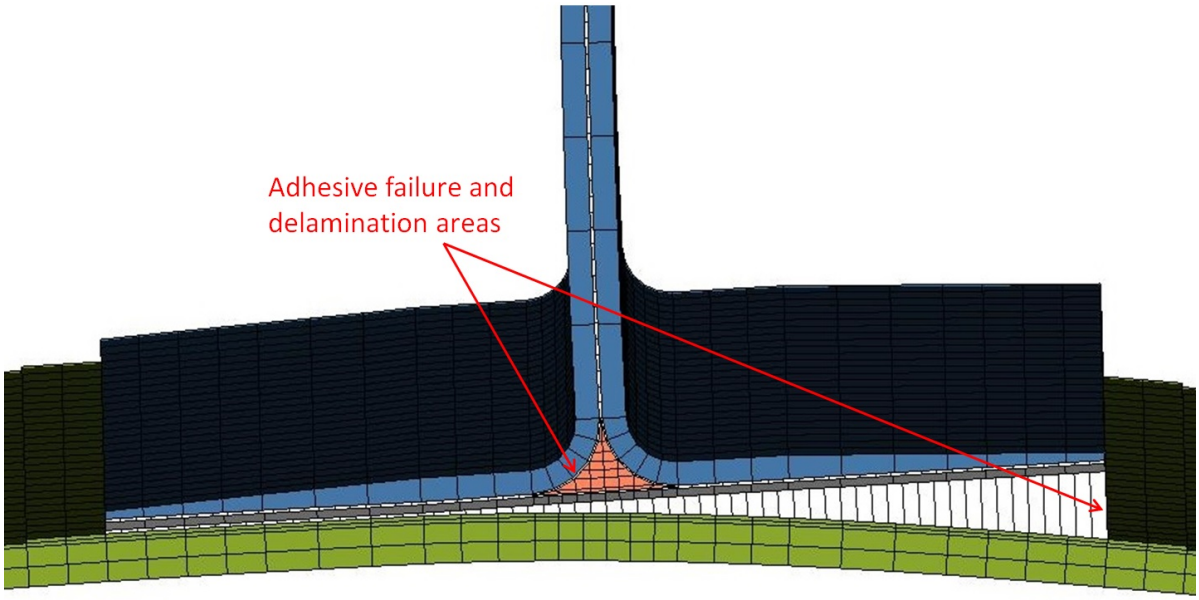


Figure 5.5: Load step of the simulation showing the areas of delamination at the T-Pull-model (graph. scale factor GSF = 5)

shows a delamination between the capping strip and the base plate starting at the right edge (positive x-direction) of the rib foot. In a few amount of load increments of the nonlinear analysis, the crack shifts along the surface of the base plate and finally leads to the complete delamination of the capping strip and the base plate.
Additionally, some CZEs delaminate on the upper side of the gusset opposite to the side where the delamination underneath the capping strip initiated. Both regions where

a delamination occurs are marked in the figure. The complete failure progress of the FEM-model will be explained in detail at the resultant load-displacement-curve of the simulation.

With the load-displacement-curve (s. figure 5.6) in mind, it shows an approximately

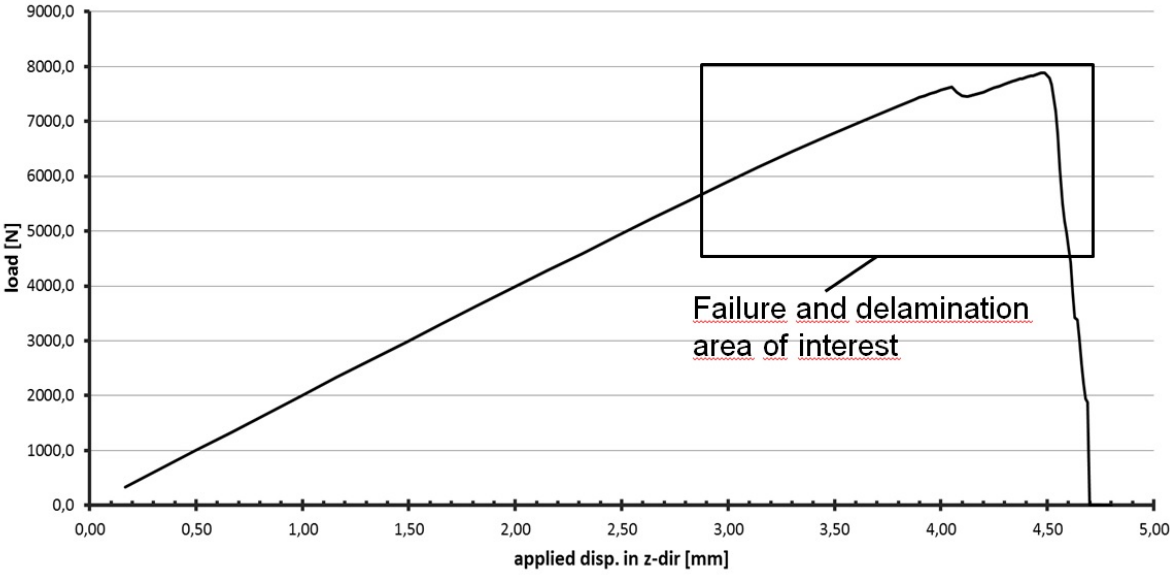


Figure 5.6: Load-displacement curve of the standard T-Pull model using the CZM

linear behavior of the component up to the load level around 7,7kN. This load is reached at the point where a vertical displacement of 4,0mm is applied on the top arm of the T-stringer. Since the gradient of the load-displacement-curve describes the stiffness of the examined component, there is no distinct stiffness change up to this point. Increasing the applied displacements in vertical direction further, the carried load decreases abruptly underneath 7,5kN before it continues to increase again. This discontinuity is a first sign of significant stiffness change of the model and will thus be regarded in detail.
When the applied displacements rise to 4,5mm, the load-displacement-curve shows the next decrease. The highest load sustained by the component of $F_{sim,crit}$ =7,85kN is reached at this point. This load is called the critical load of the component. After reaching this point, the sustained load decreases in a short period to 0kN meaning that the total failure has been arisen.

The area of the discontinuities is framed on the load-displacement curve. It will subsequently be the regarded area for the damage and the stress analysis of the adhesive bondlines.

#### 5.1.2.3. Damage analysis of the adhesive bondlines

Within the damage analysis of the adhesive bondlines, all of the modeled CZEs obtaining any damage larger than 1% shall be traced. A CZE starts to damage, once its failure onset criterion corresponding to 2.9 is reached. If a CZE possesses the damage value d=1,0, its stiffness is decreased to zero and thus, the adjacent components delaminate. In figure 5.7 the framed area of the load-displacement-curve is presented in detail.

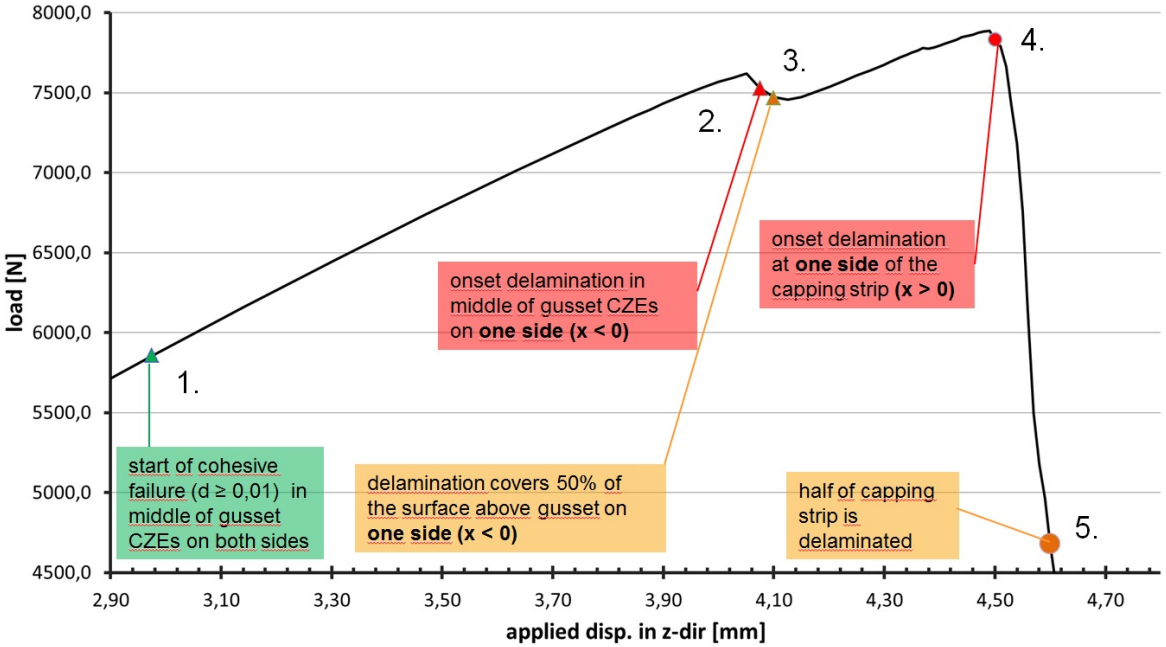


Figure 5.7: Area of interest of the load-displacement-curve where the failure of the adhesive bondlines occur in the FEM-T-Pull-model

Five Significant points for the damage evolution are added with a marker on top of the curve. An image showing the damage value of the CZEs in the bondlines is added in figure 5.8 for each of these five load points .
Undamaged CZEs are not plotted at all, whereas damaged elements are plotted and colored along the quantity of damage they bear. Low damaged CZEs ($0{,}01 \leq d \leq 0{,}1$) are colored in dark blue, high or even completely damaged CZEs ($0{,}9 \leq d \leq 1{,}0$) are colored in dark red.

The first CZEs having a damage value $d \geq 0{,}01$ start to fail at a sustained load of 5,8kN (at point 1.). As shown in the top left picture in figure 5.8, these CZEs are located on one side of the T-stringer, in between the L-profile and the gusset. It is

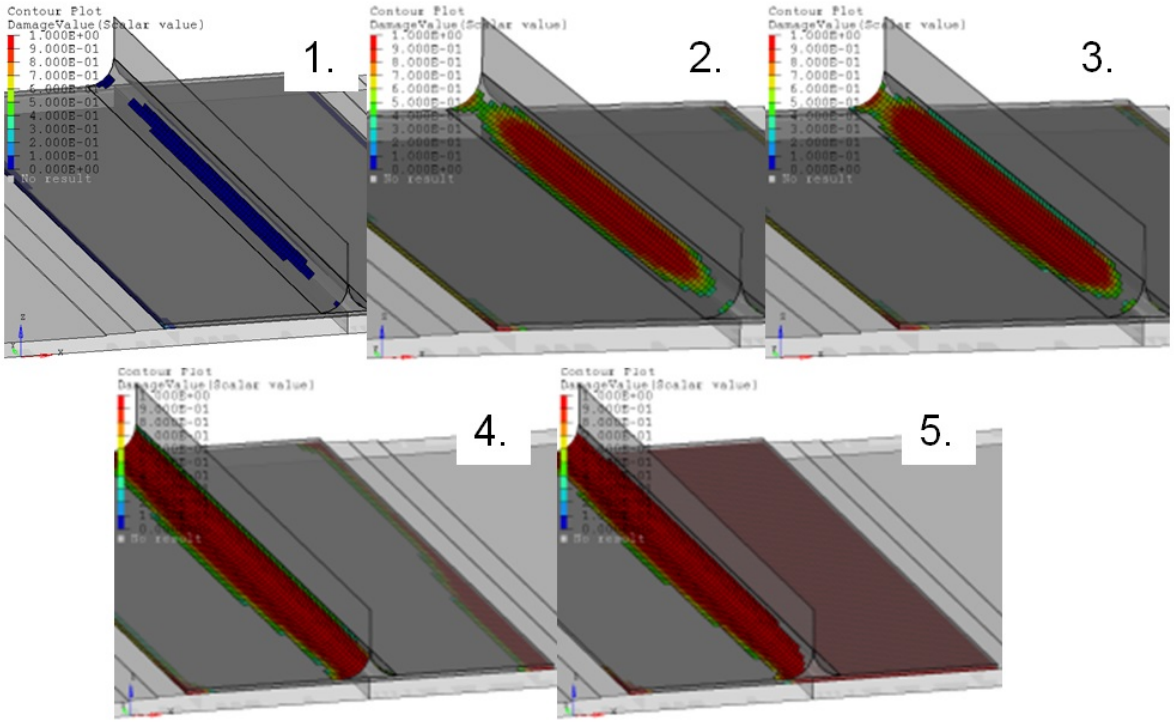


Figure 5.8: Images of CZE-damage at the points of interest according to the load-displacement curve shown at figure 5.7

remarkable that the damage starts in the middle of the component and just few CZEs fail at the front and the back side (y-direction). In the same load increment, a failure exists also in the adhesive bondline between the capping strip and the base plate. Just the complete outer row of CZEs situated on the left and the right side (x-direction) of the model simultaneously has a damage value $d \geq 0{,}01$.

In the load increment at point 2., the first CZEs are damaged completely $d$=1,0. Having passed an equivalent applied load of 7,7kN, the left (negative x-direction) L-profile of the T-stringer starts to delaminate of the gusset. It is the same side where the first CZE failure above the gusset had been discovered at point 1.. Additionally, the component starts the delamination progress in the center of the length direction (y-direction) too, just like the failure had been initiated. At the other side of the gusset (positive x-direction), none of the CZEs damages more than 50% ($d$=0,5).
A possible reason for this unsymmetrical delamination might be the rotated composite layup of 6° compared to the basic coordinate system of the component. This rotated layup is demanded along the side view of the engineering drawing in the appendix D.1.

In total, an amount of 114 CZEs damaged completely at the end of the load increment at point 2.. The number of fully damaged CZEs during the simulation of the model is plotted over the load-displacement-curve in the appendix D.2.

For the following load increments of the simulation, the delamination proceeds further along the length direction of the model until it reaches the front and the back side of the component. Before the capping strip starts to delaminate of the base plate at point 4.), the specified delamination covers nearly the whole radial area above the gusset. Until point 4. is reached, the number of fully damaged CZEs rises up to 584 elements. Afterwards, the delamination between the capping strip and the base plate starts until these two parts are fully delaminated of each other. Thus, the number of fully damaged CZEs rapidly grows to 5397 elements in the end of the simulation.

With the load-displacement-curve in mind, it is remarkable that the one-sided delamination above the gusset influences the stiffness of the component which thereby, does not loose its full bearing capacity. In contrast, the delamination of the whole capping strip has a much higher influence on the stiffness. This second delamination finally leads to the main failure of the component after which it can not sustain any loads anymore.

#### 5.1.2.4. Stress analysis of the adhesive bondlines

In order to understand the damage behavior of the adhesive layers in the T-Pull-model further, the stresses in all of the adhesive layers are reviewed. In this connection, the stresses of the adhesive layers are separately imaged. The adhesive layers around the gusset are separated the way it is shown in figure 5.9.

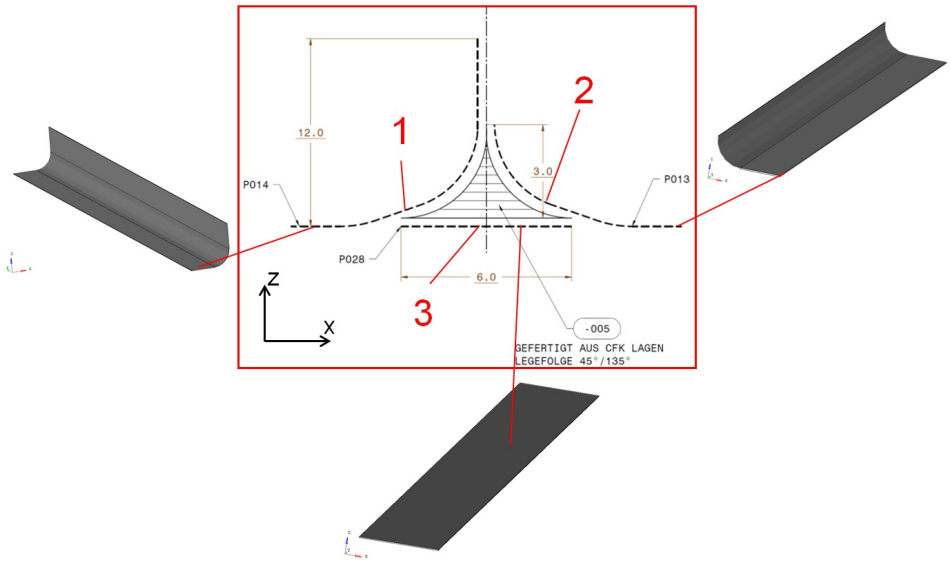


Figure 5.9: Composition of the adhesive layers around the gusset

As it has been explained in chapter 2.2.3, the relevant stresses of the CZEs are differentiated in peel and shear stresses corresponding to the different adhesive material properties in normal and in shear direction. Hence, the resultant shear stress is formed along equation (17) and used for the shear stress evaluation.

A selection of peel- and shear-stress-distribution-plots of the adhesive layers around the gusset and the adhesive layer underneath the capping strip is attached in the appendix of the T-Pull-specimen D.3 to D.10.
The stress analysis is concentrated on the points of interest specified at the load-displacement-curve in figure 5.7. Particularly, the load step of failure initiation is of interest, because on the one hand the failure onset criterion reaches the value $QIC$=1,0 and on the other hand the damage value d starts to rise.
In order to give an example of the stress plots, the stress distribution of the adhesive layer 1 (s. figure 5.9) is illustrated in figure 5.10 at an applied load of 5,8kN (point 1. s. figure 5.7).

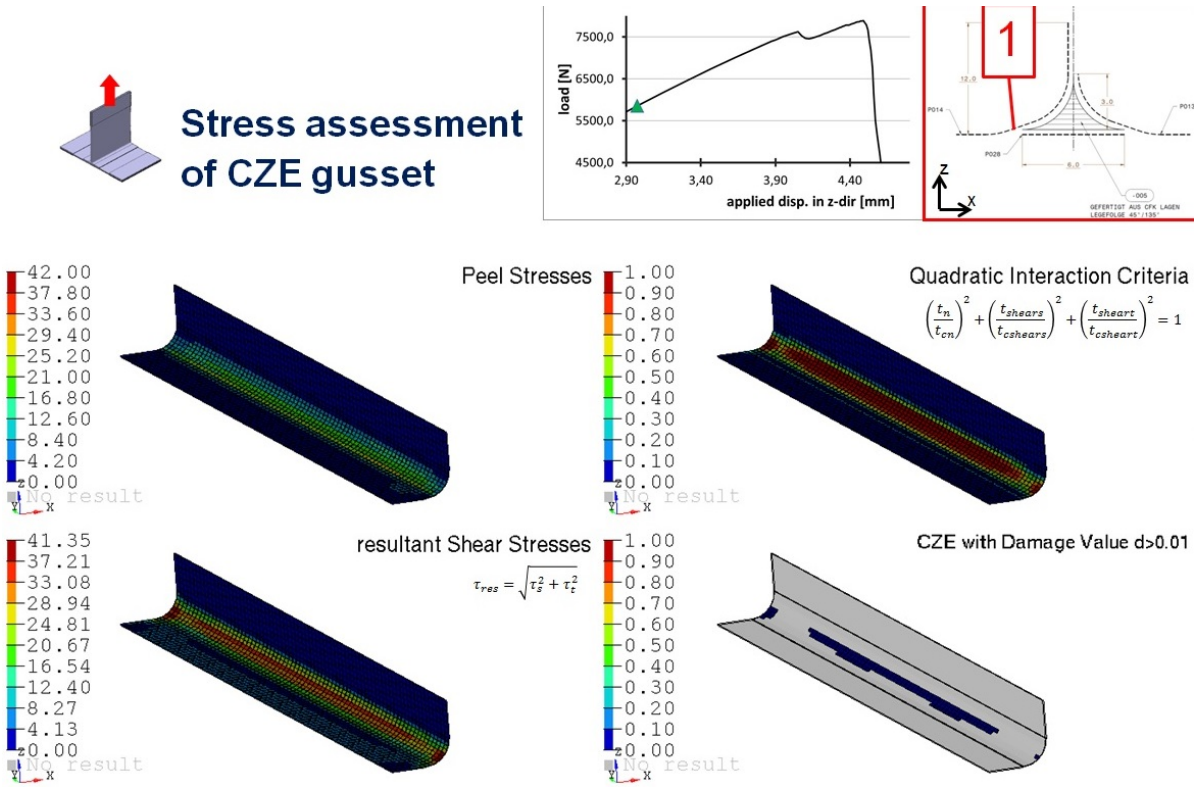


Figure 5.10: Stresses in adhesive layer 1 above the gusset at an applied displacement of $w_{applied} = 2,97mm$; equiv load=5,8kN

Adjacent to the stress distributions in the adhesive layers, the quadratic interaction criterion is calculated for all of the CZEs according to equation (14) and it is plotted at the top right image of figure 5.10.

At those elements where the combination of peel and shear stresses in form of the quadratic interaction criterion rises to the value QIC=1,0, the CZEs start to damage. For the purpose of giving a better overview of the analysis, the damage values of the CZEs are plotted once more in the bottom right corner of the figure.

Concerning the mapped adhesive failure above the gusset in figure 5.10, it is important to state that the regarded adhesive layer fails for the most part due to shear loading. The adhesive shear stresses of those CZEs starting to fail at this increment are elevated to $\tau_{shear}$ ≈35MPa. This, in turn, is close to the critical adhesive shear stress of $\tau_{max,shear}$=[redacted].
In contrast, the peel stresses elevate at these elements only at an average of 20MPa.

The stress distribution in the adhesive layer between the capping strip and the base plate is shown in figure D.8 to D.10 in the appendix. When the delamination of this adhesive layer starts at an applied displacement of 4,5mm, the stress distribution shows a ratio of peel and shear stresses. Thus, the adhesive layer underneath the capping strip primarily fails due to high shear stresses, too.

### 5.1.3. Rating of FEM results

The evaluation of the FEM-simulation is done in consideration of the test results. If the load-displacement-curve of the simulation is put on top of the load-displacement-curves of the preliminary tests, the proximity of all the curves is illustrated (s. figure 5.11).

Apart of the nonlinear loading effects in the tests at the start of the load applica-

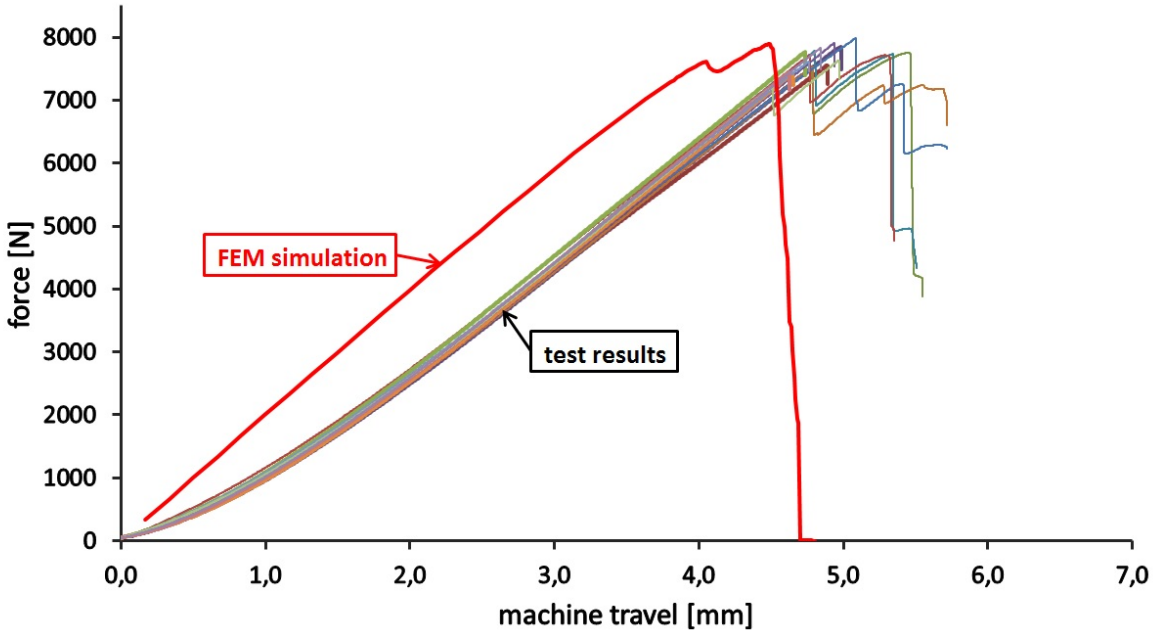


Figure 5.11: Load-displacement curves of 16 T-Pull specimen tests and of the FEM-simulation of the standard T-Pull model

tion appearing up to approximately 1,5mm of machine travel, the curves of the simulation and the tested curves conform well to each other. The curves possess the same gradient expressing that the correct stiffness could be reproduced in the FEM-model. Furthermore, the critical force of the simulated FEM-model matches into the range of

those of the tests. Nevertheless, the simulation brings up a little higher critical force ($F_{sim,crit}$=7,85kN) than the average value of the tests ($F_{test,crit}$=7,7kN).

As it has been forecited in the beginning of this chapter, M. Weiland (s. [22]) used a Puck-failure-criterion to determine the failure to be expected. Corresponding to his results, the delamination at the upper side of the gusset as it is also discovered in this chapter is the critical failure for the T-Pull-model.

Indeed, the exact mode of delamination of the herein simulated FEM-model (a combination of delamination above the gusset and underneath the capping strip) could not be identified at any test specimen. But, the delamination of the test occurred in case 1. and case 2. according to figure 5.2 at one of the simulated positions, either next to the gusset or at one side underneath the capping strip.

Obviously, the T-Pull-model reacts very sensitive in reality. Since all the tested specimen have been fabricated and tested in the same way, one kind of failure mode for all the tests would be expected.
The reason for the varying test results must be based on slight, unavoidable inaccuracies or minimal deviations in construction and setup.

While the component has been simulated several times under the influence of changing some model parameter, the sensitivity of the T-Pull-model can be demonstrated at the FEM-model. The variation of the material input for the MCOHE-cards of the adhesive as well as the variation of the clamping conditions of the horizontal brackets illustrate the named sensitivity.
Both parameter variations are attached in the appendix of the T-Pull-model (s. figure D.11 and D.12).

The change of the material input at the MCOHE-cards of the adhesive refers to the fact that no distinct material values for the adhesive Hysol EA9695 could be found along literature and tests which respect in the same time equation (20). In this reason, the values of the energy release rate have been kept fix according to [35] and a parameter study of the remaining four MCOHE-parameter: $E, G, \tau_n, \tau_{shear}$ has been fulfilled.
In the end, all of the chosen MCOHE-cards lead to a critical loading of the FEM-model

around 7-8kN which is close to the test results. However, the chosen MCOHE-cards implicate at the same time a qualitative change of the mode of failure expressed by the images referring to the curves.
The most convenient MCOHE-card with respect to the maximal traction of the CZEs is attached in the appendix 11. It is the used MCOHE-card for the presented T-Pull-model of this section.

Besides, as it has been mentioned, the mode of the simulated failure could also be influenced by varying the frictional clamping conditions at the horizontal brackets. The clamping conditions considering a proposed friction coefficient $\mu$=0,15 (s. [39]) and a proposed clamping force of 6500N according to the test definition has been used in the previous part of this work.
However, it can be stated that the clamping of the model is an important adjustment of the model which has to be accurately arranged.

All in all, the chosen settings of the simulation lead to a wall time of $t_{T-Pull}$ ≈6h. The settings of the nonlinear solution algorithm include a fixed incrementation scheme with a number of $n_{incr}$=93 increments. In addition, the recommended load-displacement convergence criterion (UPV) pursuant to [1] is used. The specified convergence tolerance for mechanical load cases of $ERR_{conv,UPV}$=0,1 is also chosen according to [1]. Further nonlinear settings of the models can be read in the appendix A.2.2.
An increase of the number of increments to $n_{incr}$=800 quantitatively reduces the critical failure load $F_{crit,sim}$ about 3%. This more converged solution is achieved due to the expense of a significant increase of wall time to $t_{T-Pull}$ ≈34h.

A parallel refinement of the CZE-mesh required according to table 6 would elevate the wall time of the model drastically analog to the CLS-mesh-size evaluation and thus, it would not provide a useful approach anymore.

In the future, there are new tests for the T-Pull-model planned. Particular effort should be put in these on the clamping conditions and on the conditions of each adhesive layer so that at its best just one failure mode results out of the tests.
Besides, a suitable visual recording system for the test failure could help to understand the precise failure of the tests further.

## 5.2. T-Tension

The second presented critical detail is the T-Tension model.
Basically, the T-Tension-model resembles strongly the T-Pull-model. The assembly of L-profiles, gusset, adhesive layers, capping strip and baseplate remains the same. Even the stacking of all the composite parts is identical.
A major difference which can already be detected by looking at the figure on the right is the length of the component. Instead of 150mm, the length of the T-Tension-sample measures only 40mm.

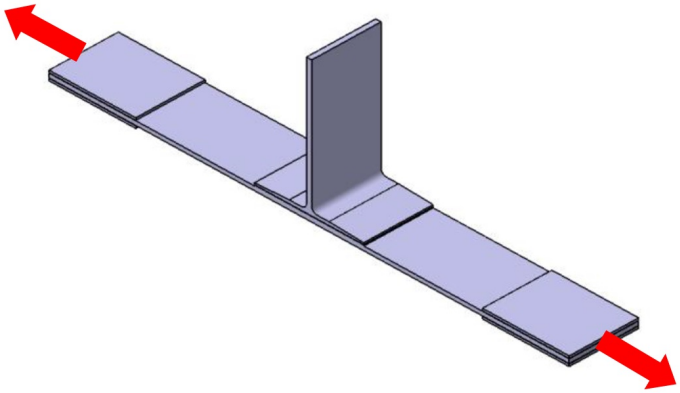

Besides, the size of the base plate clamped between the horizontal mountings is longer than the one of the T-Pull-specimen. As the T-Tension-specimen is loaded along this direction, one horizontal bracket stays fix, while the other one is movable in the width direction of the component. The red arrows symbolize the occurring loading conditions in the figure on the right.
Furthermore, the vertical clamping is not present anymore and the height of the T-stringer is reduced to 82mm.

### 5.2.1. Test results

The preliminary tests of the T-Tension-specimen are also executed at the WIWeB in Erding. Additional to the equivalent measured load, strains are measured at the surfaces of the component. In this favor, three strain gauges are installed at the surfaces agreeable to the engineering drawing D.13 in the appendix. Two of them are located on the upper surfaces of both short arms of the T-Stringer, while the third one is placed in the center of the lower surface of the base plate.
The failed T-Tension-specimen is photographically shown in figure 5.12.

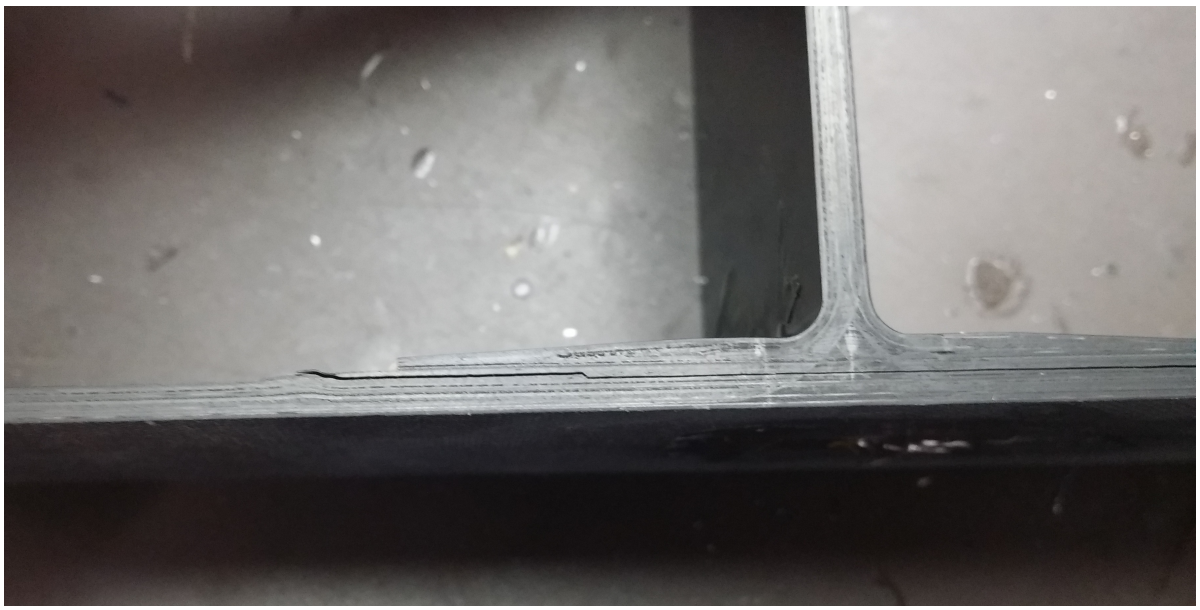

Figure 5.12: Photographic image of the failed T-Tension-test-specimen

On closer examination, the crack of the component is identified underneath the T-stringer. But, instead of arising in one of the specified bondlines, the crack begins directly at the surface of the base plate. In general, the base plate consists out of a stacking of 20 UD-layers. At its center, however, it is thickened at its upper surface by a stepped package of four additional CFC-layers in the stacking sequence of -45/+45/+45/-45°. The T-stringer is adhesively bonded on top of this thickened part of the base plate. Referring to figure 5.12, it looks like the crack arises between this stepped local thickness increase of the base plate and thus, as if the layers of the base plate delaminate without damaging any part of the bonded T-stringer.

The tested T-Tension-specimen starts to damage when an equivalent load of round about 30kN is applied. This failure is plotted on the load-strain-curves in the sub-chapter 5.2.3 in which they are compared with the result of the simulation. The simulation of the T-Tension-model is subsequently presented.

### 5.2.2. Simulation

The created FEM-model to reproduce the behavior of the T-Tension-tests is depicted in figure 5.13. Since the assembly of the component stays the same as at the T-Pull-model, the previous chapter is referenced in this way to obtain a more detailed description.

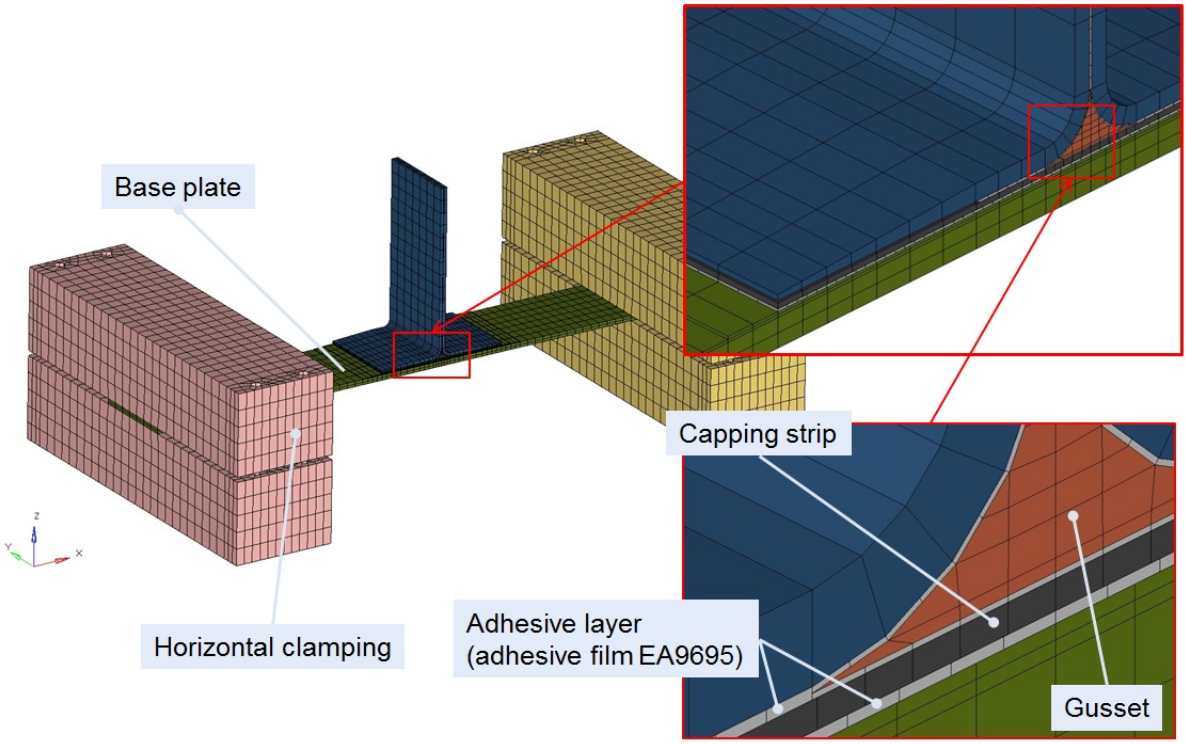


Figure 5.13: T-Tension model created via Hypermesh

The FEM-model of the T-Tension-specimen includes 14122 elements of which 4540 elements have the type of a CZE. Since the chosen element sizes used in the T-Pull-model-simulation have generated promising results, no change on the element size has been introduced at the T-Tension-model.

The movement of one of the horizontal brackets shall extend the base plate and induce a load in the component. In this reason, the frictional effects which would appear at the horizontal clamping are neglected for the sake of convenience. Thus, the FEM-meshes of the horizontal brackets and of the base plate are congruently modeled towards each other.

#### 5.2.2.1. Load-displacement behavior and adhesive bondline failure

The incrementally increased, applied displacement in x-direction (s. figure 5.13) leads to a slight downwards bending at the position of the bonded T-stringer. This state of deformation is presented using a graphical scale factor GSF=5 for an applied displacement of 1,06mm (equivalent load of 30kN) in figure 5.14.

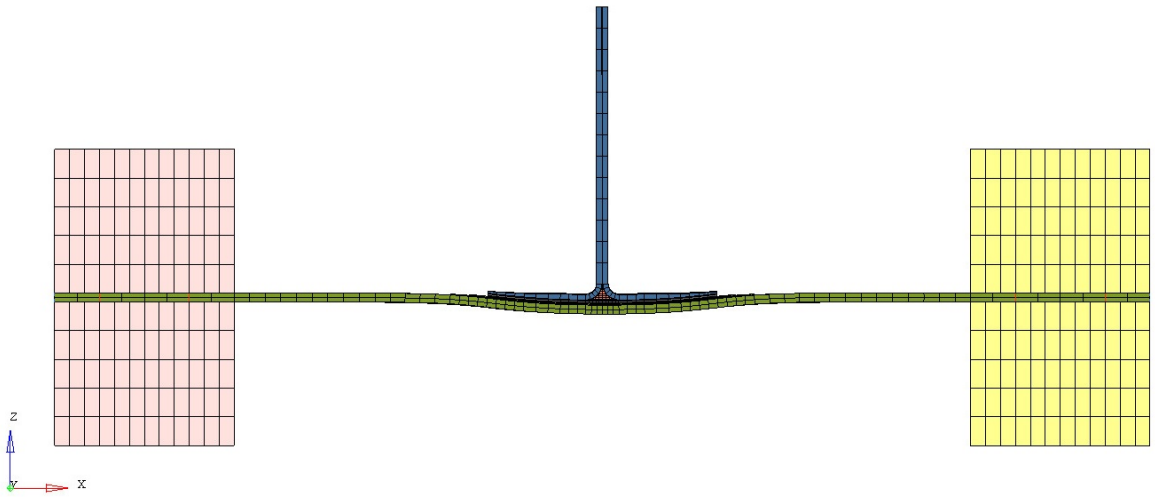


Figure 5.14: T-Tension model at an applied load of 30kN in x-direction (graph. scale factor GSF = 5)

The appearing downwards bending effect is the same effect which could be detected at the CLS model. At the position of the stepwise thickened base plate and following at the position where the T-stringer is bonded, the stiffness at the upper side of the base plate is increased. Thus, the base plate elastically lengthen more on its lower side than on its upper side resulting in the bending effect.

For the entire simulation, the sustained load of the component is plotted over the applied displacement in figure 5.15

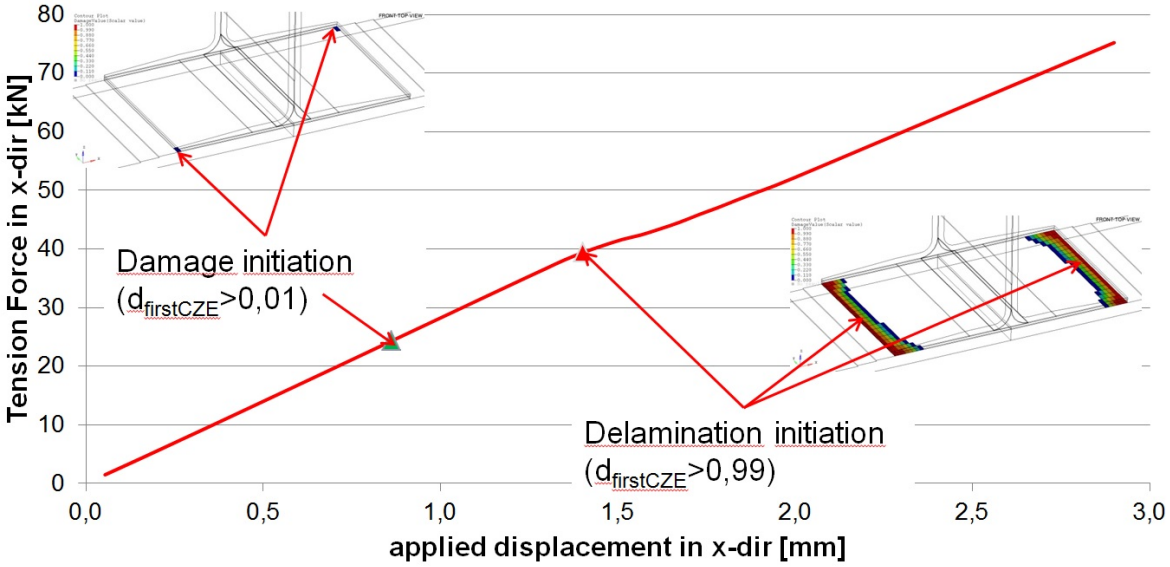


Figure 5.15: Load-displacement-curve of FEM-T-Tension-model; the points of damage initiation and of delamination initiation are marked on the curve

Within the simulation of the FEM-model, the first CZEs start to fail at an equivalent load of 24kN. At this moment indicated by the green triangle on the load-displacement-curve, the front left and the back right corner of the adhesive layer underneath the capping strip start to damage.
Just as it could be recognized at the load-displacement-curve of the T-Pull-model, the hereby initiated plastification of the corresponding CZE doesn't affect the stiffness of the component significantly. First, the start of the delamination which is indicated by the red triangle on the load-displacement-curve at almost 40kN does affect the stiffness. The gradient of the load-displacement-curves slightly decreases at this position.

The progress of the delamination during the simulation is explained in the following subchapter.

#### 5.2.2.2. Damage analysis of the adhesive bondlines

Only the adhesive layer between the capping strip and the base plate takes any damage during the simulation. No CZE damages at all in the other adhesive layers inside the T-stringer.
The explanation is based on the fact that the primary loading of the component is inside of the base plate, while the T-Stringer behaves just as a stiffness increasing part at the

upper surface of the base plate.

The delamination of the T-stringer from the base plate shown in figure 5.16 progresses relatively slow.

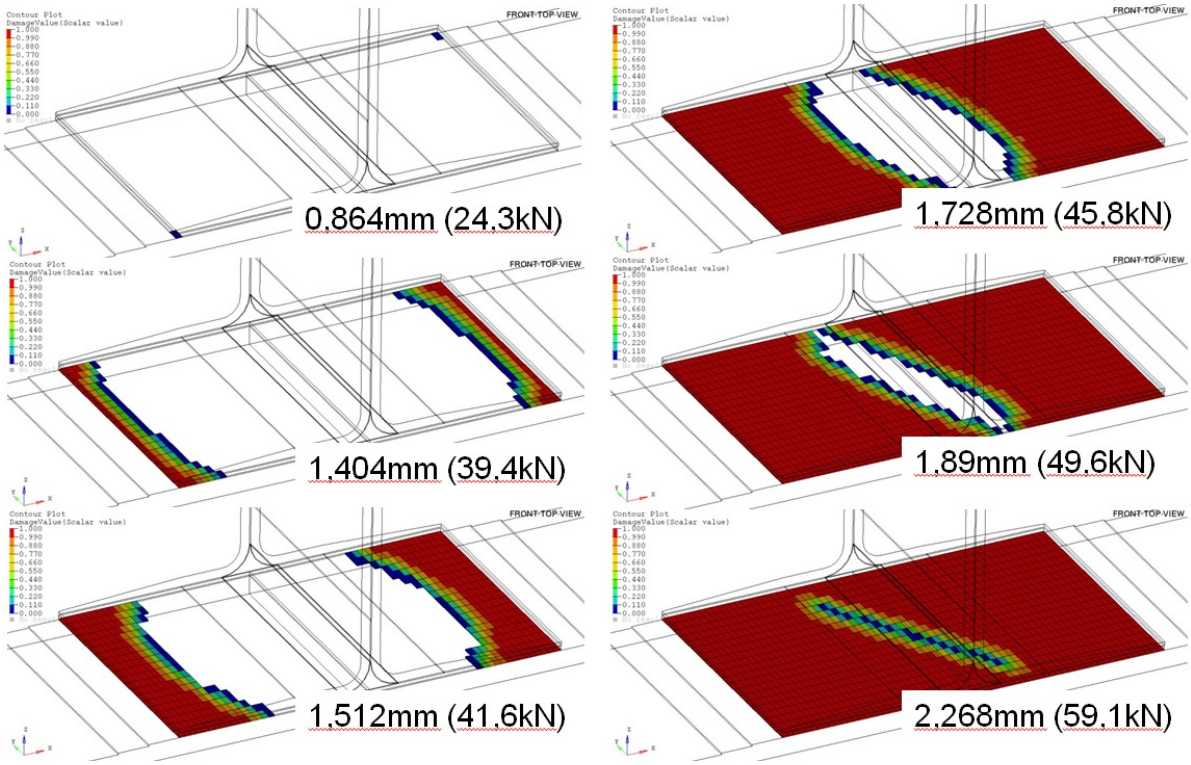


Figure 5.16: Damage evolution of the FEM-T-Tension-model (selection of load increments during the progress of delamination)

The progress of delamination is traced again by looking at the number of delaminated CZE over the simulation time (s. appendix D.14). It shows that the major part of the CZEs delaminate in between the initiation of delamination at 39,4kN and an equivalent load application of about 50kN. Approximately 1100 of the total 1280 CZEs underneath the capping strip delaminate inside this margin. Having reached the load level of 50kN in the simulation, the CZEs in the center underneath the capping strip exclusively are still intact. They delaminate in a lower rate of spread when the load is further increased. Additionally, it is conspicuous that the last failing CZEs are arranged in an angle of 45° towards the loading direction (in x-direction). This effect results out of the stacking of the base plate. The fiber orientation of the CFC-ply at the surface of the base plate underneath the adhesive layer (135°-ply) points exactly in the same direction.

In contrast to the T-Pull-simulation, the delamination of the T-stringer does not signify the break-down of the component, because the load can still be transferred through the base plate.
However, the executed simulation does not respect the destruction of the composites. On that account, it can just be stated that if the composites do endure a tensional loading up to approximately 60kN without failing, the T-stringer delaminates completely.

#### 5.2.2.3. Stress analysis of the adhesive bondlines

Since the adhesive layers inside of the T-stringer do not see a distinct load, the stress analysis exclusively focuses on the adhesive layer between the base plate and the capping strip. The occurring stresses of the CZEs are mapped in figure 5.17 for the point of failure initiation (24,3kN).

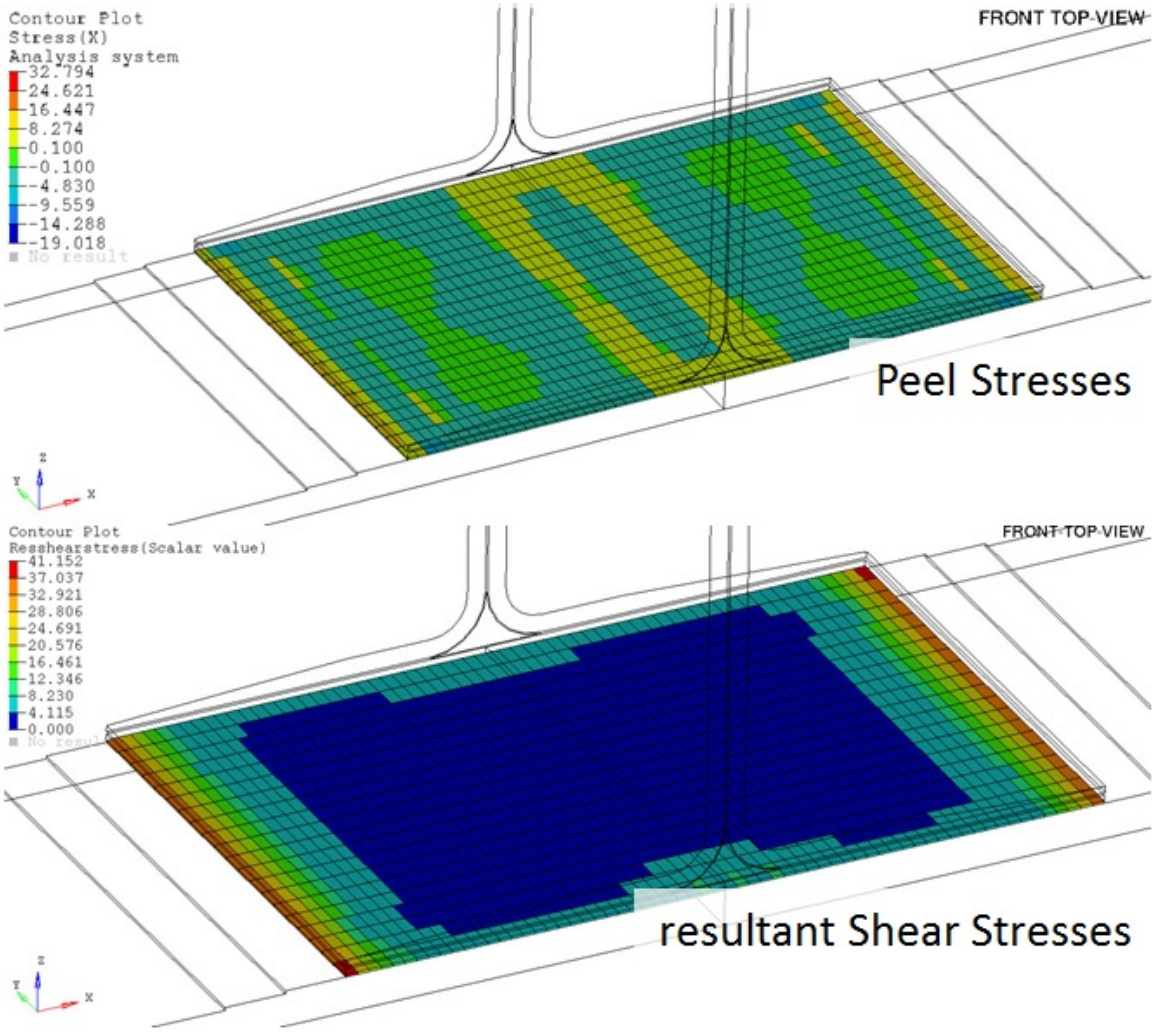


Figure 5.17: State of stress at an applied displacement of 0,864mm, which corresponds to a load of 24,3kN

The above image demonstrates the distribution of the peel stresses inside the adhesive layer, while the image below presents the distribution of the resultant shear stresses corresponding to equation (17). As the peel stresses of all the CZEs clearly are beyond the critical peel stress limit of the adhesive, the existing resultant shear stresses in the adhesive rise up to their critical limit.

At the chosen time step, the front left and the rear right CZE start failing. According to figure 5.16, their damage value rises for the first time over a damage value of $d \geq 0{,}01$. These two elements reach resultant shear stresses of up to 41,1MPa which is close to the defined shear stress limit of $t_{shear}$=[redacted] of the Hysol EA9695 adhesive.

This result leads to the statement that the adhesive failure of the T-Tension-model is nearly exclusively based on shear loading.

### 5.2.3. Rating of FEM results

The quality of the simulated results are discussed in this subsection. For that reason, the strains and the loads of the preliminary tests and those of the simulation are compared to each other. As it has been mentioned, three strain gauges have been attached to the test-specimen. The strain results of the strain gauges are presented in the following, as they are plotted over the equivalent applied load of the model. Figure 5.18 depicts the strains of the tested T-Tension-specimen at the strain gauge 1. Its position on the component is indicated on the top left image in the figure.

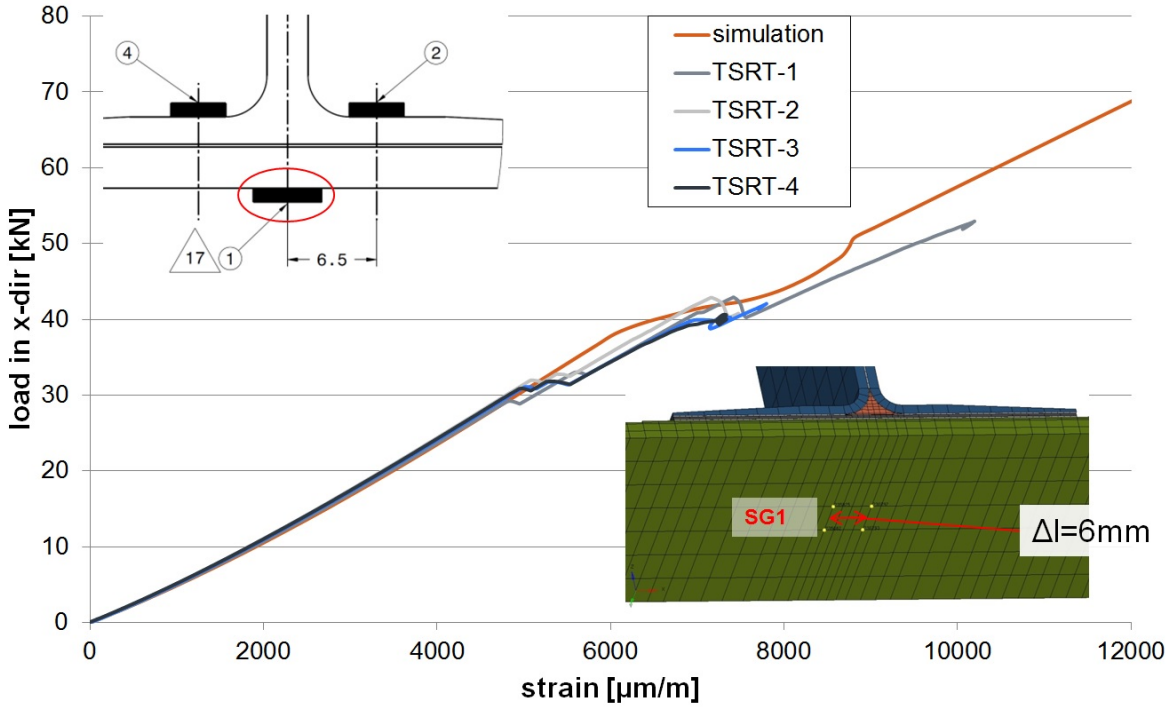


Figure 5.18: Superposition of the strain measurement at the strain gauge 1 and of the strain results of the simulated FEM-model

The four preliminary tests having been executed at the WIWeB in Erding are named TSRT-1 to TSRT-4.
Analog to the tests, the strains of the FEM-model have been evaluated at the correct position and have been superposed in the same figure. The orange curve represents in this context the strain results of the FEM-model.
In doing so, the strains $\varepsilon_{FEM}$ of the FEM-model have been calculated along equation:

$$\varepsilon_{FEM} = \frac{|u_{left,Nodes} - u_{right,Nodes}|}{d_{Straingauge}} \tag{23}$$

$d_{Straingauge}$ represents in this relation the undeformed strain gauge length. The four yellow marked nodes situated in the figure 5.18 of the FEM-model at the bottom right side represent the corners of the strain gauge position. The averaged displacement in x-direction of both left corner nodes forms $u_{left,Nodes}$ and the averaged displacement in x-direction of both right corner nodes forms $u_{right,Nodes}$.

In exactly the same way, this procedure is done for the evaluation of the other two strain gauges, strain gauge 2 and strain gauge 4 which are both located on the upper surfaces of the short T-stringer arms. The load-strain results of these are printed in figure 5.19.

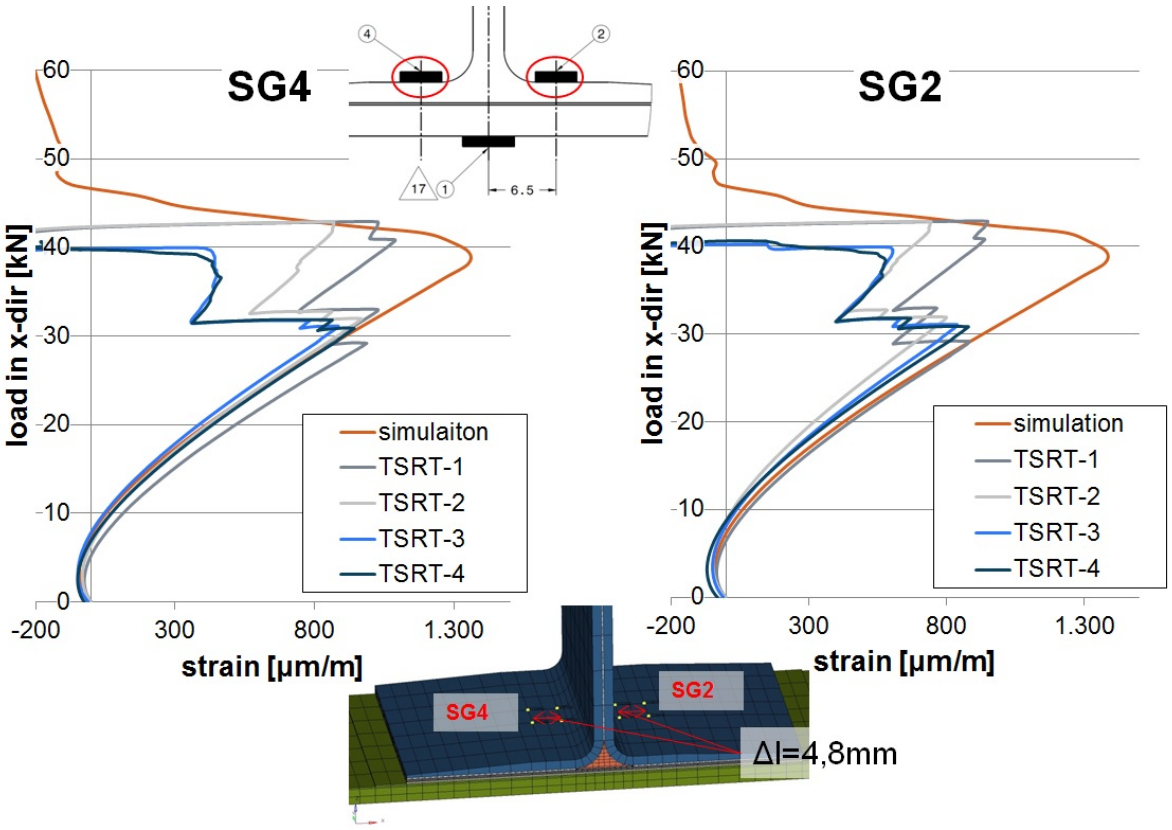


Figure 5.19: Superposition of the strain measurement at the strain gauges 2 and 4 and of the strain results of the simulated FEM-model

Basically, the deformation at all the three strain gauges of the simulation correlates to the tested models for a low loading condition up to 30kN. At a load level of 30kN, the test-curves show sudden inconstancies at all of the strain measurements. These represent a first type of failure of the tested specimen. Moreover, it does not completely destroy the specimen, because they can still sustain a further load increase afterwards. When the equivalent load is subsequently increased, the strains measured at the strain gauges approximately indicate the same gradients as before the first inconstancies have appeared. Other inconstancies are detected at the curves of the tested specimen at an equivalent load of about 40kN.

Finally, the simulation result correlates well with the test results. The predicted delamination arising underneath the capping strip did not start at the predicted load level of 39,4kN, because a different type of failure already occurred before at an equivalent load level of 30kN.

Since a crack of the tested specimen is detected at the position of the stepwise increased thickness of the base plate (s. figure 5.12), a strain output of the composites is generated to judge the occurring failure of the tests at this position.
Two figures depicting the strains at the front of the T-Tension-model at the equivalent loads of 24kN and 30kN are attached in the appendix D.16 and D.17. The first figure shows the load increment in which the simulation discovered the initiation of the softening of the adhesive layer between the capping strip and the base plate. On the contrary, the second figure depicts the state of strains where the tested specimen brought up their first inconstancies on the load-strain-curve.
The strains are visualized by ROD-elements possessing a small stiffness. They are positioned on the upper surface of the base plate and their stiffness is chosen that small that they are not affecting the stiffness of the remaining component.
With the aid of the figures, it can be determined that a local strain maximum is present inside the thickness increase of the base plate. This strain maximum rises up to 8130 $\mu$m/m at the equivalent load of 30kN. Corresponding to [38], the failure strain of a +/-45°-CFC under shear loading conditions conforms to 0,88% which is equal to 8800 $\mu$m/m. Thus, the simulated strain is at that position already close to its critical strain and consequently, a failure at this position could be expected.

In future investigations on the T-Tension-model, additional two-dimensional CZEs could be inserted in the FEM-model at the position where the failure of the test samples occurs. These CZEs could for instance be inserted between the individually modeled plys of the base plate in order to model interlaminar delaminations.
Then again it has to be discussed in the team of the project, how the model of the T-Tension is furthermore going to be progressed, because the intend of the simulation was to predict the failure of the specific adhesive in the specified adhesive layers. Since the failure did not occur in these adhesive layers, the geometry of the T-Tension-model might also be adapted until one of the secondary bonded adhesive layers becomes the critical part of the component.

At the T-Tension-model the material input for the MCOHE-card has been varied analog to the T-Pull-model. In comparison to the T-Pull-model, the T-Tension-model does not react sensitive to this change as it can be seen at the load-displacement-curves attached

in the appendix D.15.

In general, the wall time of the T-Tension-simulation amounts to $t_{T-Tension}$ ≈3h. 378 increments have been solved within the realized T-Tension-simulation. The convergence criterion and the size of the convergence tolerance remain the same as for the T-Pull-model.

Due to the fewer amount of elements and thus a fewer amount of degrees of freedoms, the T-Tension-simulation is computed faster than the T-Pull-simulation. Additionally the neglect of frictional effects at the horizontal mounting comparably speeds up the time of simulation, too.

## 5.3. T-Shear

The last of the three presented critical details is the T-Shear-model. As once again the assembly, the stacking and the lay-up does not show any difference in comparison to the other two critical detail models, there are some necessary modification of the geometry.

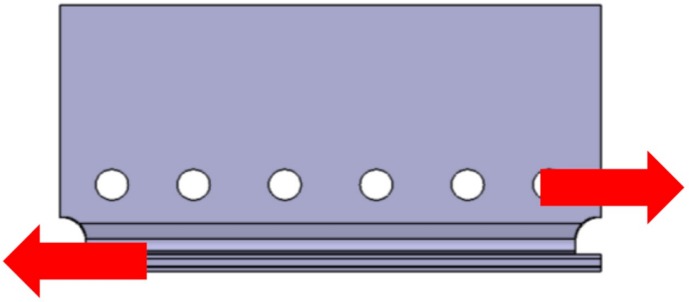

A side view of the T-Shear-model is imaged at the top of this page in order to point up the loading conditions of the model. The shear loading condition is introduced to the component by fixing both sides of the base plate on one horizontal bracket. At the same time, a displacement along the longitudinal axis of the component is applied on one end of the vertical long T-stringer arm.

For the sake of preventing the clamped composite plates to rotate in the brackets, the clamping is fulfilled by perforating the composites and using bolts to fix the composites in the brackets. A precise side and top view of the clamped T-Shear-specimen can be found in the engineering drawing in the appendix D.19.
The clamped composite parts are additionally thickened by CFC-plates in order to stabilize the component in the metal brackets of the mounting. Their dimensions are also attached in the appendix D.18.

### 5.3.1. Test results

Unfortunately, none of the T-Shear-specimen tests have been executed yet. Tests for this model are already prepared at the WIWeB in Erding and they will be executed in the beginning of the year 2016 so that they can not be referenced within this work. Nevertheless the simulation is already completed in order to predict the adhesive failure of the component. Thus, the simulation is going to be presented in the next subsection.

### 5.3.2. Simulation

Pursuant to the engineering drawings, a three-dimensional model of the T-Shear-component is created. The figure 5.20 displays the clamped FEM-model. The adhesive layers are hidden by the vertical clamping, but they have the same position as in the other two critical detail models.

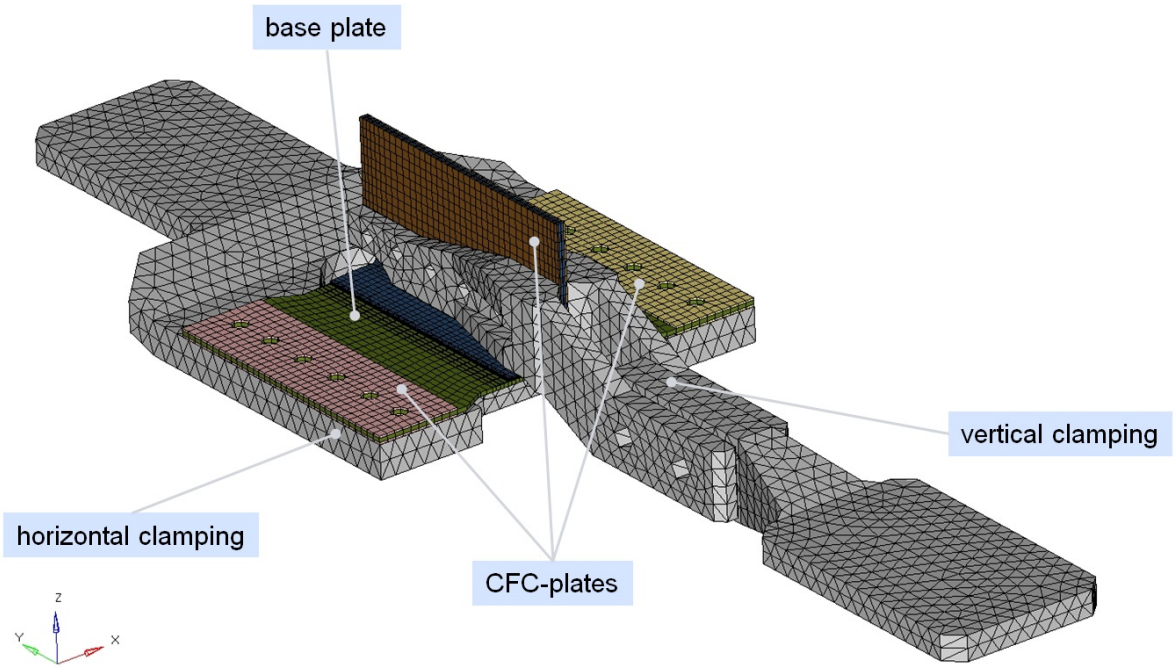


Figure 5.20: Side top view of the clamped undeformed T-Shear-model

A similar element size to the other critical detail models leads to a total amount of 45574 elements of which 10210 elements form the adhesive layers and thus have the CZE character. Both, the vertical and the horizontal bracket are meshed by an unstructured mesh using CTETRA-elements. Since the material of the brackets is isotropic, there is no need to build up a structured mesh as it has been set up for the T-Shear-specimen. In the same time, the applied tetra-meshing facilitates to accurately form the geometry of the brackets.
For the sake of convenience, the connection between the component and the brackets is modeled by fix contact constraints, without modeling the bolts. In this favor, the Node-to-Segment-Algorithm of MSC-Nastran is applied another time to fix the incongruent meshes of the brackets and the component.
No frictional effects are considered in the simulation.

#### 5.3.2.1. Load-displacement behavior and adhesive bondline failure

When a displacement is applied on the model, it starts to deform. While the horizontal bracket stays fix, the vertical bracket moves in the negative y-direction according to figure 5.20.

The induced displacement leads to a downwards bending of the front side of the component at the position where the T-stringer is bonded. The explanation for this downwards bend is based on the lesson of technical mechanics. The fixation of the base plate on the one hand and the displacement of the vertical bracket on the other hand acts like a pair of forces inducing a torsional moment around the x-direction on the component. This downwards bending increases until the cohesive failure starts inside of the CZEs and finally until a delamination is provoked. The predicted delamination of the FEM-simulation is demonstrated in figure 5.21.

At the opposite side (at the backside of the model (y-direction)) the loading conditions leads to a corresponding upwards bending effect of the base plate, due to the same explanation.

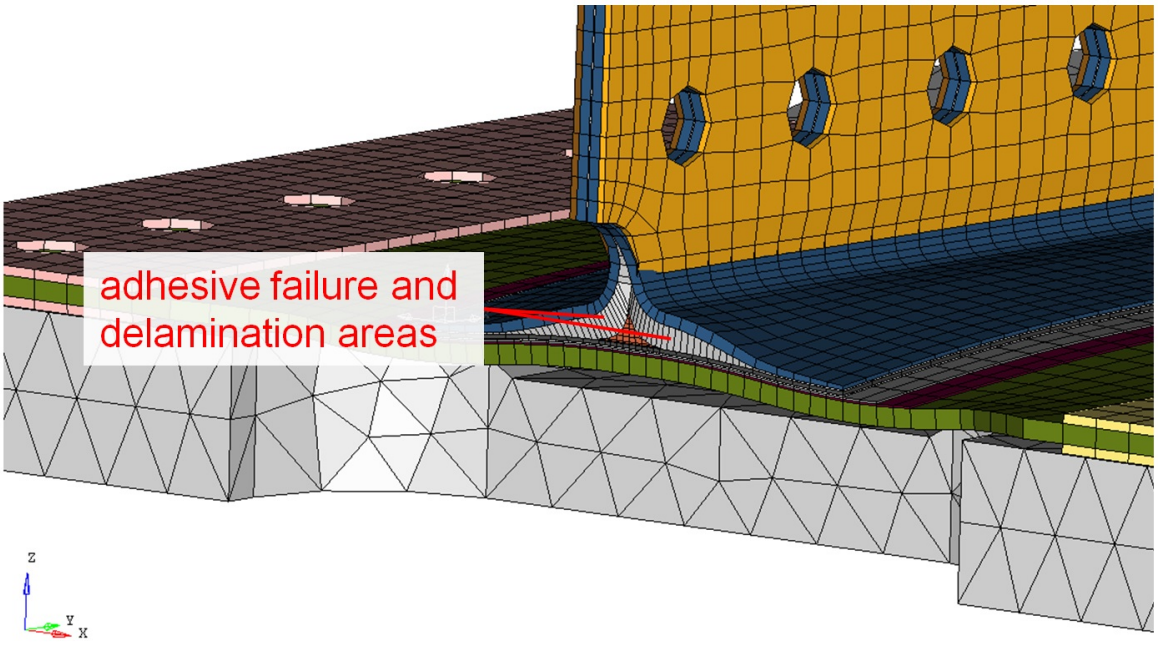


Figure 5.21: Deformed T-Shear-model with a masked vertical bracket to view the deformed CZEs in the component (state of deformation at an equivalent applied load of 79,1kN); graph. scale factor GSF = 5

The deformation of the model leads to high stresses particularly in the adhesive layers between the gusset and both of the blue-colored L-profiles, which form the T-stringer. This

is the position, where the induced loads of the vertical T-stringer arm are transferred to the horizontal part of the component. The two images mapped on the load-displacement-curve (figure 5.22) show that these CZEs start to fail and to delaminate first.

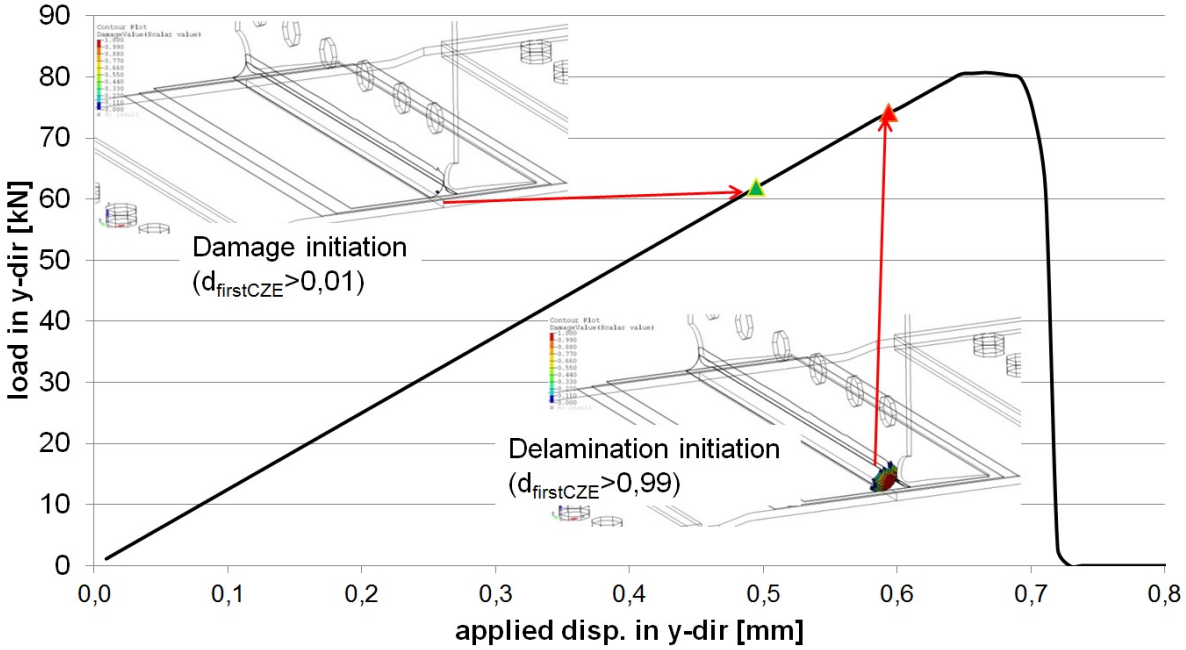


Figure 5.22: Load-displacement-curve of FEM-T-Shear-model; the points of failure initiation and of delamination initiation are marked on the curve

Additionally the correspondent loads for damage initiation and delamination initiation of the model are visible by the markers on the load-displacement-curve. If the curve is compared to the ones of the other two critical details, it is remarkable, that the T-Shear-model possesses a relative high stiffness. The equivalent load of the model reaches already high values at a comparably low applied displacement.
Furthermore, the point of delamination initiation (red marker) at about 74kN does not lead to a major stiffness influence in the model. The significantly decreasing stiffness of the model starts at approximately 80kN and leads finally to a fully delaminated model at an applied displacement of 0,729mm.
The justification of the curve shall be given with the aid of the following damage analysis of the adhesive layers.

#### 5.3.2.2. Damage analysis of the adhesive bondlines

In order to present the simulated damage progress of the model, images of load incre-

ments with specific importance have been assembled in figure 5.23. The blue colored CZEs represent once more the elements possessing a low damage value of $0{,}01 \leq d \leq 0{,}1$ while the red colored CZEs represent the elements possessing a high damage value of $d \geq 0{,}99$. Thus, the red colored CZEs can be considered as fully delaminated.

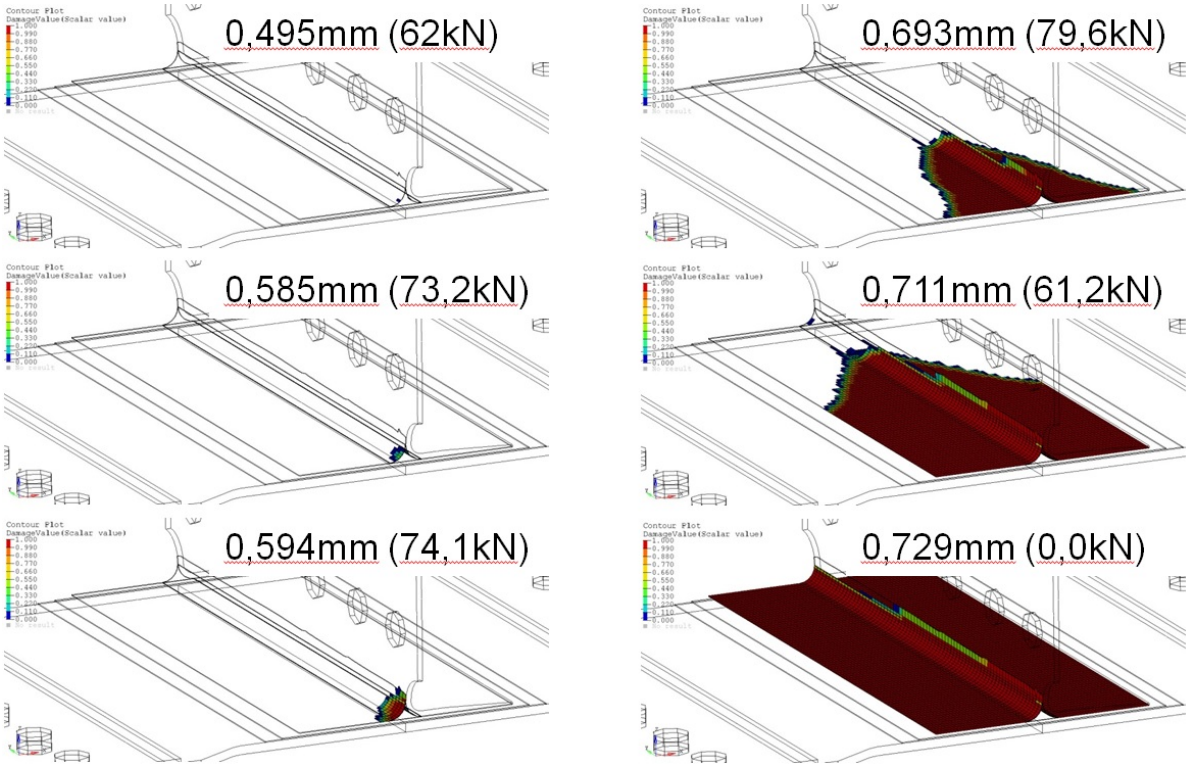


Figure 5.23: Damage evolution of the FEM-T-Shear-model (selection of load increments during delamination progress)

Corresponding to the simualtion of the T-Shear-model the adhesive layers get their first damage at an applied displacement of 0,495mm correlating with a load of 62kN. When another 0,1mm of displacements are applied, the T-stringer begins to delaminate of the gusset at the same spot where the first adhesive failure had been detected before. The component sustains at this moment an equivalent load of 74,1kN.
Instead of immediately extending afterwards, the surface of delamination starts to grow slowly and nearly remains the size which can be seen at the bottom left image in figure 5.23 until a displacement of 0,65mm is applied. The delamination of the model speeds up at this load increment equal to 80kN in such a way that within a few following increments both L-profiles of the T-stringer are fully delaminated of the rest of the model.
Hence, the completely damaged adhesive layer between the capping strip and the L-

profiles can be seen at an applied displacement of 0,729mm (s. figure 5.23). Once this increment is reached, the model naturally does not transfer any loads anymore.

#### 5.3.2.3. Stress analysis of the adhesive bondlines

The stresses in the adhesive are illustrated in figure 5.24 for the load increment of damage initiation in the CZEs at an applied displacement of 0,495mm.

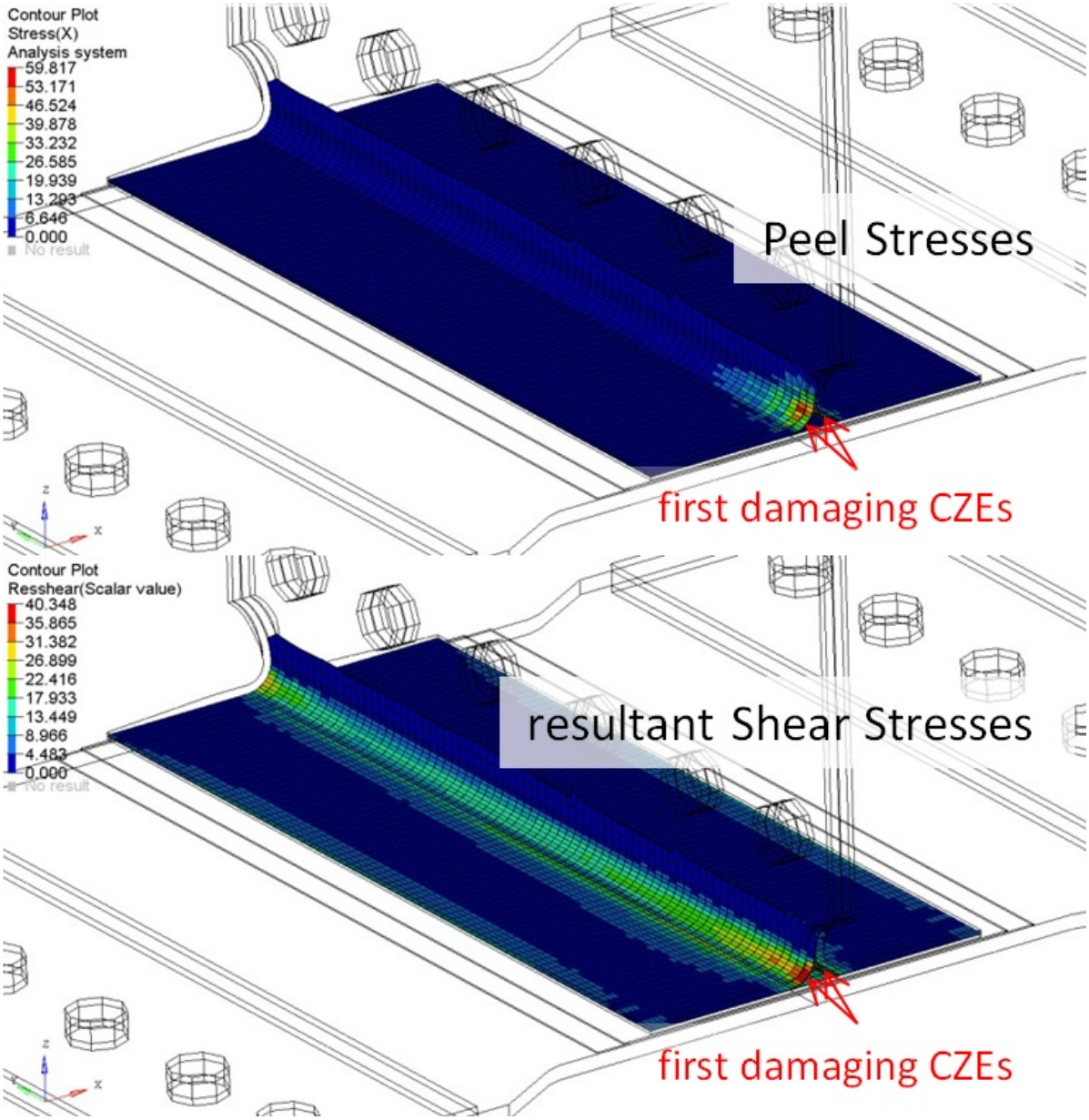


Figure 5.24: State of stress at an applied displacement of 0,495mm, which corresponds to a load of 62kN (point of damage initiation)

The downwards bending effect at the front of the model leads to punctual high peel stresses in the adhesive layer above the gusset. These peel stresses are the most distinct at the front edge of the model.
On the opposite side of the component, there are negative peel stresses in the same area above the gusset. Since negative peel stresses represent a pressure on the adhesive, these stresses do not account for the damage behavior of the CZEs, and thus only peel stresses with a positive value are plotted.

Corresponding to equation (17), the definition of the resultant shear stresses in contrast does not allow any negative shear stresses at all. Compared to the peel stress, the resultant shear stress rises in the whole area above the gusset to a stress value higher than 8,97MPa and it is relatively smooth distributed in the adhesive layer. But even at the plot of the resultant shear stresses it can be detected that they increase towards both ends of the component similarly to the peel stress distribution.

The two CZEs starting to damage ($d \geq$0,01) at the chosen load increment are marked by the red arrows in the figure 5.24. It is similar to the T-Tension-model that the defined maximal stress in shear direction of the adhesive is nearly reached. Both of the CZEs indicate a resultant shear stress values close to 40MPa.
Thus, also the failure initiation of the adhesive layer in the T-Shear-specimen is primarily triggered by shear loading.

### 5.3.3. Rating of FEM results

The judgment of the quality of the simulation is dependent on the test results of the T-Shear-specimen. Not holding any test results of the T-Shear-model yet, the evaluation of the model remains unrealized within this work and should be done in future projects.

The changing of the material input into the MCOHE-card (analog to the other two critical detail models) does not show any significant changes on the load-displacement curve. The named variation is depicted in the appendix D.21. According to this the T-Shear-model is as well not as sensitive as the T-Pull-model.

At a glance on the wall time, the T-Shear-simulation needs $t_{T-Shear} \approx$5h at 400 executed increments. An increment increase up to 800 increments for the T-Shear-simulation does

not influence the quantitative results of the T-Shear-model (s. appendix D.22).

# 6. Conclusion and Recommendations

In the course of this work, several adhesively bonded composite parts have been numerically simulated. The verification of the simulation to reproduce an appearing adhesive failure leads to the following conclusion:

On the material level of the adhesive it has been proven that its elastic properties can be accurately modeled. It is succeeded to correctly model the elastic stiffness of each tested specimen in all the herein presented FEM-models before a damage is initiated. The specific proof is supplied by the stress-strain-curves of the SLS-specimen.
Indeed, these curves of the SLS-simulation also reveal the awareness that the softening of the adhesive could not be precisely simulated. In consideration of the determined CZ-material-input gained by the execution of separate material tests, these CZEs simulate a smaller softening capacity than their corresponding real adhesive.

The failure of the CLS-specimen could not be correctly simulated. For a variation of composite and adhesive mesh sizes, the same critical failure load of 30kN can always be simulated, whereas the tested specimen failed at a load of 55kN. A further mesh refinement of the adhesive elements (meaning a finer local discretization) is not reasonable to model the CLS-specimen. If there were any influences on the resultant critical failure load provoked by a mesh refinement, the failure would have occurred at an even lower load level than the simulated 30kN according to the theory. Anyway, an influence is not expected due to the other results unfolded in the study of the mesh size.
A study of the nonlinear analysis parameter (incremental discretization) proves that the model is fully converged according to C.3. Thus, parameter variations of the CZE-material (s. C.1) have been executed to understand which CZE-parameter could be varied to at least approach the test procedure.
A change of the material parameter would finally enable the correct reproduction of the desired adhesive test failure of the Mojo-Mix adhesive. However, if this is done the origin of the material input of the CZEs can not be explained anymore by the previously executed material tests of the adhesive.

In contrast to the CLS-simulation, the simulations of the critical details provide promising results. Especially the T-Pull-model quantitatively reproduces the adhesive failure

precisely. Even the quality of the simulated type of failure correlates to the majority of failures of the preliminary tests. The predicted T-Tension delamination at a load of 40kN did not occur in the preliminary tests, because a different kind of failure emerged which was not respected by the created CZM-models. The high load at the failing position could however be demonstrated by strain plots of the FEM-model.
Since the simulation of the critical details are funded on the parameter settings of the CLS, it remains dubious why only the CLS-simulation leads to the vast deviations.

The otherwise suitable simulations of adhesive failure in the bonded composite components are based on the occurring adhesive loading conditions. As every herein simulated adhesive failure originates mainly from a too high shear loading, the size of the CZEs is of minor relevance in comparison to the accuracy of the results. Corresponding to the theory, the detected unsensitivity of varying the CZE-size under shear loading conditions allows the application of relatively coarse meshes on the studied FEM-models. A further coarsening of the models was introduced by the use of the contact approach, combining the defined adhesive CZE-mesh with an even coarser composite mesh. The herewith used methods to keep the models as coarse as possible led to a significant reduction of the computing time.

Nevertheless, the analysis of the critical details needs up to 6 hours of wall time. A simulation of the airbrake at the end of the validation pyramid of the project would thus need several days under the conditions which have been developed on the element and the detail level. According to this, the effort to simulate a large complex adhesively bonded composite structure is estimated to be high and still needs further verification.

Since all processed components were subjected to a primary shear load, the question remains how comparable adhesively bonded composite models would react on a primary normal loading condition. It could form a further prospective research project to determine whether the chosen discretizations of the models are still applicable under normal load conditions to accurately predict an adhesive peel failure. Then again, it has to be taken into account that adhesive joints are typically designed to transfer shear load in technical structures.

For the model creation in this work, the preprocessor HyperMesh 13.0 has been used.

Unfortunately, HyperMesh 13.0 is not fully harmonized with the newest features of the utilized Nastran version V2014 R1 and thus, not all of the required input data of the Nastran input file could be directly generated. Neither the property of the solid composite elements (PCOMPLS) nor the cohesive zone elements and their properties (CIFHEX, PCOHE) nor the contact could be generated directly in HyperMesh 13.0. Thus, I recommend for future projects to directly use the recent version of Patran. The pre- and post processor Patran is like the solver Nastran a software tool of the MSC Software Corporation and hence both are harmonized to each other.
Additionally, the use of several property cards of the CZEs (PCOHE-cards) in conjuction with the applied contact algorithm led to problems at the used Nastran version V2014 R1. Thus, it was not possible to model multiple different adhesives in one component in the same time under the specified conditions. According to the statement of the customer support of MSC Nastran, this will be possible in the next version of Nastran. This innovation will help to specify the adhesive CZM-models more detailed in prospective projects.
Since several basic investigations have been executed on the CLS-specimen so far, the knowledge on the element level could already be strengthened within the company of Airbus Defence & Space. Finally, it allows to compare different studies and it helps to understand model-specific problems. For this reason, I recommend to investigate further on the detail level of the validation pyramid.

In summary, this work simulates adhesively bonded components via the CZM exceeding the coupon level of single-mode tests. In the process, the simulation of the film adhesive „Hysol EA9695“ provides accurate simulation results on the detail level. Until now, few nonlinear analysis based on the CZM risked to proceed this far. That is why this work contributes to increase the suitability of the CZM for the daily engineering use to simulate the failure of adhesive joints.

# References

[1] **MSC SOFTWARE CORPORATION** (2014): *„MSC Nastran 2014 Nonlinear User's Guide SOL 400“*, 4675 MacArthur Court, Suite 900, Newport Beach, CA 92660

[2] **MSC SOFTWARE CORPORATION** (2014): *„MSC Nastran 2014 Quick Reference Guide“*, 4675 MacArthur Court, Suite 900, Newport Beach, CA 92660

[3] **MSC SOFTWARE CORPORATION** (2015): *„MSC Nastran, Multidisziplinäre FEA-Lösung“*, 4675 MacArthur Court, Suite 900, Newport Beach, CA 92660, MSC Nastran homepage, URL: http://www.mscsoftware.com/de/product/msc-nastran [status: 20.10.2015]

[4] **MSC SOFTWARE CORPORATION** (02/2012): *„Section 2: Solid Composites“*,presentation at composites technology day, 4675 MacArthur Court, Suite 900, Newport Beach, CA 92660

[5] **Douglas MARRIOTT** (06/2013): *„THEORY SERIES: Implicit vs Explicit - Introduction“*, MSC Software UK Nonlinear, Articles and links for the MSC UK Nonlinear community, URL: http://mscsoftwareuk.blogspot.de/2013/06/theory-series-implicit-vs-explicit.html [status: 19.07.2015]

[6] **T. LÖBEL et al.** (2015): *„Fatigue evaluation and enhanced shear strain measurements of bonded composite joints“*, report of 10th International Conference on Composite Science and Technology, DLR, German Aerospace Center (Braunschweig)

[7] **Dr. Christian MEIER** (09/2011): *„So schwer ist's mit dem Leichtgewicht“*, Bild der Wissenschaft online, Technik & Kommunikation, URL: http://www.bild-der-wissenschaft.de/bdw/bdwlive/heftarchiv/index2.php?object_id=32714169 [status: 17.06.2015]

[8] **L. J. HART-SMITH** (03/1978): *„Technology conference associates, conference on advanced composites technology“*, Douglas Aircraft Company, McDonnell Douglas Corporation, El Segundo, California

[9] **ESA** (1995): *„Adhesive Bonding Handbook for advanced structural materials“*, Structures and Mechanisms Division, European Space Research and Technology Centre, Noordwijk, Netherlands

[10] **P. CZARNOCKI, K. PIEKARSKI**: *„Yielding of Adhesives“*,university of Waterloo, Journal of Materials Science, Springer

[11] **G. KELLY** (2004): *„Joining of Carbon Fibre Reinforced Plastics for Automotive Applications“*, tech. report, Department of Aeronautical and Vehicle Engineering, Royal Institute of Technology, Sweden

[12] **J.W. VAN INGEN, A. VLOT** (1993): *„Stress Analysis of Adhesively Bonded Single Lap Joints“*, tech. report LR-740, Survey and Evaluation of Analysis, Faculty of Aerospace Engineering, Structures and Materials Laboratory, TU Delft, Netherlands

[13] **H. SCHÜRMANN** (2005/2007): *„Konstruieren mit Faser-Kunststoff-Verbunden“*,zweite bearbeitete und erweiterte Auflage, Springer-Verlag Berlin Heidelberg

[14] **D. GROSS et al.** (2013): *„Technische Mechanik 1“*,zwölfte aktualisierte Auflage, Springer-Verlag Berlin Heidelberg

[15] **D. GROSS et al.** (2014): *„Technische Mechanik 2“*,zwölfte aktualisierte Auflage, Springer-Verlag Berlin Heidelberg

[16] **SOLIDWORKS CORPORATION** (2011): *„Die Nicht-Lineare Analyse“*,advisor for FEA, Dassault Systèmes, 300 Baker Avenue Concord, MA 01742

[17] **L. F. M. DA SILVA et al.**: *„Closed-form solutions for adhesively bonded joints“*, Departamento den Engenharia Mecânica e Gestao Industrial, Faculdade de Engenharia da Universidade de Porto, 4200-465 Porto, Portugal

[18] **Prof. Dr.-Ing. D. SCHULZE** (WS2014/15): *„Computational Fluid Dynamics“*, script for lecture, Hochschule für angewandte Wissenschaften (HAW) Hamburg, Berliner Tor 9, Department F+F, 20099 Hamburg

[19] **J. ANKERSEN, G. A. O. DAVIES**: *„Interface elements - advantages and limitations in CFRP delamination modelling“*, tech. report, department of aeronautics, imperial college london, UK

[20] **Marc Villa MONTERO** (2014): *„Capability Assessment of a Virtual Testing Software in Progressive Failure Analysis and its Material Characterisation Module“*, master thesis, Lulea University of Technology, Department of Engineering Sciences and Mathematics, Airbus Defence&Space, Manching

[21] **M. BORDOGNA** (2014): *„Benchmark of MSC Marc to evaluate its cohesive element capabilities“*, internal internship report, Airbus Defence&Space, Manching

[22] **M. WEILAND** (2014): *„FE-Analysis of adhesive joints at composite structures with P-FEM“*, master thesis, Technische Hochschule Ingolstadt, Faculty Mechanical Engineering, Airbus Defence&Space, Manching

[23] **BOPACS** (2014): *„CLS Benchmark Discription“*, Airbus Defence & Space Manching, TAECA24, Airbus Group

[24] **F. H. HERMES** (09/2010): *„Prozess zone and cohesive element size in numerical simulations of delamination in bi-layers“*, master thesis, Philips Applied Technologies, Eindhoven University of Technology, Eindhoven

[25] **C. G. DAVILA, P. P. CAMANHO, A. TURON, J. COSTA** (2005): *„An Engineering Solution for solving Mesh Size Effects in the Simulation of Delamination with Cohesive Zone Models“*

[26] **C. G. DAVILA, P. P. CAMANHO, A. TURON** (2007): *„Effective Simulation of Delamination in Aeronautical Structures Using Shell and Cohesive Elements“*, journal of aircraft

[27] **C. G. DAVILA, P. P. CAMANHO, A. TURON, J. COSTA** (01/2005): *„A Damage Model for the Simulation of Delamination in Advanced Composites under Variable-Mode Loading“*, AMADE (uni. of Girona), DEMEGI (uni. of Porto), NASA (Virginia)

[28] **A. TURON** (2006): *„Simulation of delamination in composites under quasi-static and fatigue loading using cohesive zone models“* thesis for the degree of doctor of philosophy, university of Girona

[29] **European Aviation Safety Agency (EASA)** (07/2015): *„Certification Specifications and Acceptable Means of Compliance for Large Aeroplanes CS-25“*, Amendment 17

[30] **NATIONAL INSTITUTE FOR AVIATION RESEARCH (NIAR)** (04/2011): *„Hexcel 8552 IM7 Unidirectional Prepreg 190gsm & 35%RC Qualification Material Property Data Report“*, NIAR, National Center for Advanced Materials Performance (NCAMP), NASA, Wichita State University

[31] **T. LOEBEL**: *„Rohrprobenprogramm EA9695 0.05 PSF NW“*

[32] **M.CALOMFIRESCU et al.**: *„FFS-Fortschrittliche Flugzeugstrukturen: Übersicht über die 5. Phase des Leitprojektes zur Erschließung neuer Technologien für Composite Strukturen für zukünftige, militärische Flugzeugplattformen“*, Airbus Defence and Space GmbH (Manching), DLR Institut für Faserverbundleichtbau und Adaptronik (Braunschweig), DLR Institut für Bauweisen und Strukturtechnologie (Stuttgart), WIWeB (Erding), Airbus Group Innovations (Ottobrunn)

[33] **F. ALTENWEGNER et al.** (03/2010): *„Kleben von Composites; Kennwertermittlung zur Berechnung von strukturellen Klebungen“*, Labor Klebetechnik und Verbundwerkstoffe, Hochschule Landshut

[34] **F. ALTENWEGNER et al.** (2014): *„Bestimmung von Werkstoffkennfunktionen eines Strukturklebstoffs“*, Hochschule Landshut und Airbus Group Innovations (München)

[35] **I.S. FLOROS, K.I. TSERPES, T.LÖBEL** (04/2015): *„Mode-I, Mode-II and Mixed-Mode I+II fracture behavior of composite bonded joints: Experimental characterization and numerical simulation“*, composites part B report, Laboratory of Technology & Strength of Materials, University of Patras, DLR (Braunschweig)

[36] **L.TONG, Q. LUO** (2008): *„Analysis of Cracked Lap Shear (CLS) Joints“*, Chapter 2 of Modeling of Adhesively Bonded Joints , Springer-Verlag Berlin Heidelberg

[37] **POPOV** (WS2003/04): *„Die elastische Linie des Biegeträgers (Biegelinie)“*, script of studies, chapter 10.6 TU Berlin

[38] **J. M. CORUM et al.** (02/2000): *„Basic properties of reference crossply carbon-fiber composite“*, Engineering Technology Division of Oak Ridge National Laboratory, Lockheed Martin, Tennessee, USA

[39] **M. A. Chowdhury et al.** (2013): *„Experimental Investigation of Friction Coefficient and Wear Rate of Composite Materials Sliding Against Smooth and Rough Mild Steel Counterfaces“*, Departement of Mechanical Engineering, Dhaka University of Engineering and Technology, Gazipur, Bangladesh

[40] **E. NAST** (2014): *„Umdruck zur Lehrveranstaltung Faserverbundtechnologie“*, script of lecture, department of Aeronautical Engineering, HAW Hamburg

[41] **A. RODRIQUEZ** (2001): *„Carbon Composite Repair with Hysol EA 9695 to AIMS 08-05-000“*, technical service laboratory report, Loctite Aerospace, CASA, Spain

[42] **D. C. NOORMAN** (09/2014): *„Cohesive Zone Modelling in Adhesively Bonded Joints“*, master thesis, TU Delft

[43] **M. SEIBEL** (SS2014): *„Entwurf und Dimensionierung von Faserverbundstrukturen“*, script of lecture, department of Aeronautical Engineering, HAW Hamburg

[44] **K. SONG et al.** (2008): *„Guidelines and Parameter Selection for the Simulation of Progressive Delamination“*, Abaqus Users' Conference, Swales Aerospace / ATK Space, Hampton VA23669

[45] **R. NEELY**: *„Grid Generation“*, NASA Research Center, URL: http://images.google.de/imgres?imgurl=http%3A%2F%2Fntl.bts.gov%2Fimages%2F316.gif [status: 08.02.2016]

# A. Appendix for Theoretical Background

## A.1. Adhesive lap joints

| | Material linearity | | | | Adherends | | | | | Adhesive stresses | | | Solution | |
|---|---|---|---|---|---|---|---|---|---|---|---|---|---|---|
| | Adhesive | | Adherend | | | | | Dissimilar | | | | | | |
| | Linear | Nonlinear | Linear | Nonlinear | Isotropic | Composite | Similar | Thickness | Material | $\sigma_x$ | $\sigma_y$ | $\tau_{xy}$ | Closed-form | Numerical |
| Volkersen (1938) | X | | X | | X | | X | X | | | | X | X | |
| Goland and Reissner (1944) | X | | X | | X | | X | | | | X | X | X | |
| Wah (1973) | X | | X | | X | X | X | X | | | X | X | X | |
| Hart-Smith (1973a,b) | X | X | X | | X | | X | | | | X | X | X | |
| Pirvics (1974) | X | | X | | X | | X | X | X | X | X | X | | X |
| Grimes and Greimann (1975) | X | X | X | X | X | X | X | X | X | | X | X | | X |
| Renton and Vinson (1975) | X | | X | | X | X | X | X | X | | X | X | X | |
| Srinivas (1975) | X | | X | | X | X | X | X | X | | X | X | | X |
| Allman (1977) | X | | X | | X | X | X | | | | X | X | | X |
| Bigwood and Crocombe (1989) | X | | X | | X | | X | X | X | | X | X | X | |
| Bigwood and Crocombe (1990) | X | X | X | | X | | X | X | X | | X | X | | X |
| Cheng et al. (1991) | X | | X | | X | | X | X | X | X | X | X | X | |
| Crocombe and Bigwood (1992) | X | X | X | X | X | | X | X | X | | X | X | | X |
| Adams and Mallick (1992) | X | X | X | | X | X | X | X | X | X | X | X | | X |
| Yang and Pang (1996) | X | | X | | X | X | X | X | X | | X | X | X | |
| Frostig et al. (1999) | X | | X | | X | X | X | X | X | | X | X | | X |
| Sawa et al. (2000) | X | | X | | X | | X | X | X | X | X | X | | X |
| Mortensen and Thomsen (2002) | X | X | X | | X | X | X | X | X | | X | X | | X |
| Adams and Davies (2002) | X | X | X | X | X | | X | | | | | | X | |

Figure A.1: Summary of both linear and nonlinear two-dimensional analytical models available in the literature [17]

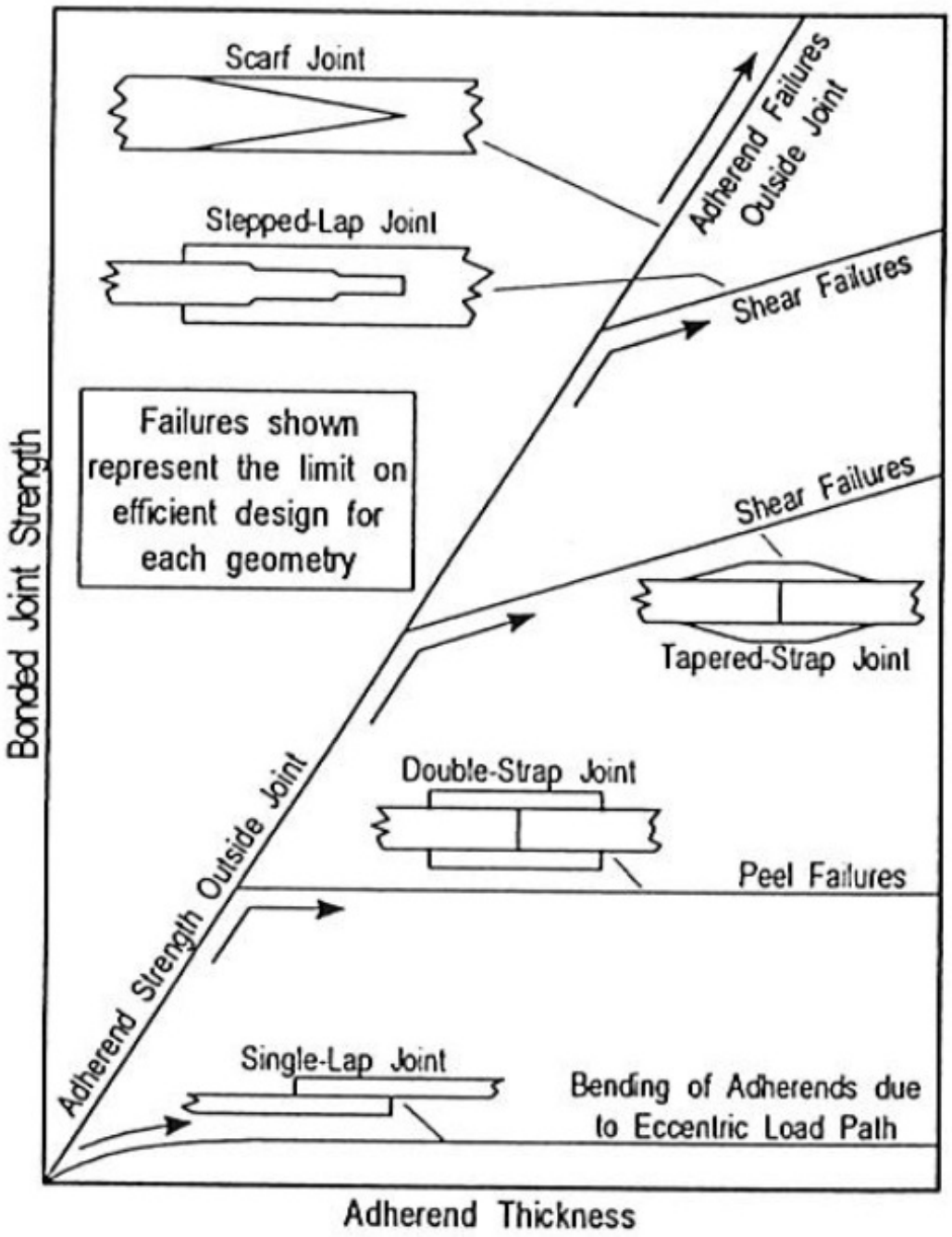


Figure A.2: Hart-Smith-diagram: the strength of different adhesively bonded joint types is shown over the adherent thickness corresponding to [8]

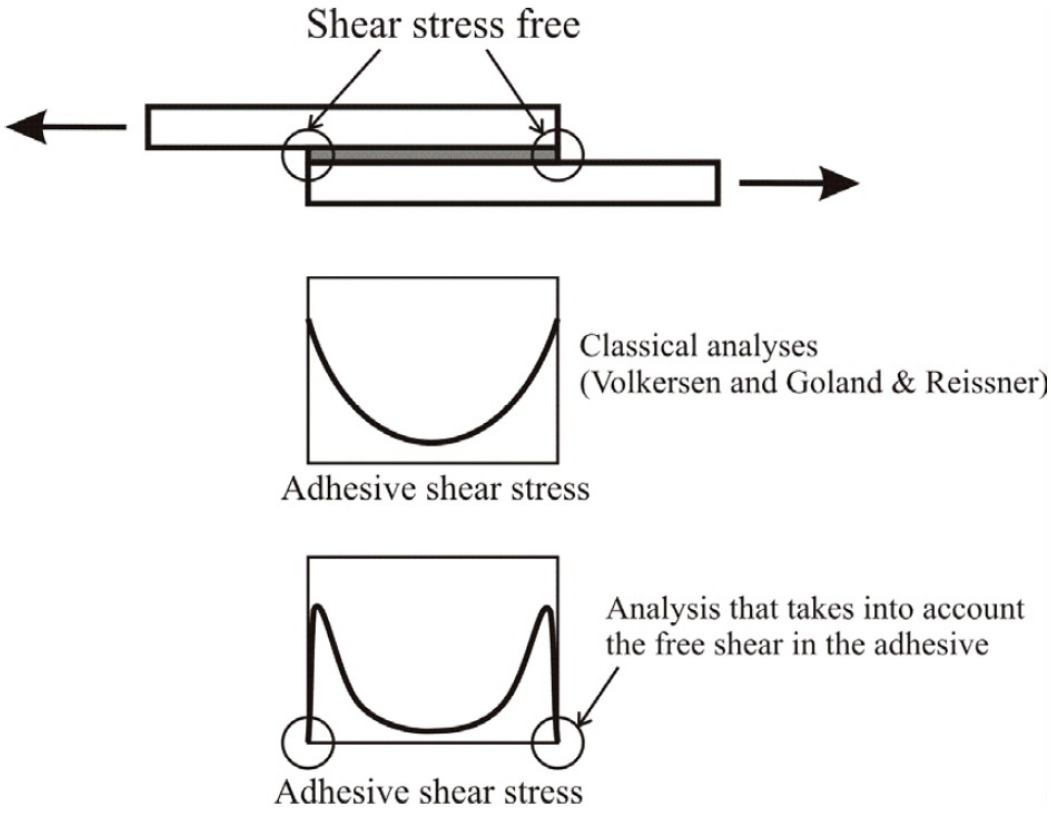


Figure A.3: Adhesive shear stress distribution when the stress free condition at the ends of the overlap is verified according to [17]

## A.2. Mechanical structure analysis

The technical mechanic is the lesson of movement of structural bodies influenced by loading forces according to [14]. Simultaneously, the technical mechanic distinguishes between static and kinetic systems. In doing so, the kind of system depends on its technical constraints and thus, on its degrees of freedom. The multitude of mechanically regarded systems are static systems, like the studied adhesively bonded composite parts in this work.

In general, the mechanical structure analysis is a useful tool to dimension whatever kind of structural component. By calculating the deformation and strains of a component under specific load cases, its stress-tensor can be determined. Furthermore, the existing analyzed stresses can afterwards be set into relation with the stress allowable of the material. This gives information whether the structure fails or resists the applied loads.

A proper structure analysis is done to guarantee necessary safety against the failure of a structural component. The structure analysis goes always side by side with mechanical tests proving the suitable field of application for the analysis. In economic regards, the application of a structure analysis has its main purpose in saving cost expended for the materials, the assembly and the fitness of a component.
On the one hand, the structure analysis benefits fewer necessary tests (s. [29]). On the other hand, a simultaneous process of test and analysis (as you can see in figure 1.2) leads to more know-how in the development of technical components.

### A.2.1. Linear Analysis

The linear static analysis is the most commonly used form of structure analysis. It is based on the linear stiffness $K$ of a component [16]. The stiffness is a property which describes the deformation $u$ of a loaded component by an applied load $P$.

$$P = K \cdot u \tag{24}$$

In this connection the stiffness $K$ is dependent on different factors.
Primarily, the **material** of a component influences its stiffness. A linear material behavior is expressed by the elasticity law, which has been established in 1676 by R. Hooke. The elasticity law relates strains and stresses in a material. The dependent coefficient be-

tween both is the material specific modulus of elasticity $E$ [15]. If a critical stress value (s. limit load in figure 3.1) is exceeded through loading conditions, the material will start to deform plastically and hence, the modulus of elasticity decreases.
Secondly, the **geometrical shape** of a component codetermines its stiffness. If the deformation of a structural component is high or takes influence on the loading behavior, geometrical nonlinearity is present. A rule of thumb states according to [16] that geometrical nonlinearities have to be respected if a deformation of more than a twentieth part of the largest component dimensioning is present.
The last influence on the stiffness is given by the **boundary conditions** of a component. If a different clamping of a component is chosen it effects the deformation at an unchanged load.
If none of these three factors influence the stiffness significantly, a linear analysis of the component is appropriate. A linear stiffness leads to the fact that the analyzed component will gain back its initial state when its loading forces $P$ are removed.

The linearity between loading and deformation offers a simple principle of superposition of single loads to get the results of a complex load case of multiple loads.

### A.2.2. Nonlinear Analysis

In contrast to the linear structure analysis, the nonlinear structure analysis is designed to analyse a structure in which significant stiffness changes are present. Material, geometrical or boundary nonlinearities [1] lead, thus, to the following change of equation (24):

$$P = K(P, u) \cdot u \tag{25}$$

The changing of the stiffness matrix $K$ accounts for an iterative solution algorithm to get accurate results. The quantity of nonlinearities in the stiffness matrix determines appropriate parameters for the solution algorithm. If a high-grade area of nonlinearities is reached in a structural analysis, this area needs to be more accurately simulated. The convergence of the constitutive equation obtains in this context an important meaning.

#### Convergence

To satisfy the nonlinear stiffness changing in the model, the final state of deformation

is approximated by an incremental solution scheme of stringed together linear analysis. The load $P$ is hence increasingly applied in an iterative manner until the final full load value is reached. The breakdown of the analysis into several increments implies that the computing time rises consequently with the amount of increments.
The aim for a suitable FEM model is always to get most efficiently accurate results. Thus, the computing costs should stay at a low level, while the analysis results should reach a certain level of quality. The level of quality is expressed by the convergence fault of the analysis.

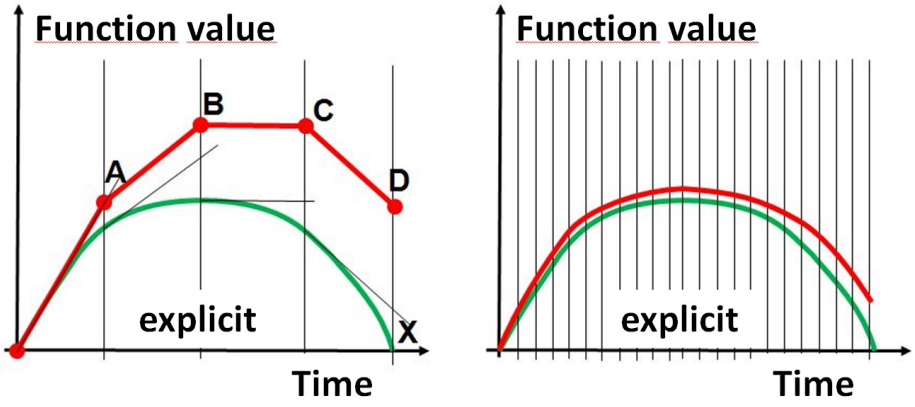


Figure A.4: Visualisation of an explicit method of resolution

In figure A.4, a comparison between the analytical correct solution (green curve) and the solution of an explicit nonlinear solution algorithm (red curve) is depicted.
Thus, the aim of the nonlinear numerical analysis is in this case to accurately reproduce the analytical function. In this purpose, the nonlinear analysis is divided into the typical increments. At each increment in the explicit nonlinear analysis the calculated end function value of the previous increment is taken as the start function value for the next increment. In order to calculate the end function value of an increment the function is derived at the start point. Using the derivation at the start point, the gradient in this point is determined so that a linear tangent approach can be fulfilled for the approximation of the increment. The higher the curvature of the function and the taller the chosen increment, the heavier the convergence fault $ERR_{conv,explicit}$ rises. The latter is demonstrated in figure A.4, by comparing the left and the right image.

The explicit solution algorithm provides a relatively fast approach for a nonlinear analysis. Unfortunately, it leads to a summation of convergence faults of each increment and

thus, a significant deviation is the result. According to [5] the explicit solution algorithm therefore requires a small incremental size and is favorable on high speed simulations as for instance to simulate crashes or impacts.

In order to control the quantity of the convergence faults the implicit solution algorithm is introduced. In each increment, the solver tries to satisfy the algebraic transformed equation (24).

$$P_{analytisch} - k_{analytisch} \cdot u_{analytisch} = 0 \tag{26}$$

The implicit solution algorithm shows its benefits on static, quasi-static and long duration events. In the analyzing process, multiple iterations are solved during one single increment until the convergence fault $ERR_{conv,implicit}$ of the current increment falls below a specified value, as it is mapped in figure A.5.

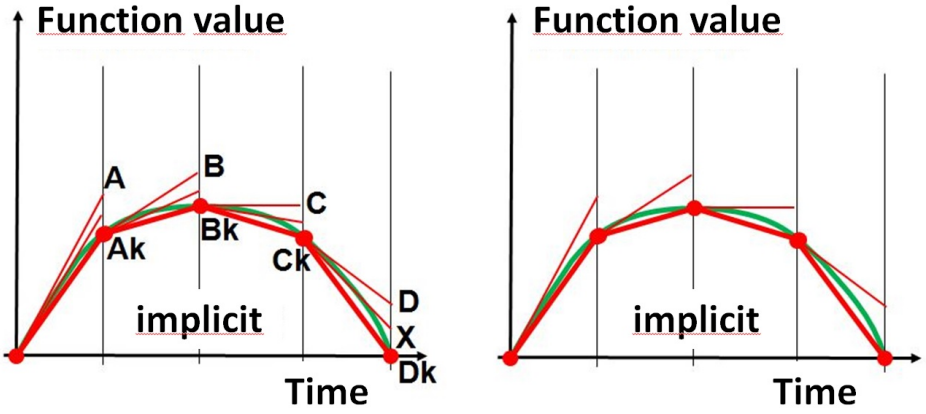


Figure A.5: Visualisation of an implicit method of resolution

A popular method to numerically evaluate a function value at a certain time step of a specific function is the Newton-Raphson-Method. This method is often used to iteratively approximate an analytical function.

$$P_{implicit,i} - k_{implicit,i} \cdot u_{implicit,i} = Error_{implicit,i} \geq 0 \tag{27}$$

For the present work, the nonlinear results are approximated along the recommendation of [5] by using the implicit solution algorithm and the Newton-Raphson-Method.
There exist three main methods in a nonlinear structural FEM-analysis to control the convergence using the implicit solution algorithm (s. [1]). These three methods result out of the parameters of the constitutive equation (27).

Utilizing the first method, convergence can be controlled by the **residual (P)** checking iteratively the residual force against the reaction force in the model. If the ratio gets under a specified value, convergence is achieved for the increment.
The second method of convergence controlling is to compare the maximum **displacements (U)** of the current iteration with the displacements of the previous iteration. The difference between both has to get under a certain level.
The third method is the control of **strain energy (W)** which basically works like the second method. By this method the whole model is checked iteratively.
MSC Nastran proposes to use a convergence error of 0,1 to mechanically analyze a structure. This is kept within all the executed analysis. The convergence check is done via the force and the displacement convergence method (UPV).

Because the discretisation is based on iterative linear approximations of the constitutive equation, the implicit solution algorithm needs more iterations to obtain convergence, in areas, where the constitutive equations have high nonlinearities.

# B. Appendix for determination of Cohesive Zone material parameter

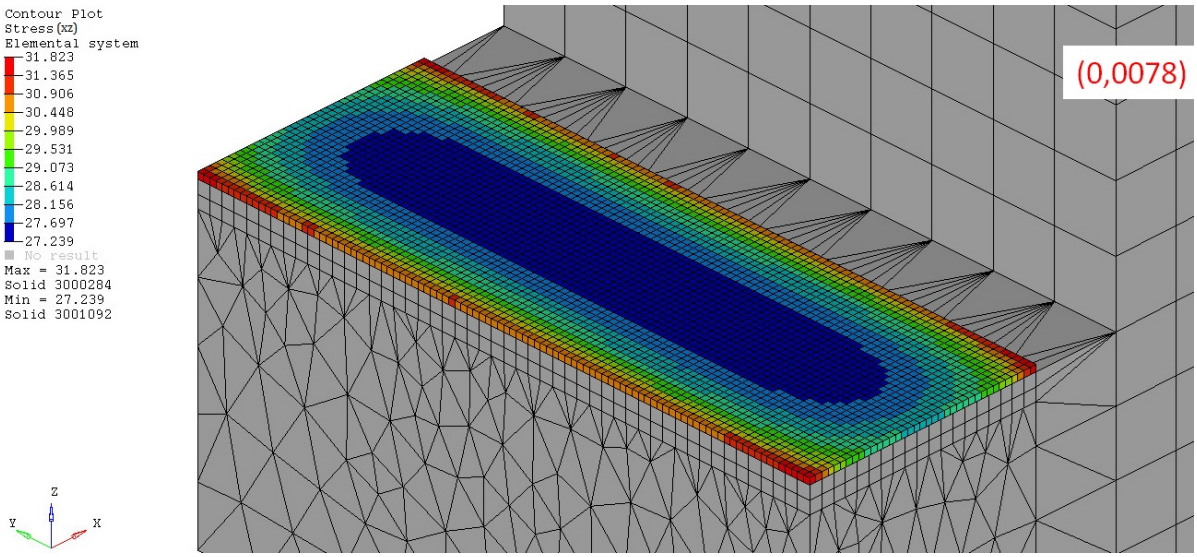


Figure B.1: shear stress $\tau_{shear}$ distribution over adhesive layer, for linear-elastic undamaged behavior at an applied displacement in x-direction of 0,0078mm

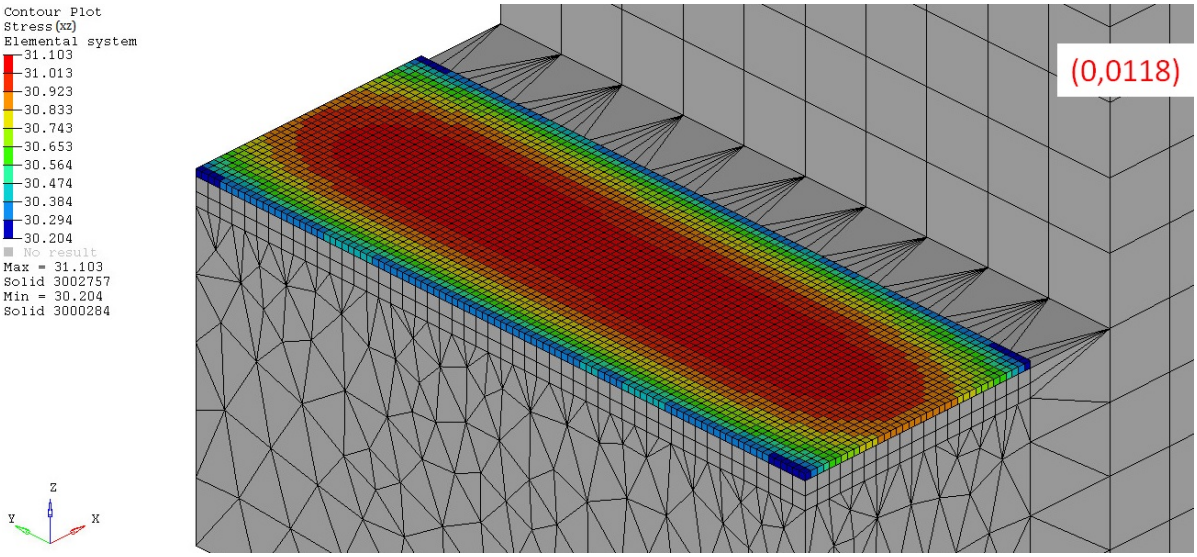


Figure B.2: shear stress $\tau_{shear}$ distribution over adhesive layer, for plastic behavior, with partly damaged CZE at an applied displacement in x-direction of 0,0118mm

Table 7: Material Parameter of „Mojo-Mix“-adhesive

| **Parameter** | **magnitude** | **origin** |
|---|---|---|
| $E_n$ | 4035MPa | (LTSM, Uni Patras) [23] |
| $G$ | 720MPa | (LTSM, Uni Patras) BBHC tests [23] |
| $\tau_n$ | 64MPa | (LTSM, Uni Patras) [23] |
| $\tau_{shear}$ | 35MPa | (LTSM, Uni Patras) BBHC tests [23] |
| $G_{Cl}$ | 0,32N/mm | (LTSM, Uni Patras) average of area calc. and usage of SBT [23] |
| $G_{Cll}$ | 0,5N/mm | (LTSM, Uni Patras) average of CBBM and Norm:AITM [23] |
| $\beta_1$ | 0,546875 | $\frac{t_{shear}}{t_n}$ |
| $\beta_2$ | 1,52439 | $\frac{G_{shear}}{G_n}$ |
| $\alpha$ | 1 | |
| $K_{el,n}$ | $\frac{4035N/mm^2}{th_{CZE}}$ | equation 12 |
| $K_{el,shear}$ | $\frac{720N/mm^2}{th_{CZE}}$ | equation 12 |
| $\nu_{c,n}$ | $0,01586 \cdot th_{CZE}$ | $= \frac{t_n}{K_{CZEn}}$ |
| $\nu_{c,shear}$ | $0,04861 \cdot th_{CZE}$ | $= \frac{t_{shear}}{K_{CZEshear}}$ |
| $\nu_{max,n}$ | 0,01025mm | $= \frac{G_n \cdot 2}{t_n}$ |
| $\nu_{max,shear}$ | 0,02857mm | $= \frac{G_{shear} \cdot 2}{t_{shear}}$ |

Table 8: Material parameter of „Loctite Hysol EA9695“-adhesive

| **Parameter** | **magnitude** | **origin** |
|---|---|---|
| $E_n$ | | Rohrprobenprogramm DLR [31] |
| $G$ | | Loctite Report [41] |
| $\tau_n$ | | equation 20 |
| $\tau_{shear}$ | | Loctite Report [41] |
| $G_{Cl}$ | 1,01852N/mm | Tinius Olsen H5K-S UTM tensile test [35] |
| $G_{Cll}$ | 0,78341N/mm | MTS universal test [35] |
| $\beta_1$ | | $\frac{t_{shear}}{t_n}$ |
| $\beta_2$ | | $\frac{G_{shear}}{G_n}$ |
| $\alpha$ | 1 | |
| $K_{el,n}$ | | equation 12 |
| $K_{el,shear}$ | | equation 12 |
| $\nu_{c,n}$ | | $= \frac{t_n}{K_{CZEn}}$ |
| $\nu_{c,shear}$ | | $= \frac{t_{shear}}{K_{CZEshear}}$ |
| $\nu_{max,n}$ | | $= \frac{G_n \cdot 2}{t_n}$ |
| $\nu_{max,shear}$ | | $= \frac{G_{shear} \cdot 2}{t_{shear}}$ |

Table 9: Property-PCOHE-card for the CZEs according to [2]

| PCOHE | PID | MID | 1 | | GRID | 0 | | | |
|---|---|---|---|---|---|---|---|---|---|

Table 10: Material-MCOHE-input for the CZEs simulating the „Mojo-Mix“-adhesive according to [2] and table 7

| MCOHE | MID | 1 | | | | | | | + |
|---|---|---|---|---|---|---|---|---|---|
| + | 0.328 | 9.517e-5 | 0.01025 | 0.546875 | | | | | + |
| + | 1.52439 | | | | | | | | |

Table 11: Material-MCOHE-input for the CZEs simulating the „Loctite Hysol EA9695“-adhesive according to [2] and table 8

| MCOHE | MID | 1 | | | | | | | + |
|---|---|---|---|---|---|---|---|---|---|
| + | 1.01852 | [redacted] | | | | | | | + |
| + | 0.769165 | | | | | | | | |

# C. Appendix for CLS

Table 12: CFC Material Hexcel IM7 8552 [30] (p.1)

| | | | | | | |
|---|---|---|---|---|---|---|
| **Prepreg Material:** | Hexcel Corporation - Hexcel 8552 IM7 Unidirectional NMS 128/2 Material Specification | | | | **Hexcel 8552 IM7 Unidirectional Tape Lamina Properties Summary** | |
| **Fiber** | IM7 unidirectional | **Resin** | Hexcel 8552 | | | |
| **Tg(dry)** | 406.43 °F | **Tg(wet)** | 321.41 °F | | | |
| **PROCESSING:** | NPS 81228 "M" Cure Cycle | | | **Tg METHOD** | DMA (SRM 18-94) | |

| | Lot 1 | Lot 2 | Lot 3 | | |
|---|---|---|---|---|---|
| **Date of fiber manufacture** | 01/26/2007 | 12/25/2006 | 02/05/2007 | **Date of testing** | 1/22/2008 - 3/4/10 |
| **Date of resin manufacture** | 02/28/2007 | 01/24/2007 | 03/01/2007 | **Date of data submittal** | 4/5/2010 |
| **Date of prepreg manufacture** | 02/28/2007 | 01/24/2007 | 03/01/2007 | | |
| **Date of composite manufacture** | 9/2007 to 10/2007 | | | | |

**LAMINA MECHANICAL PROPERTY SUMMARY**
**Data reported as: Normalized & Measured**
**(Normalized by CPT= 0.0072 inch)**

| | CTD Mean | | RTD Mean | | ETD Mean | | ETW Mean | |
|---|---|---|---|---|---|---|---|---|
| | Normalized | Measured | Normalized | Measured | Normalized | Measured | Normalized | Measured |
| $F_1^{tu}$ (ksi) | | | | | | | | |
| from LT | 357.39 | 353.70 | 362.69 | 371.08 | --- | --- | 333.50 | 327.96 |
| from UNT0 | 286.78 | 281.57 | 324.62 | 320.79 | --- | --- | 346.85 | 340.46 |
| $E_1^t$ (Msi) | | | | | | | | |
| of LT | 22.57 | 22.33 | 22.99 | 23.51 | --- | --- | 24.00 | 23.77 |
| E (Msi) | | | | | | | | |
| of UNT0 | 11.92 | 11.71 | 11.99 | 11.85 | --- | --- | 11.94 | 11.74 |
| $\nu_{12}^t$ | | 0.270 | | 0.316 | | | | 0.393 |
| $F_2^{tu}$ (ksi) | --- | 9.60 | --- | 9.29 | --- | --- | --- | 3.49 |
| $E_2^t$ (Msi) | --- | 1.46 | --- | 1.30 | --- | --- | --- | 0.81 |
| of TT | | | | | | | | |
| $F_1^{cu}$ (ksi) | | | | | | | | |
| from UNC0 | 296.49 | 291.99 | 248.94 | 251.13 | 201.93 | 199.50 | 173.00 | 172.58 |
| $E_1^c$ (Msi) | | | | | | | | |
| of LC | 20.68 | 20.53 | 20.04 | 20.44 | 20.25 | 20.00 | 20.37 | 20.65 |
| E (Msi) | | | | | | | | |
| of UNC0 | 7.75 | 7.64 | 7.47 | 7.52 | 7.57 | 7.53 | 7.74 | 7.82 |
| $\nu_{12}^c$ | --- | 0.362 | | 0.356 | | 0.374 | | 0.383 |
| $F_2^{cu}$ (ksi) | | | | | | | | |
| of TC | --- | 55.31 | --- | 41.44 | --- | --- | --- | 19.02 |
| $E_2^c$ (Msi) | | | | | | | | |
| of TC | --- | 1.53 | --- | 1.41 | --- | --- | --- | 1.18 |
| $\nu_{21}^c$ | | | | | | | | |
| of TC | --- | 0.028 | --- | 0.024 | --- | --- | --- | 0.018 |
| $\nu$ | | | | | | | | |
| of UNC0 | --- | 0.041 | | 0.035 | | 0.030 | | 0.017 |
| $F_{12}^{s5\%strain}$ (ksi) | --- | --- | --- | 13.22 | --- | --- | --- | 5.54 |
| $F_{12}^{s0.2\%}$ (ksi) | --- | 11.29 | --- | 7.76 | --- | --- | --- | 3.31 |
| $G_{12}^s$ (Msi) | --- | 0.86 | --- | 0.68 | --- | --- | --- | 0.31 |
| SBS (ksi) | --- | 21.04 | --- | 17.13 | --- | 11.23 | --- | 8.25 |

Table 13: CFC Material Hexcel IM7 8552 [30] (p.2)

| | | | | | |
|---|---|---|---|---|---|
| **Prepreg Material:** | Hexcel Corporation - Hexcel 8552 IM7 Unidirectional NMS 128/2 Material Specification | | | **Hexcel 8552 IM7 Laminate Properties Summary** | |
| **Fiber** | IM7 unidirectional | **Resin** | Hexcel 8552 | | |
| **Tg(dry)** | 406.43 °F | **Tg(wet)** | 321.41 °F | **Tg METHOD** | DMA (SRM 18-94) |
| **PROCESSING:** | NPS 81228 "M" Cure Cycle | | | | |

| | Lot 1 | Lot 2 | Lot 3 | | |
|---|---|---|---|---|---|
| **Date of fiber manufacture** | 01/26/2007 | 12/25/2006 | 02/05/2007 | **Date of testing** | 1/22/2008 - 3/4/10 |
| **Date of resin manufacture** | 02/28/2007 | 01/24/2007 | 03/01/2007 | **Date of data submittal** | 4/5/2010 |
| **Date of prepreg manufacture** | 02/28/2007 | 01/24/2007 | 03/01/2007 | | |
| **Date of composite manufacture** | 9/2007 to 10/2007 | | | | |

**LAMINATE MECHANICAL PROPERTY SUMMARY**
**Data reported as: Normalized & Measured**
**(Normalized by CPT= 0.0072 inch)**

| | **Layup:** | **25/50/25** | | **10/80/10** | | **50/40/10** | |
|---|---|---|---|---|---|---|---|
| | **Test Condition** | **Normalized** | **Measured** | **Normalized** | **Measured** | **Normalized** | **Measured** |
| **OHT Strength (ksi)** | CTD | 57.75 | 57.28 | 45.95 | 45.63 | 78.75 | 77.97 |
| | RTD | 59.00 | 58.70 | 43.65 | 43.65 | 86.59 | 86.63 |
| | ETW | 66.97 | 66.48 | 38.39 | 38.34 | 114.86 | 113.87 |
| **OHC Strength (ksi)** | RTD | 49.08 | 48.89 | 38.80 | 38.40 | 63.24 | 63.36 |
| | ETW | 35.52 | 35.29 | 25.76 | 25.57 | 46.42 | 46.22 |
| **UNT Strength (ksi)** | CTD | 99.35 | 98.79 | 70.22 | 68.97 | 174.18 | 173.12 |
| | RTD | 104.69 | 104.01 | 67.01 | 67.08 | 175.63 | 176.22 |
| | ETW | 112.46 | 111.50 | 54.17 | 53.44 | 187.43 | 187.30 |
| **Modulus (msi)** | CTD | 8.35 | 8.30 | 5.52 | 5.42 | 13.11 | 13.02 |
| | RTD | 8.39 | 8.34 | 5.22 | 5.23 | 13.15 | 13.20 |
| | ETW | 7.99 | 7.92 | 4.47 | 4.41 | 13.14 | 13.15 |
| **UNC Strength (ksi)** | RTD | 87.05 | 86.95 | 66.44 | 67.49 | 120.84 | 121.06 |
| | ETW | 57.68 | 57.09 | 40.61 | 40.43 | 79.42 | 78.79 |
| **Modulus (msi)** | RTD | 7.86 | 7.86 | 4.90 | 4.98 | 11.90 | 11.93 |
| | ETW | 7.13 | 7.06 | 4.10 | 4.06 | 11.77 | 11.66 |
| **$\nu$UNC** | RTD | --- | 0.334 | --- | 0.587 | --- | 0.423 |
| | ETW | --- | 0.356 | --- | 0.665 | --- | 0.416 |
| **FHT Strength (ksi)** | CTD | 64.02 | 63.52 | 52.25 | 52.05 | 80.70 | 80.53 |
| | RTD | 65.87 | 65.95 | 48.15 | 48.08 | 91.95 | 91.93 |
| | ETW | 70.29 | 69.52 | 42.63 | 42.30 | 101.26 | 100.77 |
| **FHC Strength (ksi)** | RTD | 69.19 | 69.30 | 54.57 | 54.25 | 98.57 | 98.16 |
| | ETW | 51.68 | 51.61 | 41.17 | 40.86 | 72.79 | 72.20 |
| **LSBS Strength (ksi)** | RTD | --- | 12.13 | --- | --- | --- | --- |
| | ETW | --- | 6.99 | --- | --- | --- | --- |
| | | --- | | --- | --- | --- | --- |
| **SSB 2% offset Strength Strength (ksi)** | RTD | 109.89 | 112.98 | 114.02 | 114.20 | 113.90 | 113.93 |
| | ETW | 88.14 | 89.88 | 86.22 | 86.87 | 91.67 | 91.80 |
| **ILT Strength (ksi)** | CTD | --- | 11.96 | --- | --- | --- | --- |
| | RTD | --- | 11.04 | --- | --- | --- | --- |
| | ETW | --- | 6.46 | --- | --- | --- | --- |
| **CAI Strength (ksi)** | RTD | 31.45 | 30.96 | --- | --- | --- | --- |

Table 14: Outputs of Cohesive Element 469208 (this is one of the trigger tip elements), monitoring failure initiation and failure propagation over loading time

| CIFHEX OUTPUT of ELEMENT469208 | | | | | | | | |
|---|---|---|---|---|---|---|---|---|
| shearxy_krit [MPa] 35 | shearxz_krit [MPa] 35 | normal_krit [MPa] 64 | | initiation | propagation | | | |
| ELEMENT 469208 | shearxy_max | shearxz_max | normal | Ye's_criterion | damage value | time | applied disp | increment |
| | [MPa] | [MPa] | [MPa] | [] | [] | [s] | [mm] | [] |
| CENTER | -14,222 | -16,214 | 5,2279 | 0,38639429 | 0,0002 | 2,16 | 0,072 | 9 |
| CENTER | -17,972 | -19,708 | 6,188 | 0,590081573 | 0,0017 | 2,4 | 0,08 | 10 |
| CENTER | -21,0540 | -22,3660 | 6,9162 | 0,781889503 | 0,0050 | 2,64 | 0,088 | 11 |
| CENTER | -22,8120 | -23,6150 | 7,2684 | 0,892943223 | 0,0107 | 2,88 | 0,096 | 12 |
| 4074214 | -25,1920 | -25,2720 | 7,5828 | 1,053475234 | | | | |
| 4074558 | -25,1920 | -25,2720 | 7,5828 | 1,053475234 | | | | |
| CENTER | -24,1760 | -24,3960 | 7,4975 | 0,97669828 | 0,0180 | 3,12 | 0,104 | 13 |
| 4074214 | -24,5010 | -24,0480 | 7,2186 | 0,974848505 | | | | |
| 4074558 | -24,5010 | -24,0480 | 7,2186 | 0,974848505 | | | | |
| CENTER | -24,3130 | -24,0310 | 7,4236 | 0,967422656 | 0,0277 | 3,36 | 0,112 | 14 |
| CENTER | -24,3780 | -23,6870 | 7,3910 | 0,956488358 | 0,0388 | 3,6 | 0,12 | 15 |
| CENTER | -24,3900 | -23,3610 | 7,4007 | 0,944480585 | 0,0508 | 3,84 | 0,128 | 16 |
| CENTER | -24,3580 | -23,0500 | 7,4511 | 0,931607204 | 0,0637 | 4,08 | 0,136 | 17 |
| CENTER | -24,2640 | -22,7690 | 7,5484 | 0,917722203 | 0,0775 | 4,32 | 0,144 | 18 |
| CENTER | -24,1540 | -22,4760 | 7,6550 | 0,902948274 | 0,0921 | 4,56 | 0,152 | 19 |
| CENTER | -24,0320 | -22,1700 | 7,7645 | 0,887409168 | 0,1075 | 4,8 | 0,16 | 20 |
| CENTER | -23,8780 | -21,8560 | 7,8742 | 0,870520004 | 0,1242 | 5,04 | 0,168 | 21 |
| CENTER | -23,6320 | -21,4560 | 8,0471 | 0,847508595 | 0,1471 | 5,28 | 0,176 | 22 |
| CENTER | -23,4070 | -21,0840 | 8,1570 | 0,826385283 | 0,1680 | 5,52 | 0,184 | 23 |
| CENTER | -23,1480 | -20,7230 | 8,2566 | 0,804621078 | 0,1896 | 5,76 | 0,192 | 24 |
| CENTER | -22,8470 | -20,2950 | 8,2792 | 0,7790795 | 0,2151 | 6 | 0,2 | 25 |
| CENTER | -22,4650 | -19,6890 | 8,1461 | 0,744635972 | 0,2497 | 6,24 | 0,208 | 26 |
| CENTER | -21,9050 | -18,8480 | 7,8767 | 0,69684187 | 0,2978 | 6,48 | 0,216 | 27 |
| CENTER | -21,0780 | -17,7530 | 7,5230 | 0,633777344 | 0,3613 | 6,72 | 0,224 | 28 |
| CENTER | -19,6610 | -16,1210 | 7,0598 | 0,539875556 | 0,4557 | 6,96 | 0,232 | 29 |
| CENTER | -18,1040 | -14,5500 | 6,6836 | 0,451279205 | 0,5448 | 7,2 | 0,24 | 30 |
| CENTER | -16,5220 | -13,0860 | 6,3497 | 0,372471904 | 0,6239 | 7,44 | 0,248 | 31 |
| CENTER | -14,9190 | -11,6840 | 6,0103 | 0,301955931 | 0,6947 | 7,68 | 0,256 | 32 |
| CENTER | -13,2590 | -10,2880 | 5,6270 | 0,237643746 | 0,7594 | 7,92 | 0,264 | 33 |
| CENTER | -11,4980 | -8,8486 | 5,1675 | 0,178357444 | 0,8190 | 8,16 | 0,272 | 34 |
| CENTER | -9,5774 | -7,3167 | 4,5885 | 0,123720373 | 0,8740 | 8,4 | 0,28 | 35 |
| CENTER | -7,1409 | -5,4149 | 3,7250 | 0,068949722 | 0,9292 | 8,64 | 0,288 | 36 |
| CENTER | -3,5033 | -2,6395 | 2,0883 | 0,016770877 | 0,9819 | 8,88 | 0,296 | 37 |
| CENTER | 0,0000 | 0,0000 | 0,0000 | 0 | 1,0000 | 9,12 | 0,304 | 38 |

## C.1. Parameter study on the MCOHE-card

In order to better understand the behavior of the CZEs, a parameter study of their material input has been executed at the CLS-model.
Primarily, the change of parameters is done to see, whether a change of the material input can raise the failure load of the CLS-component from $F_{sim,crit}$=30kN to the level of $F_{test,crit}$=55kN.

In a first step of parameter variation, the critical energy release rates $G_{CI}$ and $G_{CII}$ stay unmodified (values according to [35]). The shear-normal ratios $\beta_1$ and $\beta_2$ remain fix as well. The initial CZE-stiffness $K_{el}$ and the critical traction $\tau_{max}$ of the CZE have been varied as can be seen on figure C.1. The red colored curve represents the original bilinear material law for normal loading direction (s. figure 3.3) as it has been utilized at the presented CLS-model.
As $\beta_1$ and $\beta_2$ remain unchanged the material-law for pure shear loading changes simultaneously to the modification of the material-law for pure normal loading.

In a second step the same parameter modifications have been chosen, with a changed energy release rate (s. figure C.2).

In order to summarize the results of the executed parameter study, the failure loads of the CLS-model have been plotted next to their corresponding material curves of the CZEs.

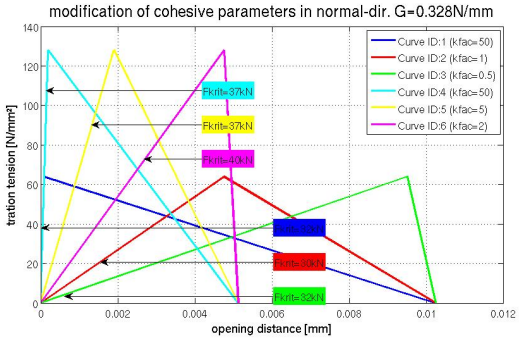


Figure C.1: Variation of CZE-parameter with $G_C I$=0,328N/mm

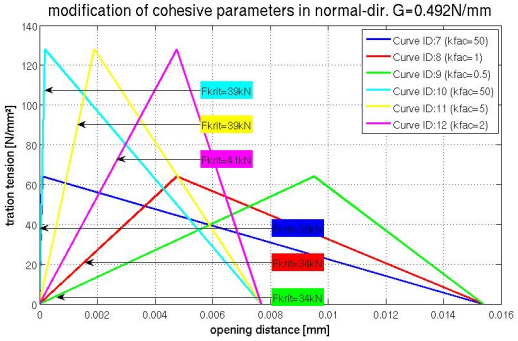


Figure C.2: Variation of CZE-parameter with $G_C I$=0,492N/mm

The result of the parameter study proves, that a change of cohesive stiffness has just small influence on the failure load. This is expected, because the CZE-stiffness has

rather numerical influence on the CLS-model according to [25]. The increase of the critical traction as well as the increase of the energy release rate raises the level of the critical failure load $F_{sim,crit}$. If an increase of the failure load is desired, the changing of the energy release rate is the recommended parameter. On the one hand, it comparably results in a larger effect and on the other hand, the changing of the critical traction can be used to compensate the disturbance of mesh size effects pursuant [25].
Additionally the ESA states in [9], that „the shear strength of adhesively bonded structural joints can be better expressed by the strain energy to failure per unit bond area, than by any of the individual properties such as peak shear stress“.

## C.2. „Breaking Glue“-model

A last CLS-model is introduced in this subsection. In comparison to all the other models based on the CZM, this model proposes contact constrains to represent the adhesive layer. The „Breaking Glue“-model is based on the Breaking Glue algorithm of MSC Nastran presented in subsection 2.2.3. The model will start to cut a contact constraint, if the involved stress criterion according to equation (5) is satisfied.
The used contact method is the „Node-to-segment“ approach in which the contact is modeled by multi-point-constraints (MPCs). The visualized contact constraints are depicted in figure (4.4). Analog to the results of the CZM-models, the results of the „Breaking Glue“-model are presented in figure C.3.

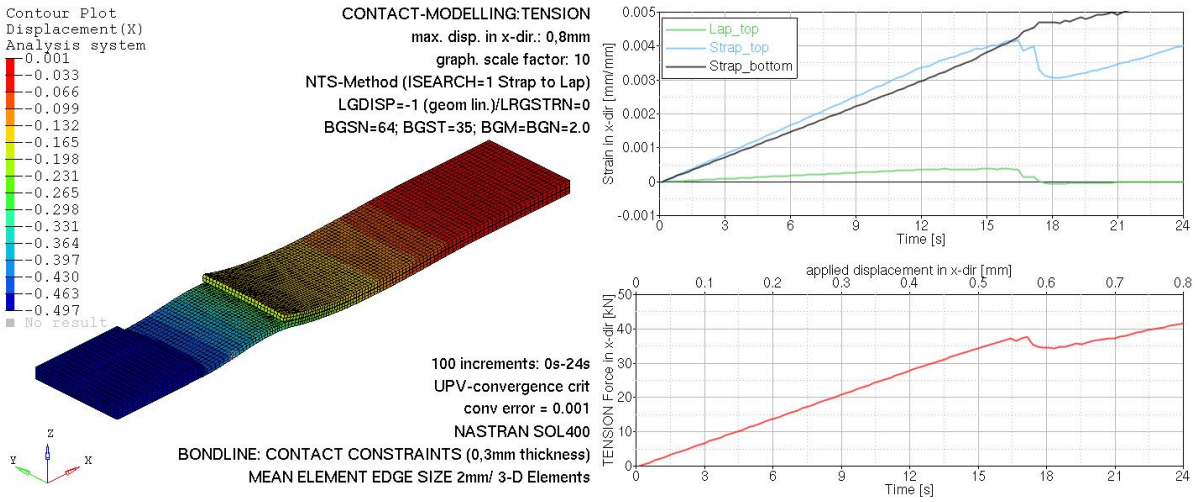


Figure C.3: Simulation of the CLS-model using the breaking glue algorithm. The state of deformation is kept at an applied tensional displacement of 0,5mm

The failure occurs at a load level of $F_{sim,crit}$=37kN which is a higher level than it is reached by the CZM-models. In addition, the crack growth is much faster and resembles more to the test results. Furthermore, also the breaking glue method does not achieve an initial failure of 55kN and fails too early.

At this position it has to be mentioned that several questions went along with the simulation of the „Breaking Glue"-model. In the direct contact to the MSC customer support some of these questions could be answered.
Hence, the most important issues and recommendations are shortly summarized:

- The thickness of the adhesive layer should not be vacant. If the contact constraints of the Node-to-Segment approach are created bridging the gap of the adhesive layer, the direction in which the contact is created (ISEARCH=1)) significantly influences the analysis results. Thus, there should be some elements created to represent the adhesive layer

- The Segment-to-Segment contact approach offers a more continual contact modeling than the Node-to-Segment approach. Unfortunately it is not valid for the use of the Breaking Glue approach

## C.3. Convergence control

To verify the nonlinear analysis a check of convergence has been executed for one CZM-model and for the breaking glue model. This check is explained at the example of the CZM-model with the model identification „3. Solid" according to 4.7.
The load-displacement-criterion (UPV) is recommended for mechanical analysis as the most suitable convergence criterion corresponding to [1]. Even the virtual work convergence criterion (WA) is testified on the models. In the course of the study of convergence and according to [1] it is detected that the number of iterations is a fundamental factor for the achievement of convergence. Figure C.4 presents the analysis of the specified CZM-model using different convergence criteria and different incrementation schemes. The convergence error remains $ERR_{conv}$ for all the shown curves on the same level of $ERR_{conv}$=0,1 (this is the recommended convergence error along MSC Nastran). It is apparent that the load-displacement-curves approach each other using a higher number of iterations during the simulation. Specifying that at least 2 iterations have to be executed

in each load increment, the figure C.4 illustrates that the convergence of the present CLS model is achieved at an iteration number of round about 3600.

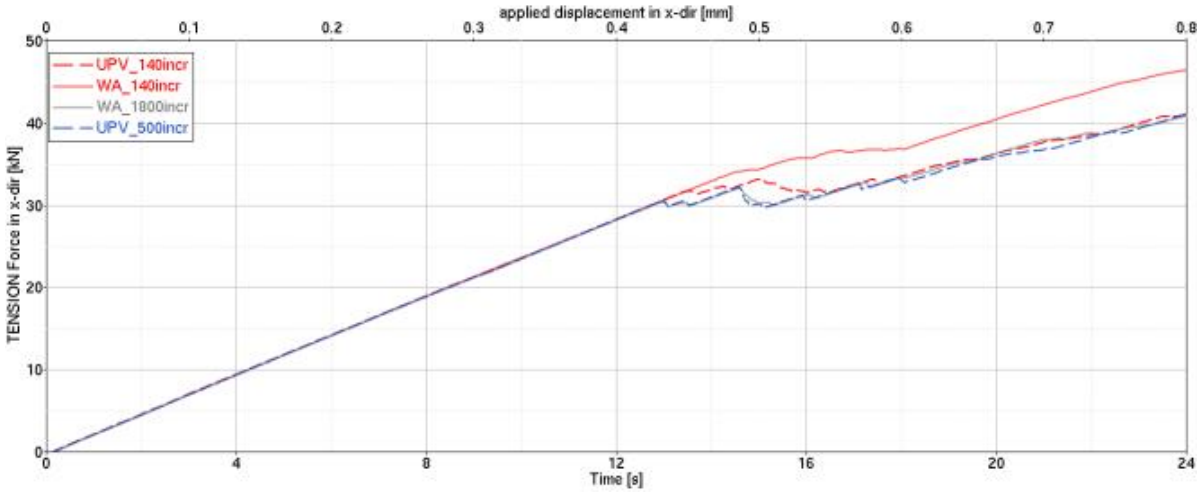


Figure C.4: Study of convergence; Simulation of the CZM-CLS-model number 3. according to 4.7 ($l_{E,Composite}$=8,3mm; $l_{CZE}$=4,15mm)

For the tested virtual work criterion (WA), the solver managed to calculate every increment exactly using two iterations per increment. The virtual work criterion (WA) contemplates the analysis globally. This is most possibly the reason, why the solver does not run into convergence problems at all. It does not respect the local stiffness changes induced by the damgage of the CZEs as the load-displacement-criterion (UPV) does. Applying the same convergence error $ERR_{conv,UPV}$=0,1, the UPV-criterion needs many more iterations during specific increments in which the nonlinearity of the model particularly is high. Thus, the iteration number per increment for the UPV-criterion is dependent on the local nonlinearity of the model which is visualized by the load-displacement-curve. While the CZEs are damaging the solver, hence, needs a greater amount of iterations than during the period of linear-elastic deformation.

A reduction of the convergence error to $ERR_{conv,UPV}$=0,01 in CLS-CZM-model-analysis leads to problems solving the constitutive equations. In the load increment, where the CZEs start to damage at an applied displacement of about $u$=0,42mm the solver of MSC Nastran does not find a converged solution of the constitutive equations in between a specified maximum limit of iterations. This maximum amount of iterations per increment is specified to $n_{iterations/incr}$=50.

The breaking glue model in contrary does not deal with material nonlinearities, since no nonlinear material is entered therein to model the adhesive behavior. Thus, a convergence error of $ERR_{conv,UPV}$=0,001 can be followed. If a node separates during the breaking glue analysis, the present iteration is not evaluated in the compliance of the maximum iteration number.

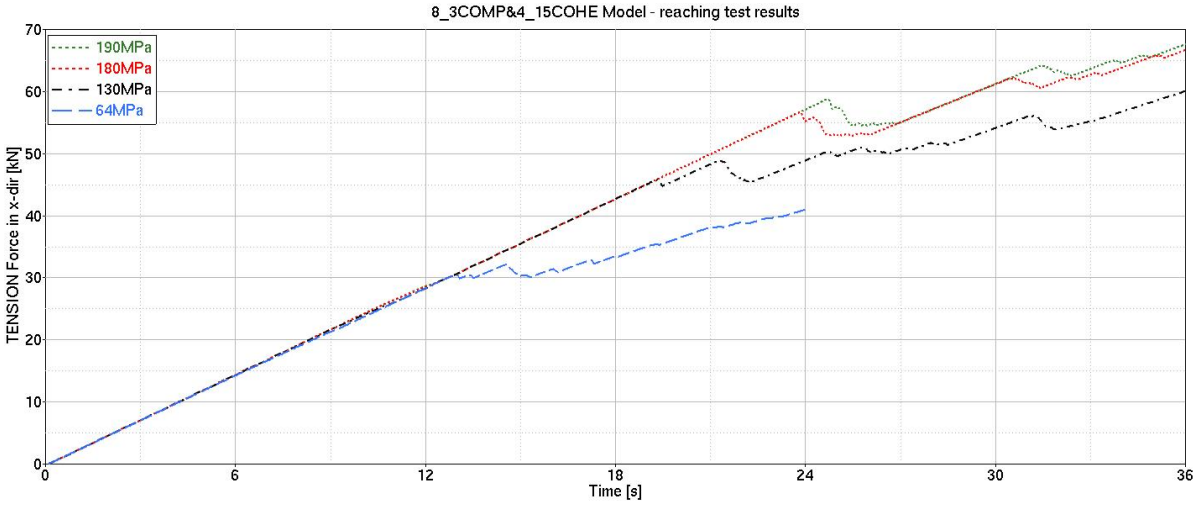


Figure C.5: Variation of the critical tension in cohesive zone elements, without changing the shear-normal-ratios ($\beta_1$, $\beta_2$) for the coarse element mesh of composite and cohesive elements (8,33mm/4,15mm)

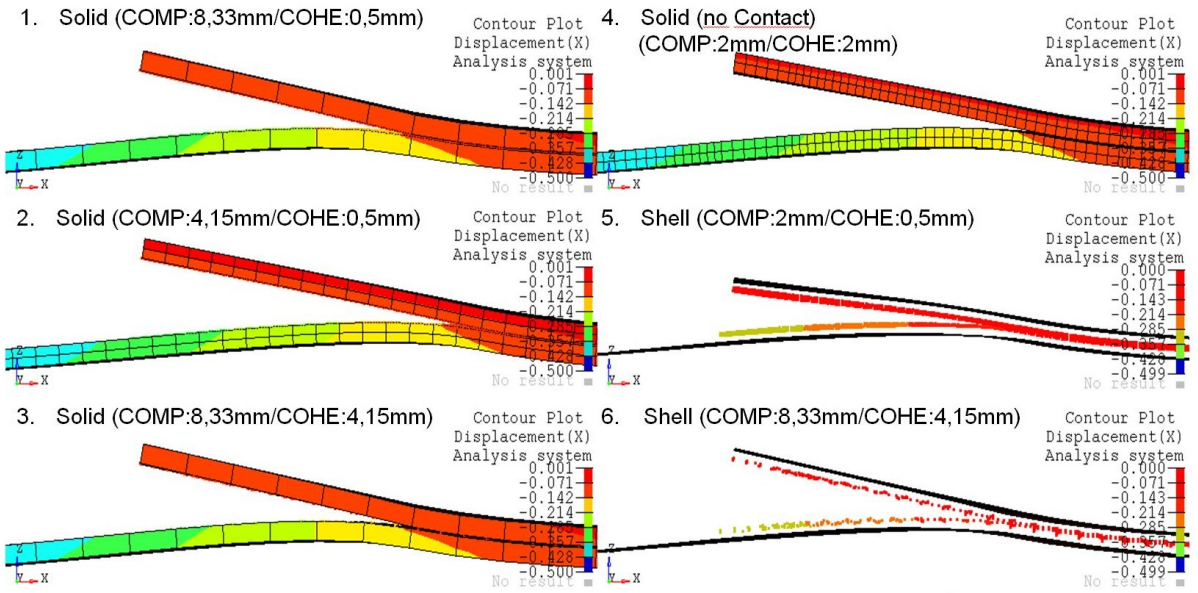


Figure C.6: Visualisation of delamination progress comparing the different studied meshes on the CLS-CZM-model (present applied displacement $u_x$=0,5mm)

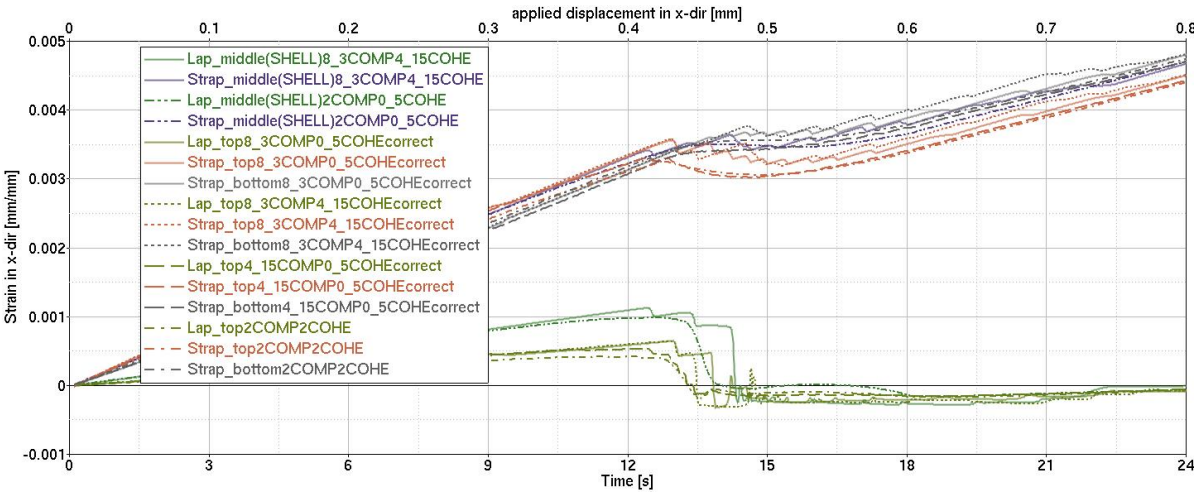


Figure C.7: Strain comparison of different CLS-CZM-models

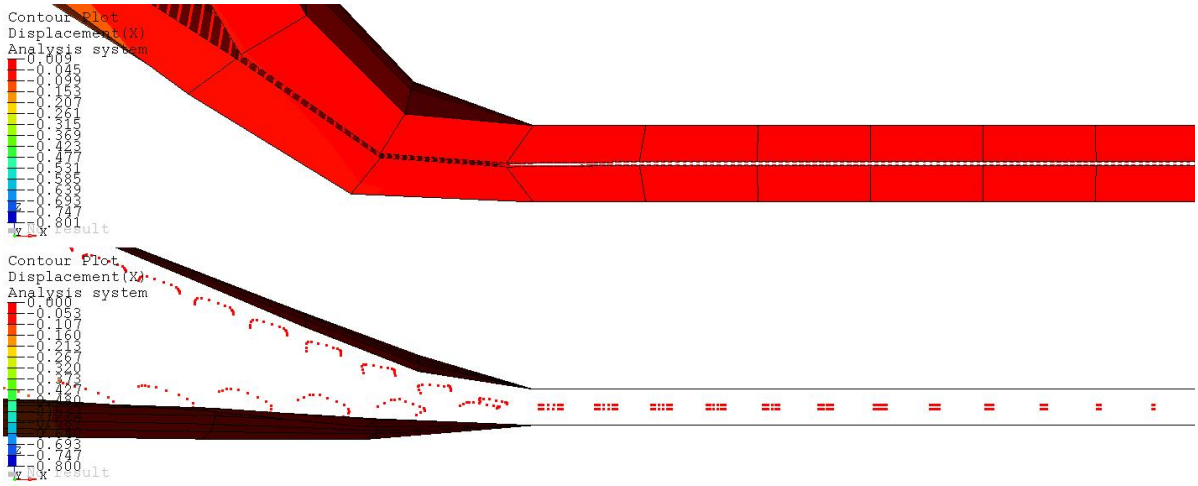


Figure C.8: Visualisation of clamping difference of the solid (top) and the shell model (bottom) on the lap-strap clamping side

# D. Appendix for critical Details

## D.1. T-Pull

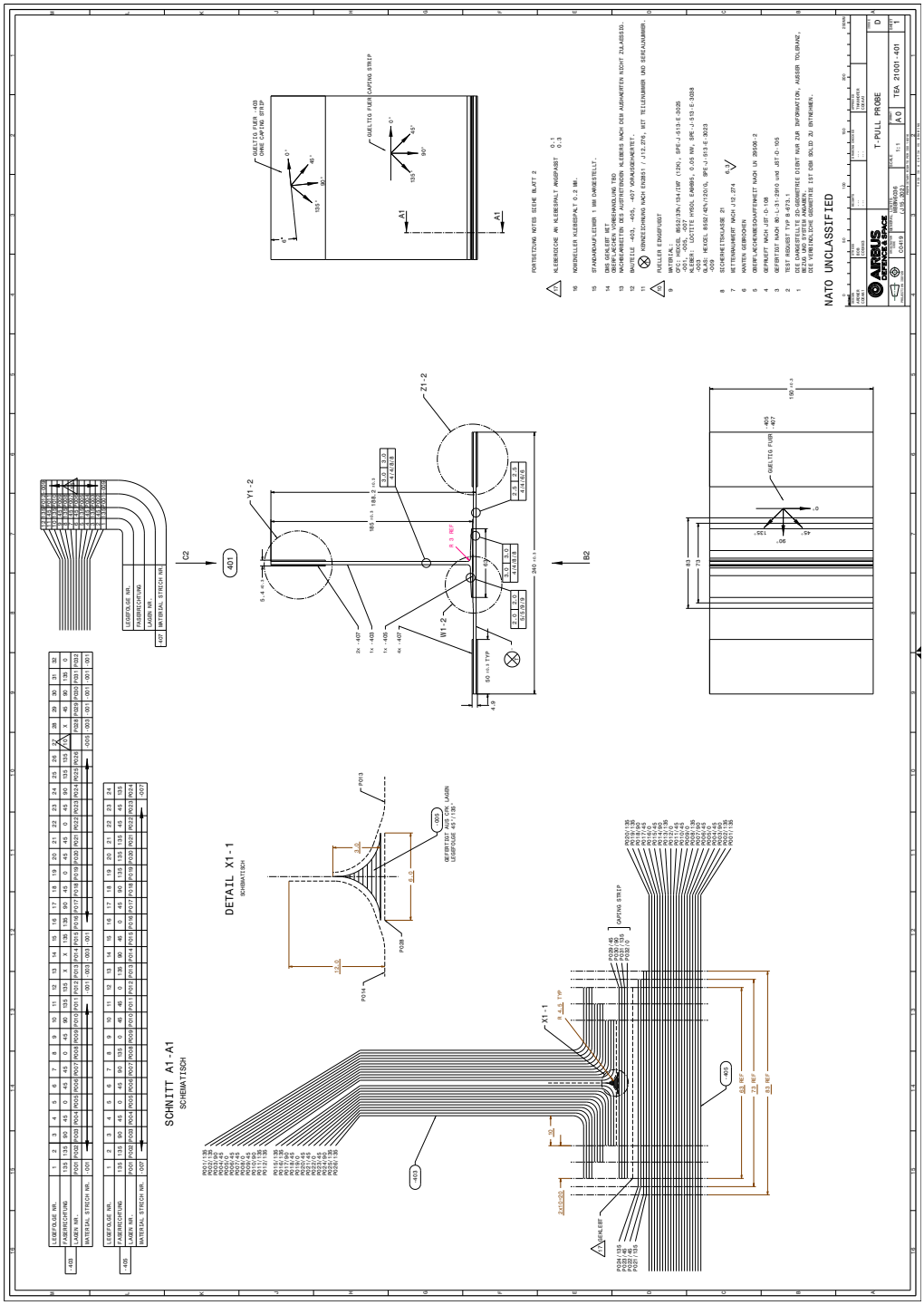


Figure D.1: Geometry and stacking of T-Pull-specimen

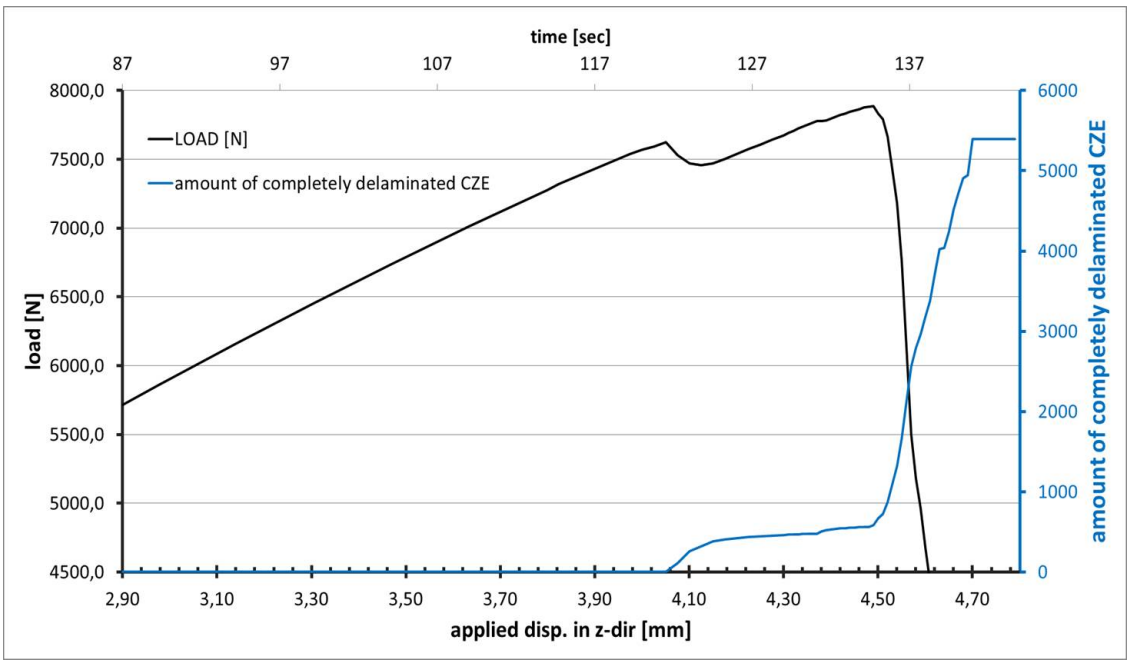


Figure D.2: Number of CZEs delamination over the simulation time and over the applied displacement (the state of simulation is clarified by the load-displacement-curve)

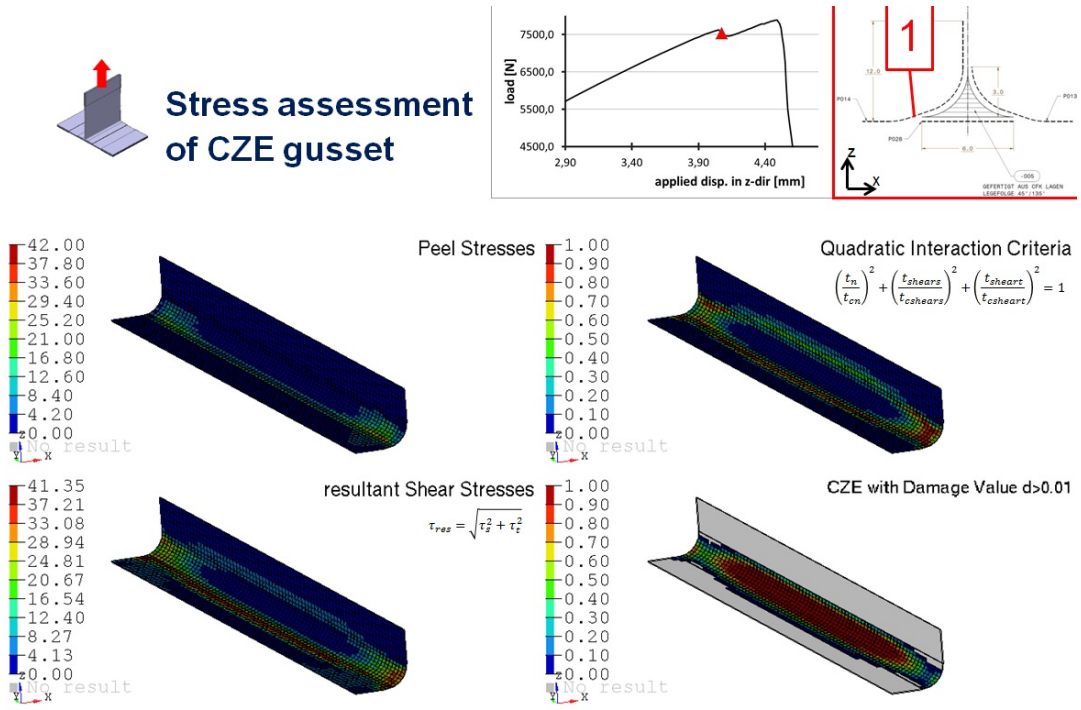


Figure D.3: Stresses in adhesive layer 1 above the gusset at an applied displacement of $w_{applied} = 4,08mm$

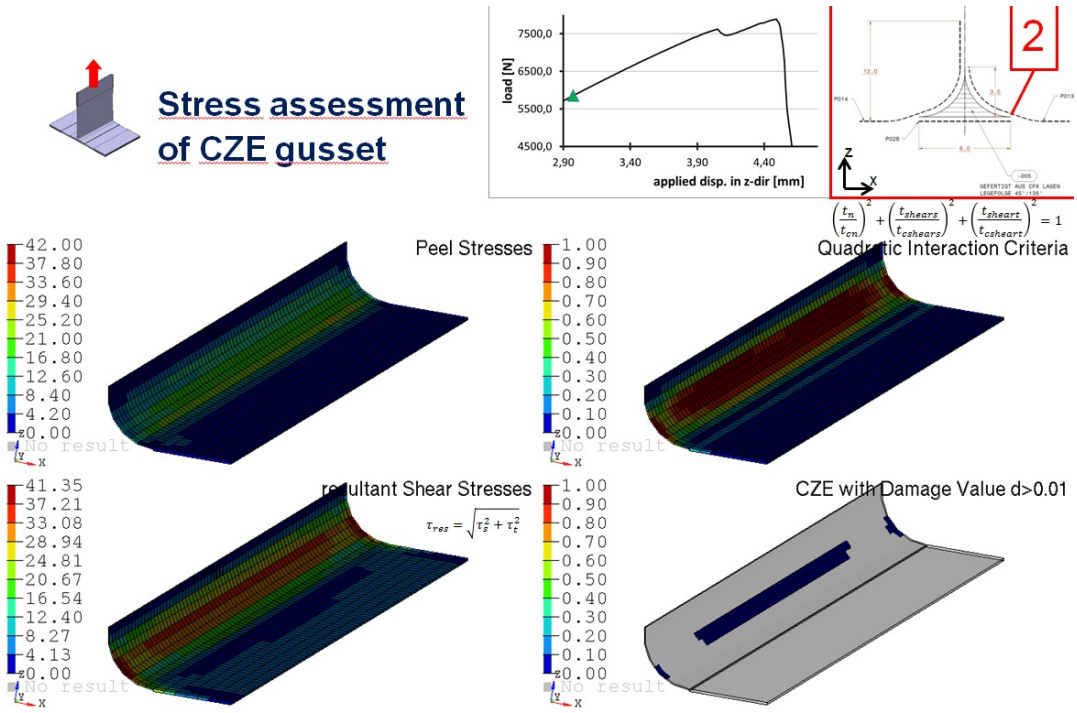


Figure D.4: Stresses in adhesive layer 2 above the gusset at an applied displacement of $w_{applied} = 2,97\,mm$

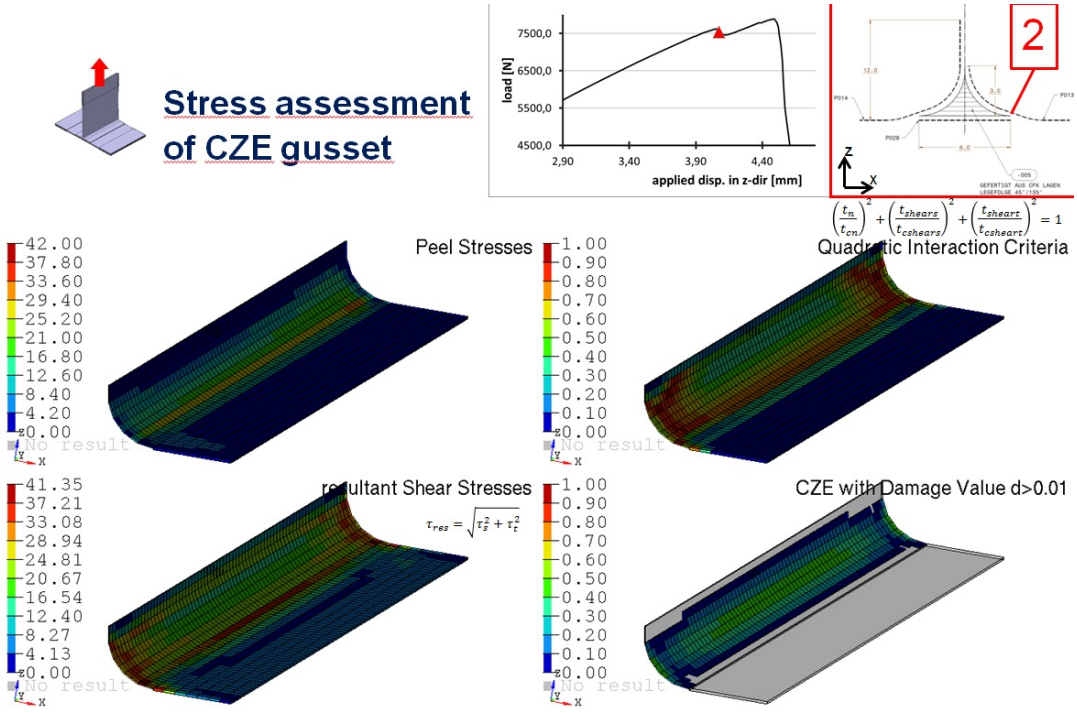


Figure D.5: Stresses in adhesive layer 2 above the gusset at an applied displacement of $w_{applied} = 4,08\,mm$

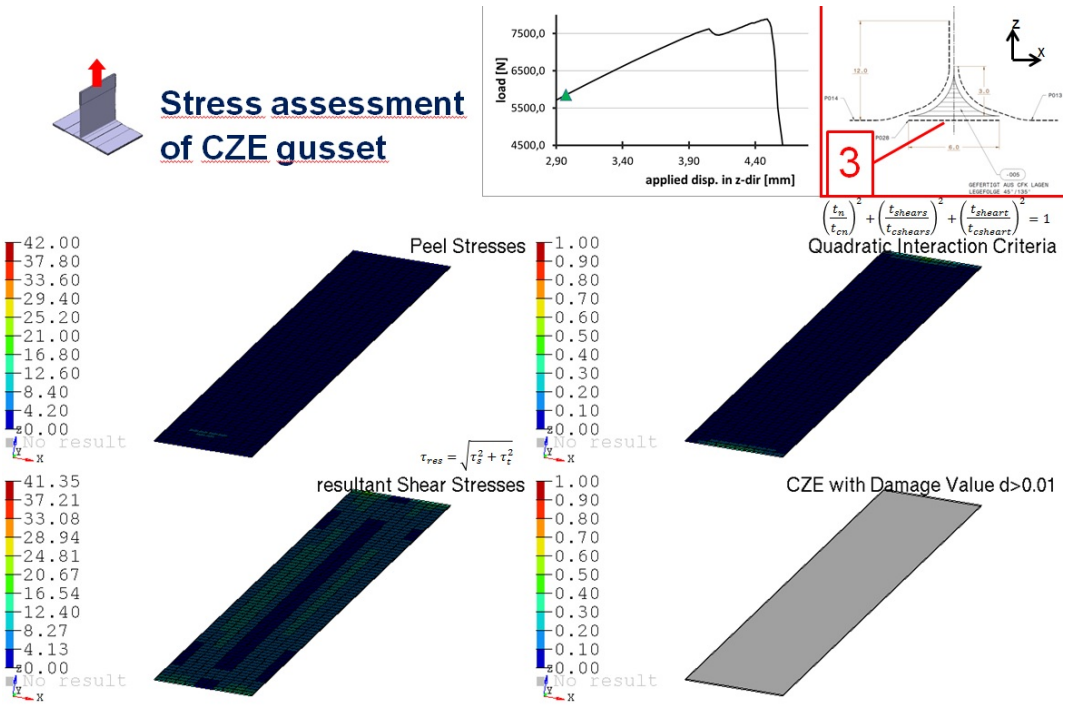


Figure D.6: Stresses in adhesive layer 3 above the gusset at an applied displacement of $w_{applied} = 2,97mm$

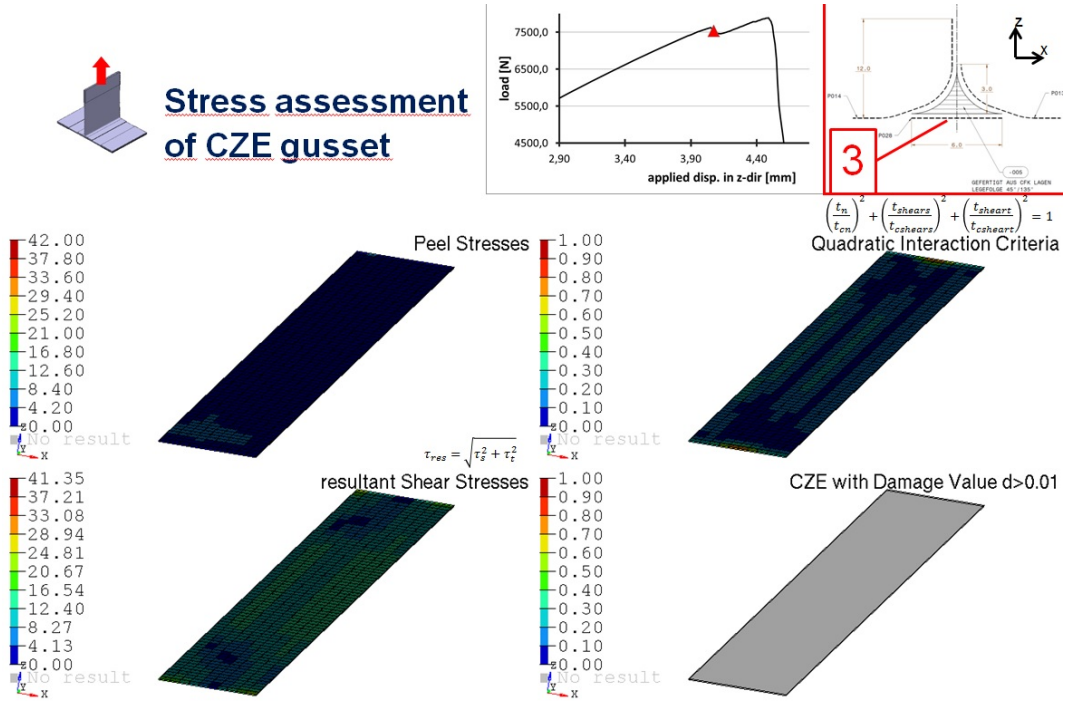


Figure D.7: Stresses in adhesive layer 3 above the gusset at an applied displacement of $w_{applied} = 4,08mm$

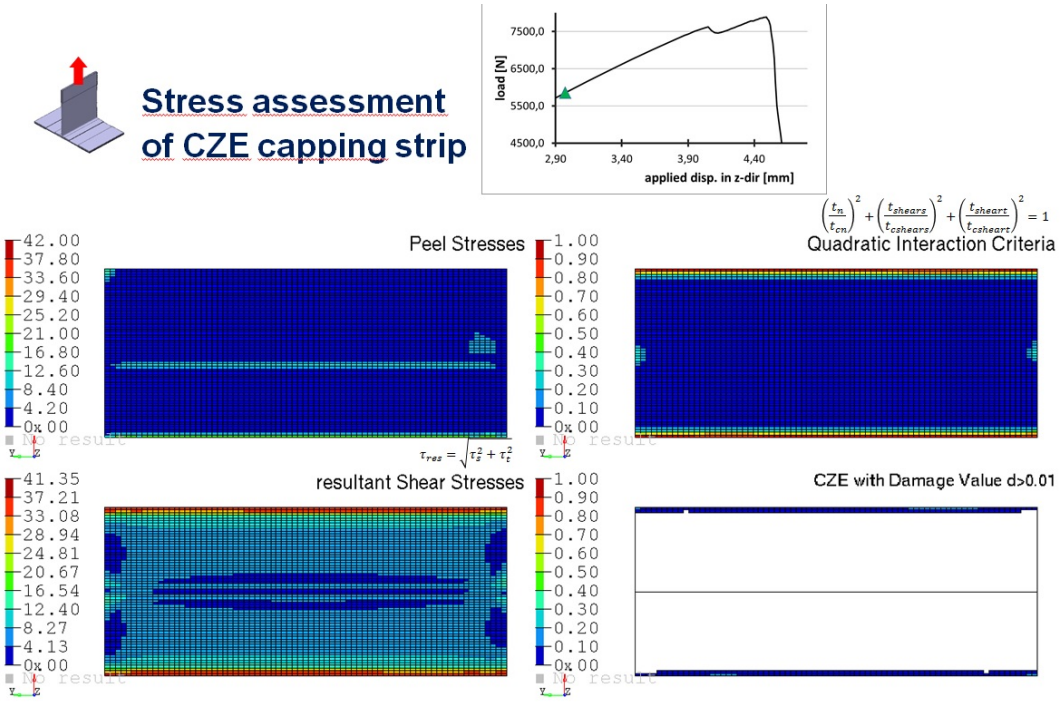


Figure D.8: Stresses in adhesive layer underneath the capping strip at an applied displacement of $w_{applied} = 2,97mm$

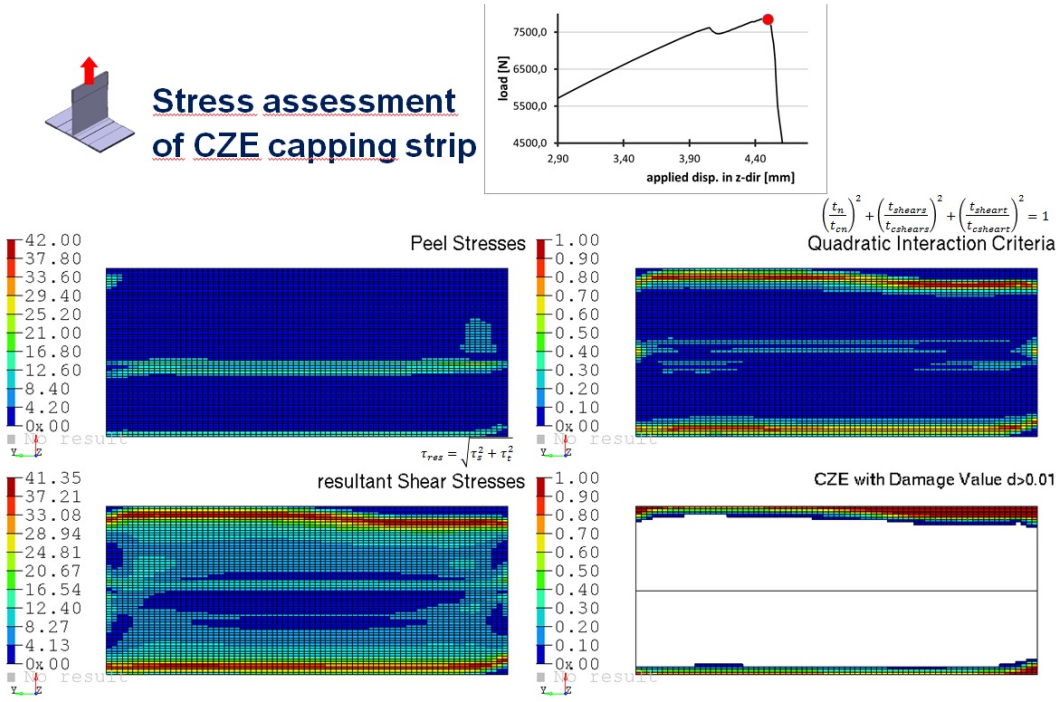


Figure D.9: Stresses in adhesive layer underneath the capping strip at an applied displacement of $w_{applied} = 4,5mm$

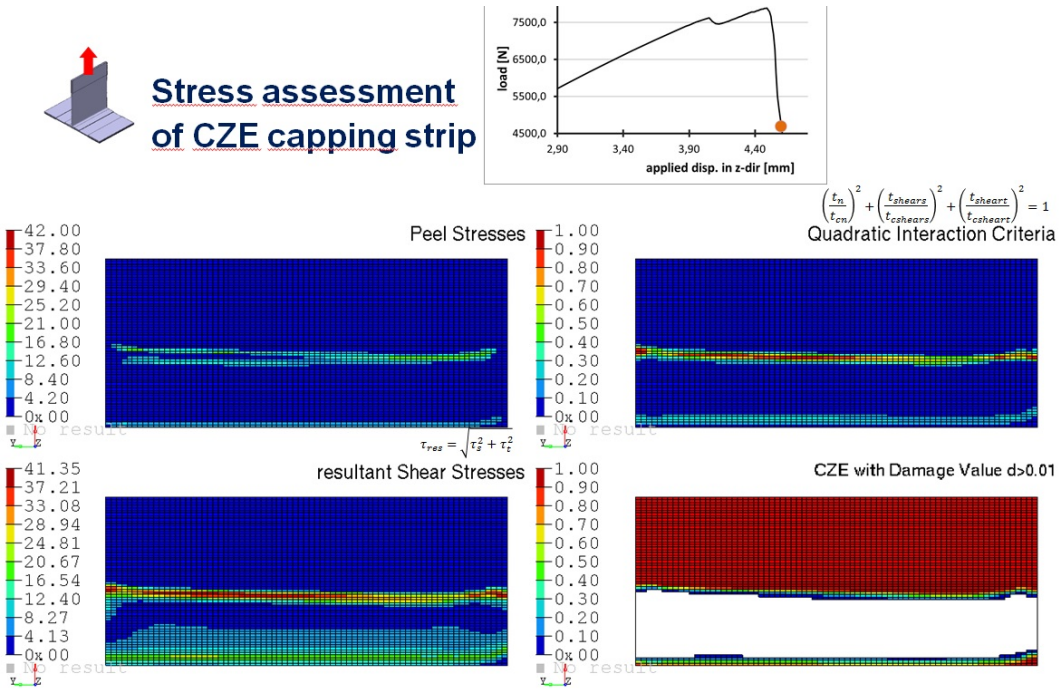


Figure D.10: Stresses in adhesive layer underneath the capping strip at an applied displacement of $w_{applied} = 4,6mm$

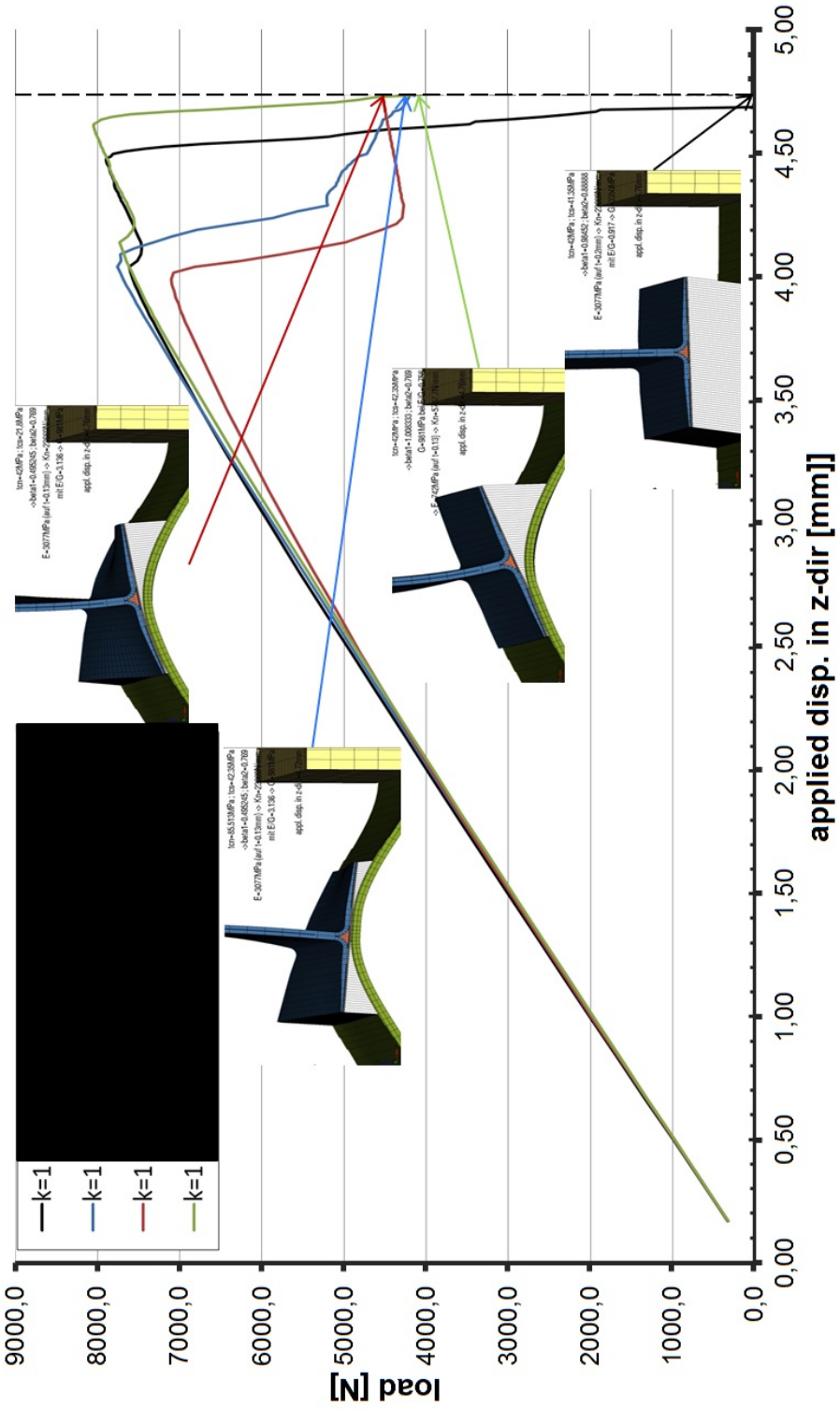


Figure D.11: Variation of MCOHE-cards for the CZEs due to a variation of input data out of different material tests (out of six MCOHE material-values to specify, the energy release rates GI, GII and GIII remain the same for all four studied MCOHE-cards; the remaining four MCOHE parameters are varied along the legend; the black colored curve is the standard load-displacement-curve, which has been presented in the T-Pull-section)

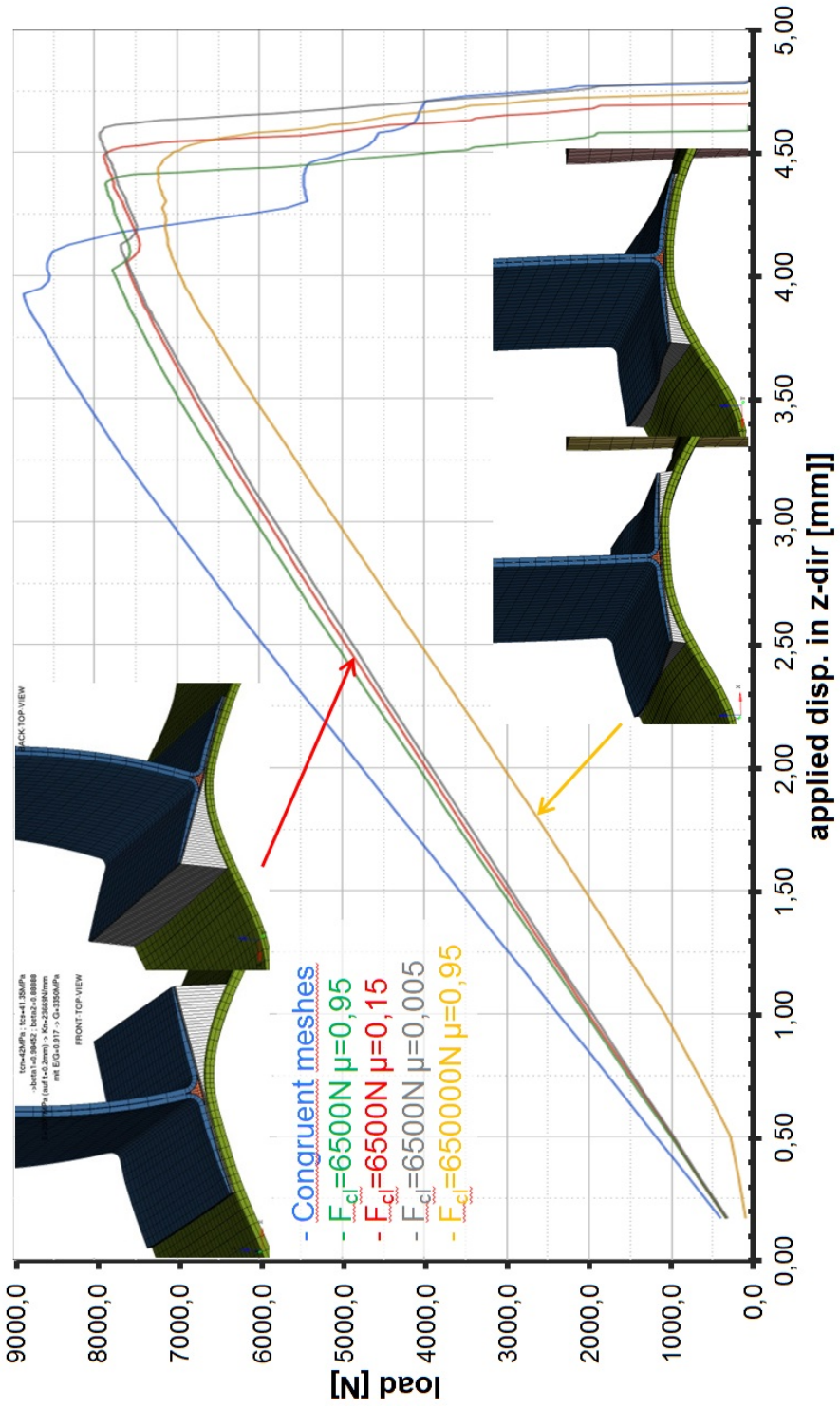


Figure D.12: Sensitivity of the T-Pull-model on a variation of frictional horizontal clamping conditions (clamping force $F_{cl}$ and friction coefficient $\mu$); the red colored curve is the standard load-displacement-curve, which has been presented in the T-Pull-section. It has the proposed friction coefficient $\mu$=0,15, which is an averaged value along [39] between steel and CFC-laminates, and the proposed clamping force $F_{cl}$=6500N along the test definition

## D.2. T-Tension

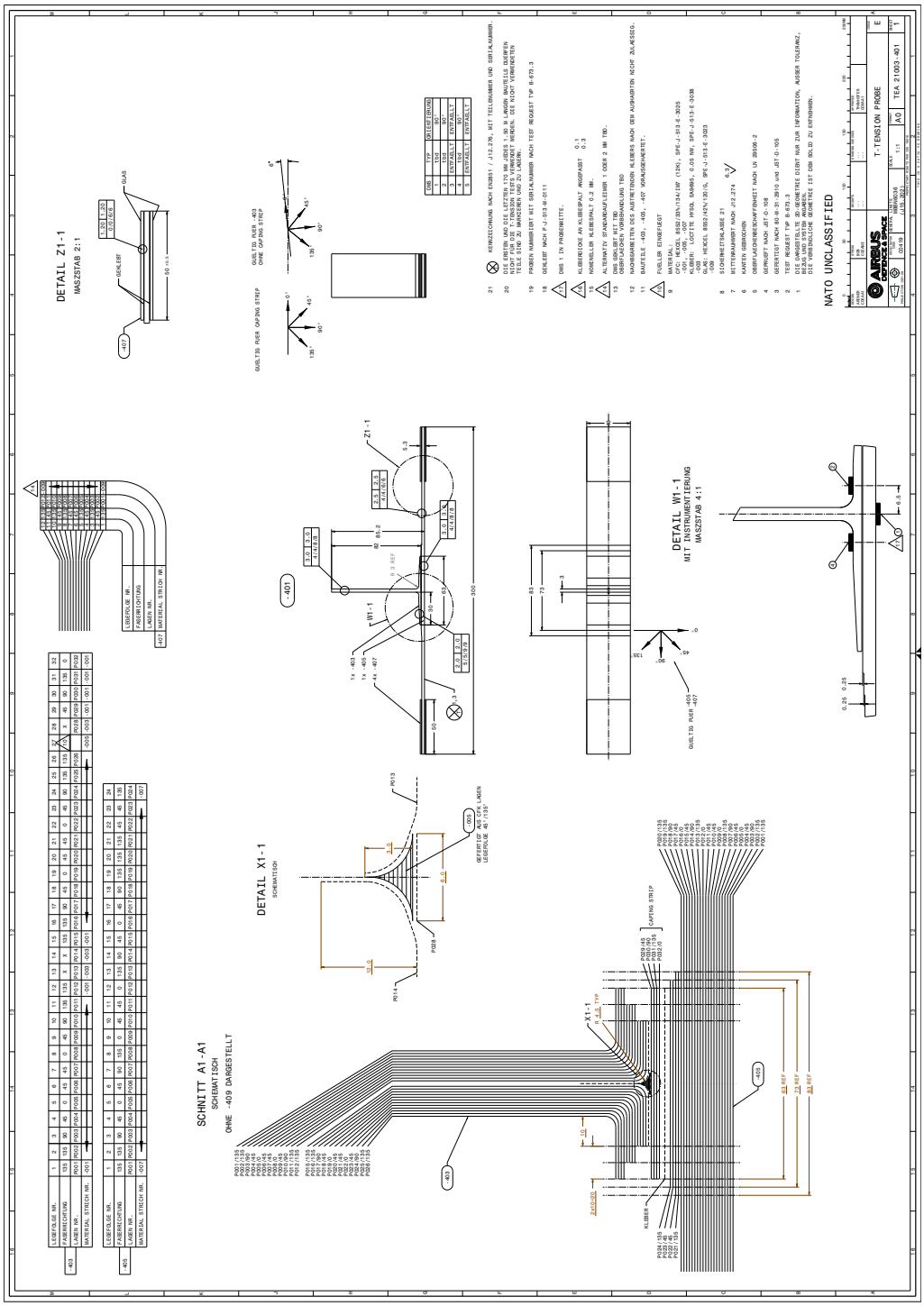

Figure D.13: Geometry and stacking of T-Tension-specimen

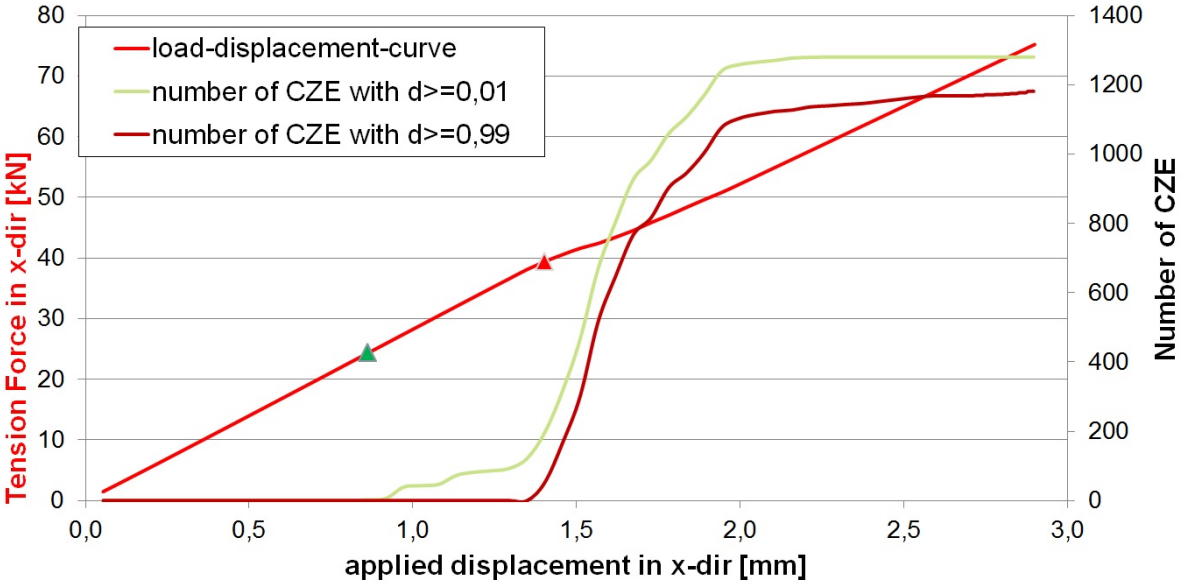


Figure D.14: Number of CZEs, which fail ($d \geq 0{,}01$) and number of CZEs, which start to delaminate ($d \geq 0{,}99$) plotted over the applied displacement (the state of simulation is clarified by the load-displacement-curve)

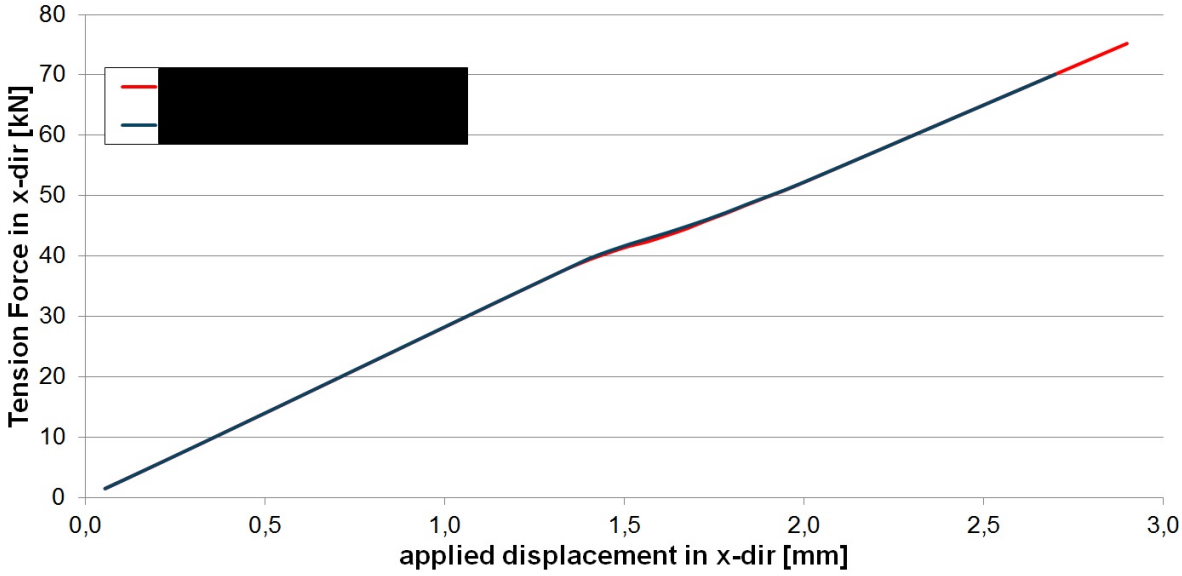


Figure D.15: Variation of MCOHE-cards for the CZEs due to a variation of input data out of different material tests (out of six MCOHE material-values to specify, the energy release rates GI, GII and GIII remain the same for the two studied MCOHE-cards; the remaining four MCOHE parameters are varied along the legend; the dark blue colored curve is the standard load-displacement-curve, which has been presented in the T-Tension-section)

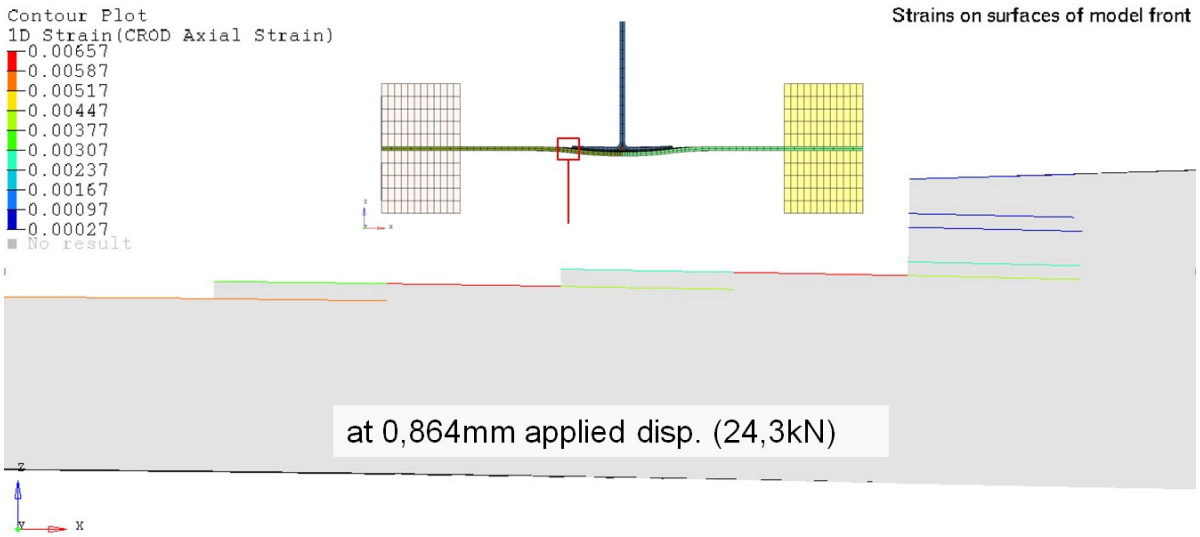


Figure D.16: Strains at the upper surface at the position of the stepped local thickeness increase at an applied displacement of 0,864mm, which corresponds to 24,3kN tensional loading

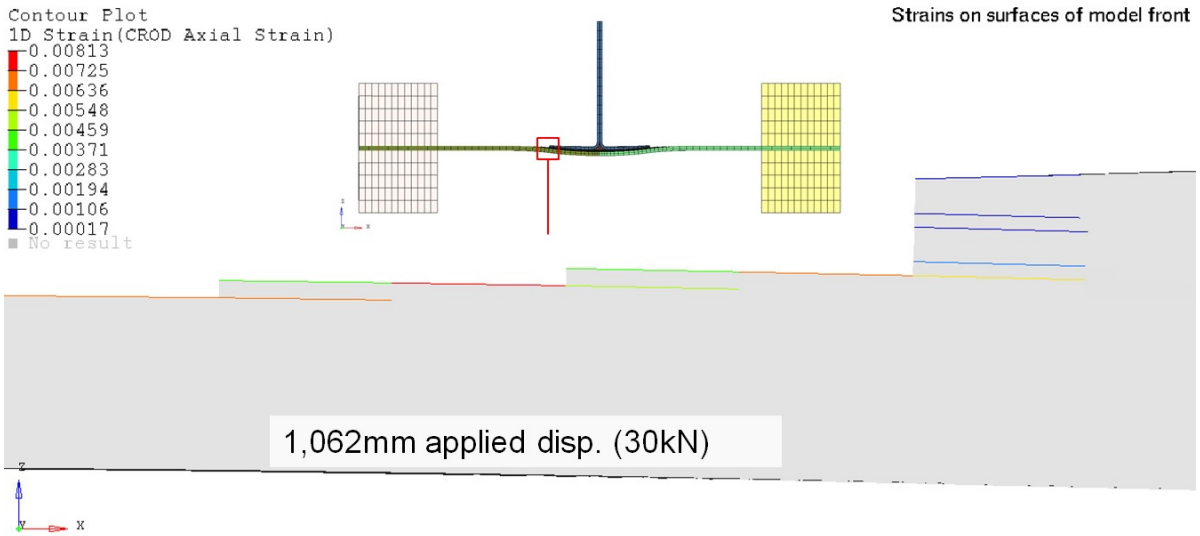


Figure D.17: Strains at the upper surface at the position of the stepped local thickeness increase at an applied displacement of 1,062mm, which corresponds to 30kN tensional loading

## D.3. T-Shear

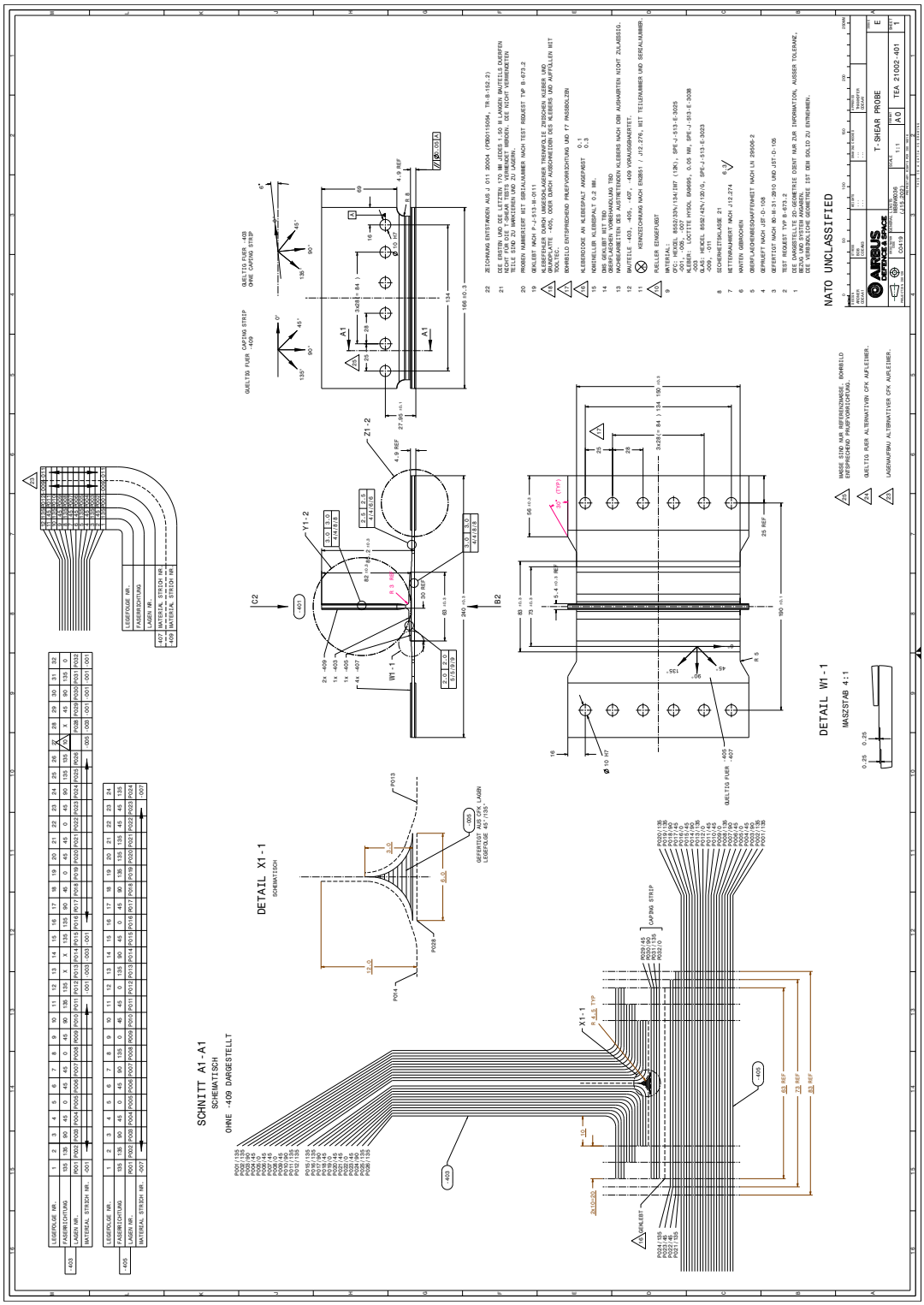


Figure D.18: Geometry and stacking of T-Shear-specimen

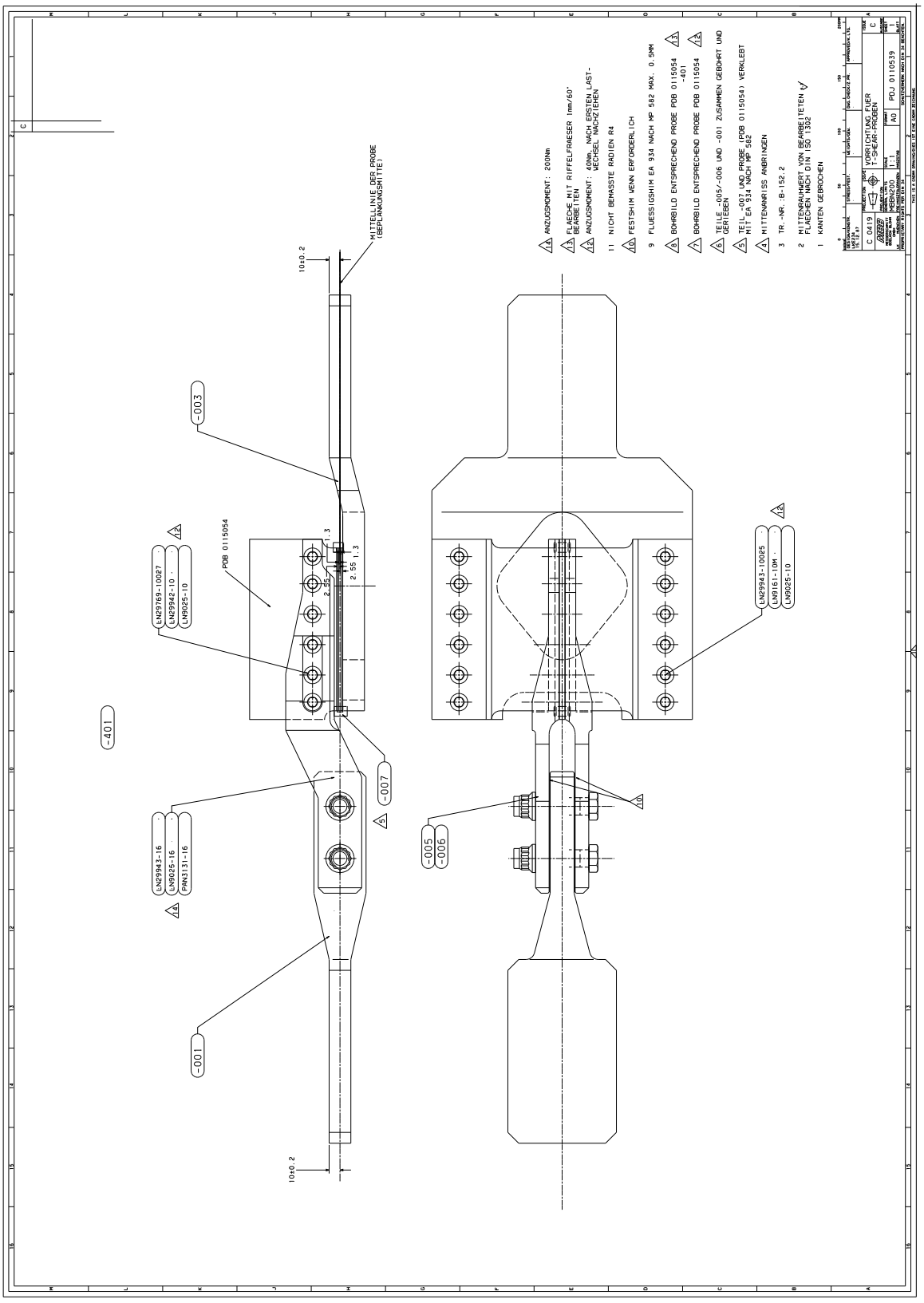


Figure D.19: Clamped T-Shear-specimen

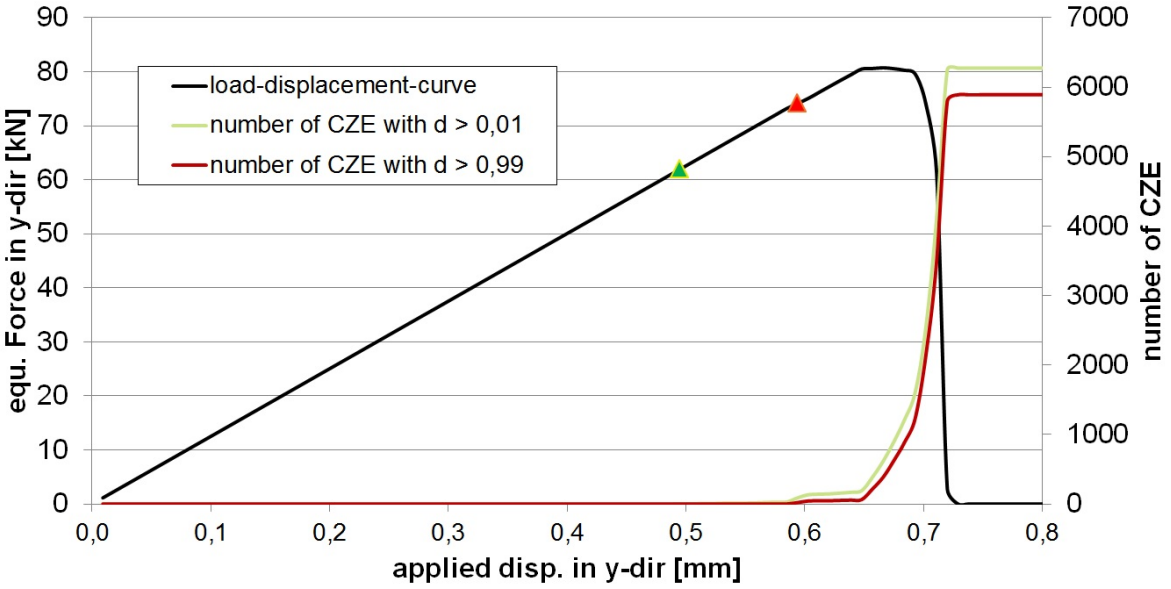


Figure D.20: Number of CZEs, which fail ($d \geq 0{,}01$) and number of CZEs, which start to delaminate ($d \geq 0{,}99$) plotted over the applied displacement (the state of simulation is clarified by the load-displacement-curve)

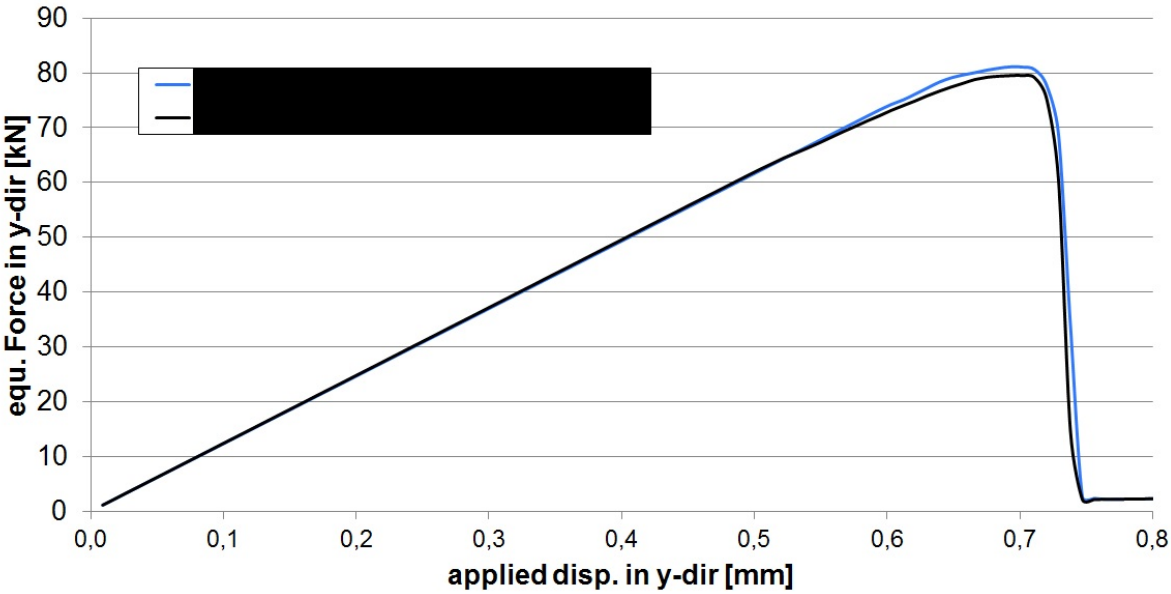


Figure D.21: Variation of MCOHE-cards for the CZEs due to a variation of input data out of different material tests (out of six MCOHE material-values to specify, the energy release rates GI, GII and GIII remain the same for the two studied MCOHE-cards; the remaining four MCOHE parameters are varied along the legend; the black colored curve is the standard load-displacement-curve, which has been presented in the T-Shear-section)

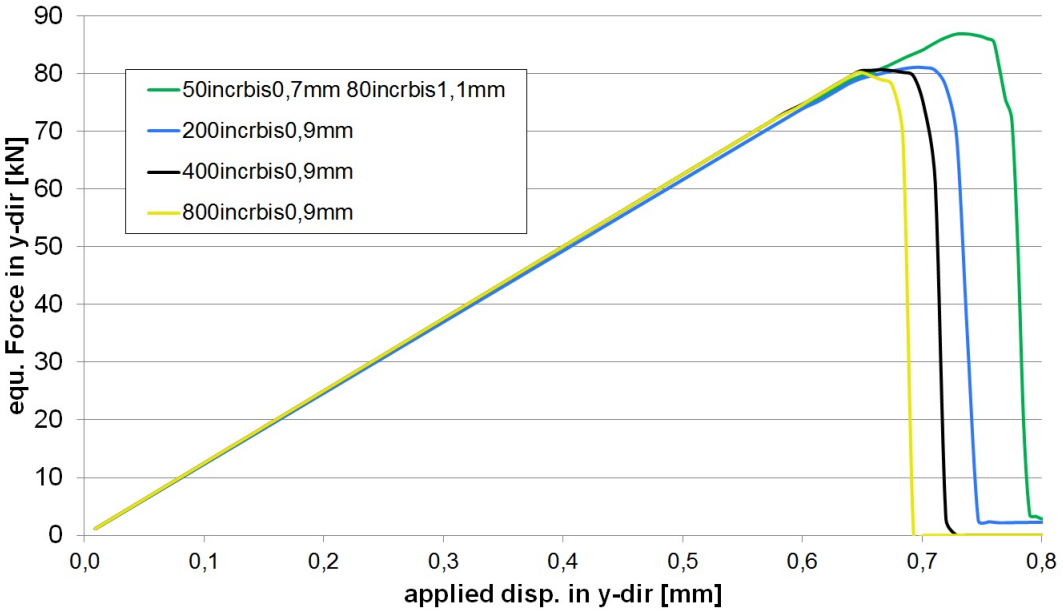


Figure D.22: Convergence control of the T-Shear-simulation; an incrementation of more than 200 increments does not influence the quantity of failure initiation and delamination initiation anymore; qualitative a higher incrementation than 200 increments reduces the time of delamination, means at a full converged solution the delamination occurs very abrupt

Hochschule für Angewandte Wissenschaften Hamburg
*Hamburg University of Applied Sciences*

## Erklärung zur selbstständigen Bearbeitung einer Abschlussarbeit

Gemäß der Allgemeinen Prüfungs- und Studienordnung ist zusammen mit der Abschlussarbeit eine schriftliche Erklärung abzugeben, in der der Studierende bestätigt, dass die Abschlussarbeit „– bei einer Gruppenarbeit die entsprechend gekennzeichneten Teile der Arbeit [(§ 18 Abs. 1 APSO-TI-BM bzw. § 21 Abs. 1 APSO-INGI)] – ohne fremde Hilfe selbständig verfasst und nur die angegebenen Quellen und Hilfsmittel benutzt wurden. Wörtlich oder dem Sinn nach aus anderen Werken entnommene Stellen sind unter Angabe der Quellen kenntlich zu machen."

*Quelle: § 16 Abs. 5 APSO-TI-BM bzw. § 15 Abs. 6 APSO-INGI*

Dieses Blatt, mit der folgenden Erklärung, ist nach Fertigstellung der Abschlussarbeit durch den Studierenden auszufüllen und jeweils mit Originalunterschrift als letztes Blatt in das Prüfungsexemplar der Abschlussarbeit einzubinden.
Eine unrichtig abgegebene Erklärung kann -auch nachträglich- zur Ungültigkeit des Studienabschlusses führen.

**Erklärung zur selbstständigen Bearbeitung der Arbeit**

Hiermit versichere ich,

Name: _____

Vorname: _____

dass ich die vorliegende – bzw. bei einer Gruppenarbeit die entsprechend gekennzeichneten Teile der Arbeit – mit dem Thema:

ohne fremde Hilfe selbständig verfasst und nur die angegebenen Quellen und Hilfsmittel benutzt habe. Wörtlich oder dem Sinn nach aus anderen Werken entnommene Stellen sind unter Angabe der Quellen kenntlich gemacht.

*- die folgende Aussage ist bei Gruppenarbeiten auszufüllen und entfällt bei Einzelarbeiten -*

Die Kennzeichnung der von mir erstellten und verantworteten Teile der ist erfolgt durch:

| _____ | _____ | _____ |
|---|---|---|
| Ort | Datum | Unterschrift im Original |